Bose-Einstein Condensation with High Atom Number in a Deep Magnetic Trap

Cover: Photos of the magnetic trap (by Henk Neerings) with an image of a Bose-Einstein condensate.

Bose-Einstein Condensation with High Atom Number in a Deep Magnetic Trap

ACADEMISCH PROEFSCHRIFT

ter verkrijging van de graad van doctor
aan de Universiteit van Amsterdam,
op gezag van de Rector Magnificus
prof. dr. J. J. M. Franse
ten overstaan van een door het college voor promoties ingestelde commissie,
in het openbaar te verdedigen in de Aula der Universiteit
op vrijdag 2 maart 2001, te 10 uur

door

Kai Dieckmann

geboren te Velbert, Duitsland

Promotor:	prof. dr. J. T. M. Walraven
Commissie:	prof. dr. D. Frenkel
	prof. dr. H. B. van Linden van den Heuvell
	prof. dr. G. Rempe
	prof. dr. G. V. Shlyapnikov
	dr. R. J. C. Spreeuw
	prof. dr. B. J. Verhaar
Faculteit:	Faculteit der Natuurwetenschappen, Wiskunde en Informatica

The work described in this thesis is part of the research program of the Stichting voor Fundamenteel Onderzoek der Materie (FOM), which is financially supported by the Nederlandse Organisatie voor Wetenschapplijk Onderzoek (NWO).
The author was supported by a Marie Curie Research Training Grant of the Training and Mobility for Researchers (TMR) activity under the Forth European Community Framework Program for research and technological development.

This work was started at

Van der Waals-Zeeman Instituut,
Universiteit van Amsterdam,
Valckenierstraat 65,
1018 XE Amsterdam,
The Netherlands,

and the main part was carried out at

FOM-Instituut voor Atoom- en Molecuulfysica (AMOLF),
Kruislaan 407,
1098 SJ Amsterdam,
The Netherlands.

ISBN 90-9014547-8

Contents

Chapter 1

Introduction

1.1 Research area

Bose-Einstein condensation was predicted in 1925 [Bose, 1924, Einstein, 1925], at the time when quantum mechanics was being developed. Seven decades later in 1995 Bose-Einstein condensation (BEC) in dilute atomic gases was first observed. Within a few months BEC was observed with the alkali atoms rubidium [Anderson et al., 1995] and sodium [Davis et al., 1995]. Lithium [Bradley et al., 1995, 1997] followed rapidly. This exciting achievement attracted a lot of attention in the scientific community and the mass media alike, in which Bose-Einstein condensation was referred to as a 'new state of matter'.

Dilute gases of neutral atoms can be studied at ultra-low temperature by confining them in a magnetic trap. Bose-Einstein condensation occurs when at high density and low temperature the thermal wavelength of the atoms becomes of the order of the interparticle separation between the atoms, and the atomic waves overlap. As the condensate forms, a macroscopic amount of atoms populate the ground state of the trap and share coherently the same wavefunction. The BEC transition temperature of dilute gases is typically slightly below $1\,\mu$K. Under normal conditions alkalis are in the solid state at room temperature and below. Therefore, the BEC in dilute gases is achieved in a metastable state, where the density of the gas is sufficiently low to prevent inelastic decay, and a long life time of the gas is achieved. For alkali gases at the highest attainable densities the dominant decay is three-body recombination by which diatomic molecules are formed and a third atom enables conservation of energy and momentum. Elastic collisions are essential for achieving a kinetic equilibrium after cooling of the gas and during the formation of the Bose-Einstein condensate. At microkelvin temperatures elastic collision happen in the s-wave scattering channel. At typical densities, the interparticle separation is big compared to the s-wave scattering length. In many experiments the mean interaction energy exceeds the kinetic energy of the Bose-condensed atoms. In this so called Thomas-Fermi case, the properties of the cloud are strongly influenced by the interactions between the atoms. For example, the shape of the Bose-condensed cloud

deviates strongly from the shape according to the ground state of the trapping potential.

Much of the early theory of interacting quantum gases was developed in the period $1940 - 1965$ and provided a microscopic basis for macroscopic quantum phenomena like suprafluidity of ^{4}He and superconductivity. However, the behaviour of the quantum fluid liquid helium is dominated by the strong interaction between the constituting particles. In order to focus the research on the Bose-Einstein phase transition itself, it was necessary to investigate dilute atomic gases.

The first attempts to achieve BEC in dilute gases were done with atomic hydrogen. Atomic hydrogen was supposed to be a good candidate for a nearly ideal Bose gas, as spin-polarized hydrogen does not form a many-body bound state, even at $T = 0$ [Etters et al., 1975]. The experimental techniques developed for trapping and cooling hydrogen strongly differ from the ones used in laser cooling and trapping of alkali atoms. The hydrogen atoms were first stabilized [Silvera and Walraven, 1980, Cline et al., 1980] in a cryogenic environment at subkelvin temperature. Magnetic trapping of hydrogen was realized by [Hess et al., 1987, van Roijen et al., 1988]. For the analysis of the gas samples spectroscopic methods as Lyman-α and two-photon spectroscopy have been developed requiring a demanding laser system. Evaporative cooling of the trapped gas, the crucial method that allowed to reach the phase transition, was first experimentally demonstrated [Hess, 1986] and developed [Luiten et al., 1996, Walraven, 1996] in the hydrogen work . BEC of atomic hydrogen led to the so far largest condensates and was achieved in 1998.

BEC was first achieved with alkali gases. This was a consequence of the development of laser based cooling and trapping methods for neutral atoms. Alkali atoms have been favored for this purpose, as for these species continuous wave lasers are available for the manipulation of the motion of the atoms. For example in case of rubidium easy to handle diode lasers can be used. A variety of methods for cooling and trapping, such as the magneto-optical trap, the optical dipole trap, sub-Doppler cooling, velocity selective coherent population trapping, and Raman-cooling have been developed [Phillips, 1998, Adams and Riis, 1997]. For the discovery and explanation of sub-Doppler laser cooling the Nobel prize was given in 1997 [Chu, 1998, Cohen-Tannoudji, 1998, Phillips, 1998]. So far, optical cooling methods did not lead directly to Bose-Einstein condensation, but are used in current experiments to produce precooled, trapped atomic samples in a non-cryogenic environment. As a final cooling process towards BEC evaporative cooling is used, during which typically 7 orders of magnitude in the phase-space density is gained.

The first achievements of BEC led to an enormous boost of activity and were followed to the present date by at least 24 successful BEC experiments world wide. The experimental progress is accompanied by extended theoretical work, which is leading to a deep understanding of the behaviour of Bose-condensed matter. A collection of articles and reviews can be found at [Edwards]. A theoretical review is given in [Dalfovo et al., 1999]. A number of experimental techniques, which are of importance for achieving BEC are summarized in [Ketterle et al., 1999, Cornell et al., 1999]. To the striking properties of Bose-condensed matter belongs the long range phase coherence which was experimentally demonstrated by [Andrews et al., 1997b, Stenger et al., 1999b]. Matter wave amplification due to Bosonic stimulation was demonstrated by [Inouye et al., 1999b,a]. In other experiments collisional properties were studied, such as the s-wave scattering length [Roberts et al., 1998, Boesten et al., 1997], the existance of two-species conden-

sates [Myatt et al., 1997], the three-body combination rate [Burt et al., 1997, Söding et al., 1999], and the existence and energy of Feshbach resonances [Tiesinga et al., 1992, Inouye et al., 1998, Roberts et al., 2000]. Important research related to condensed matter properties of the gas are the investigation of excitations of the condensate, such as the frequency spectrum and damping of elementary excitations [Jin et al., 1996, Mewes et al., 1996b, Jin et al., 1997], the propagation of sound waves [Andrews et al., 1997a] and solitons [Burger et al., 1999], and the creation of vortices [Matthews et al., 1999, Madison et al., 2000].

1.2 This thesis

This thesis deals with the quantum gas phase of atomic rubidium. The work involves the development of the experimental apparatus to reach the quantum degenerate regime and a first series of experiments with the rubidium quantum gas, including the attainment of Bose-Einstein condensation.

Emphasis is put on experiments with a large number of atoms. The availability of large numbers of cold atoms enables experiments with high density samples. From a practical point of view this allows fast thermalization and thus fast experimental procedures. From a theoretical point of view it allows the investigation of the cross-over from the collisionless into the hydrodynamic behaviour in the rubidium quantum gas.

This thesis is divided into the following chapters: In Chapter 2 some theoretical principles and results are briefly summarized to an extend as is needed for the description of the experiments. The atomic properties of rubidium, which are relevant for laser cooling and magnetic trapping are discussed. The principle of magnetic trapping is introduced, and the magnetic trapping configuration used in this thesis, which is of the Ioffe-Pritchard type [Pritchard, 1983], is explained. Bose-Einstein condensation of the trapped ideal gas is described followed by the main theoretical results for the case of repulsive interactions between the particles and large atom numbers. As of great importance for the achievement of Bose-Einstein condensation the principle evaporative cooling is briefly introduced.

Chapter 3 describes the main components of the experimental apparatus. First, it gives an overview over the laser system consisting of 5 diode lasers and the purpose of the produced laser beams for the experiment. In order to load a large atom number into a magneto-optical trap (MOT) an amount of laser power is required which exceeds the power of commonly used and commercially available diode lasers. In order to provide sufficient laser power a broad-area diode laser system, delivering 130 mW of usable laser power, was build and characterized for this experiment by [Shvarchuck et al., 2000]. For the work in this thesis the broad-area laser was integrated in the laser system and was for the first time applied in an experiment on laser cooling and trapping. Second, the vacuum system is described including a rubidium vapor cell for the realization of the atomic beam source and a UHV chamber where trapping and cooling of the gas cloud takes place. Next, a detailed portrait of the magnetic trap is given. In this work the design of the trap assembly was optimized to obtain high stability, flexibility in adjusting the trapping parameters, and a strong confinement of the gas. This enables fast and efficient evaporative cooling yielding high atom numbers and densities at the BEC phase

transition. Furthermore, the components for the rf-signal source used for evaporative cooling are specified. The chapter is ending with a description of the imaging system by which the properties of the cold gas clouds are measured.

Chapter 4 is based on the publication [Dieckmann et al., 1998] dealing with the intense atomic beam source developed in this experiment. The high atomic flux of the source is the basis of obtaining high atom numbers in a short time. The operation principle is based on the two-dimensional vapor cell magneto-optical (2D-MOT) trap. It is investigated how the atomic flux of a vapor cell based source can be optimized and an experimental comparison between different variations of the 2D-MOT geometry used as atomic beam sources has been performed. The highest achieved flux exceeds the atomic flux of existing vapor cell based atomic beam sources by almost two-orders of magnitude, for the same low laser (50 mW) power in use.

As described in Chapter 5 the atomic beam source is applied to load a magneto-optical trap with large atom number. This is done with the goal to take benefit of the high beam flux and to achieve a high atom number after a short loading time. The measured atomic beam flux is compared to the measurements of the trap loading. For the first time it was demonstrated that the effective loading flux can be improved by avoiding loss from the atomic beam due to a repulsive light force originating from fluorescence light from the magneto-optically trapped cloud. This is realized by optically pumping the atoms into a dark hyperfine state. After loading polarization gradient cooling is used to cool the cloud to a temperature below the Doppler limit, which is 144 μK for rubidium. Further, it is described how the temperature of the atomic cloud after sub-doppler cooling was minimized for the case of a large atom number.

Chapter 6 explains how the atoms are loaded from the magneto-optical trap into the magnetic trap. Further, the steps for adiabatic compression of the sample in the trap are individually characterized in detail. The characterization of magnetic trapping is completed by the measurement of the life time of the atomic sample and the measurement of the harmonic frequencies of the trap. Measurement of the life time of the sample in the compressed magnetic trap gives information on whether efficient evaporative cooling is possible and BEC can be achieved. Measurement of the harmonic trap frequencies is essential for subsequent quantitative analysis of the trapped Bose-gas.

In the first part of Chapter 7 evaporative cooling in the runaway regime is described. The efficiency of the evaporation process with respect to the particle loss is evaluated. Thereafter, the observation of Bose-Einstein condensation is presented including a description of the analysis methods used to obtain the cloud parameters from the absorption images. As highest atom numbers are achieved, gas samples can be produced which are in the transition region between the collisionless and the hydrodynamic regimes. As the last part of this chapter a demonstration of the so called 'atom laser' is added.

Chapter 8 deals with the so called Oort cloud. This is a cloud of rubidium atoms which populates the magnetic trap to energies of several mK. This is possible due to the large depth of the magnetic trap. It is demonstrated how for the first time clear evidence of an Oort cloud was obtained. A method for measuring the Oort cloud atom number is presented, and information on the energy distribution of the Oort cloud population is obtained. It is investigated, how the effects of the Oort cloud on the cold cloud can be suppressed by means of rf-shielding. With the origin of the Oort cloud identified, a

method for the reduction of the Oort cloud atom number is demonstrated. This enables to compare the effect of the Oort cloud on the cold cloud for large and reduced Oort cloud. Finally, the consequences of the observations on the non condensed samples for the possibilities of entering the hydrodynamic regime with a Bose-Einstein condensate are discussed.

Chapter 2

Theoretical basics

In this Chapter 2 theoretical principles and results are briefly summarized to an extend as is needed for the description of the experiments. The atomic properties of rubidium, which are relevant for laser cooling and magnetic trapping are discussed. The principle of magnetic trapping is introduced, and the Ioffe-quadrupole magnetic trapping configuration [Pritchard, 1983] is explained. In this thesis the magnetic trap is referred to as a 'Ioffe-quadrupole' trap. Bose-Einstein condensation of the trapped ideal gas is described followed by the main theoretical results for the case of repulsive interactions between the particles and large atom numbers. As of great importance for the achievement of Bose-Einstein condensation the principle evaporative cooling is briefly introduced.

2.1 Atomic properties of rubidium

Because of their advantageous atomic properties alkali atoms are used in many experiments on trapping and cooling of neutral atoms. In the following a brief description is given of atomic properties of rubidium, which are of relevance for the present work.

2.1.1 Hyperfine structure and laser cooling

The optical transitions from the ground state of rubidium are shown in Figure 2.1. Trapping and cooling is done with a 'trapping laser' operated at the hyperfine transition $5S_{1/2}, F = 2 \rightarrow 5P_{3/2}, F = 3$ of the D-2 line at a wavelength of $\lambda = 780\,\mathrm{nm}$. Light from this laser also gives rise to non-resonant excitation to the $5P_{3/2}, F = 2$ state, from which $^5/_8$ decay back to the $F = 2$ (upper) hyperfine level of the ground state, but $^3/_8$ decay to the $F = 1$ (lower) hyperfine level. Once the atoms are in this state, they can no longer be exited by the trapping light, as the 6.8 GHz energy splitting of the ground state is much bigger than the $\Gamma/(2\pi) = 6\,\mathrm{MHz}$ natural width of the trapping transition. Considering the hyperfine splitting of 267 MHz of the exited state the relative probability of ending up in the $F = 1$ ground state level, after excitation by the trapping laser is 5×10^{-5}, small but not negligible. By an additional so called 'repumping laser' the atoms can be

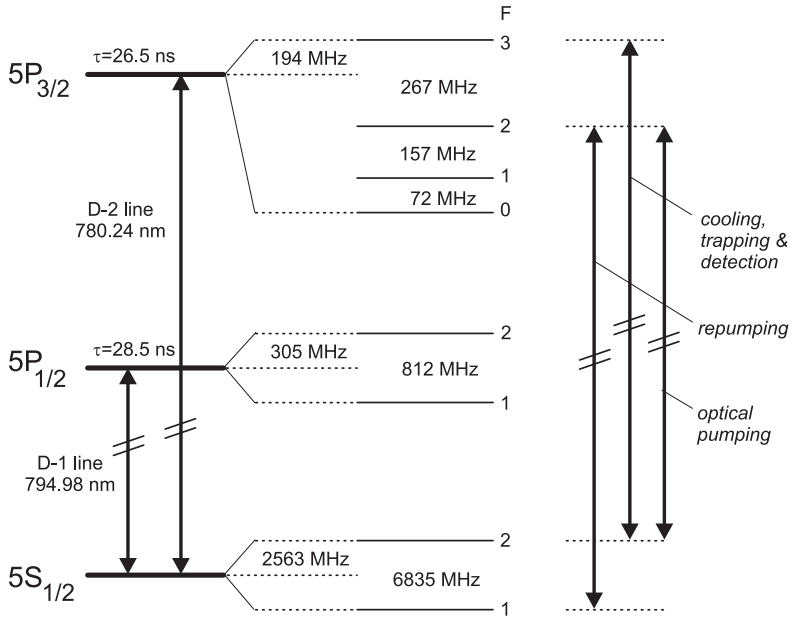

FIGURE 2.1: Hyperfine structure of ^{87}Rb: The D-2 line in the near infra-red regime is commonly used for laser cooling. The atoms can be magnetically trapped in both the $|F = 1\rangle$ and $|F = 2\rangle$ hyperfine states of the ground state $5S_{1/2}$. The data were taken from [Arimondo et al., 1977] and [Radzig and Smirnov, 1985].

resonantly exited to the state $5P_{3/2}, F = 2$, from where they can spontaneously decay back into the state $5S_{1/2}, F = 2$ again. If the trapping transition is driven resonantly with a saturation parameter $S_0 = 1$ it is sufficient to drive the repumping transition resonantly with a saturation parameter of $S_0 \approx 5 \times 10^{-5}$. The saturation intensity of the D-2 line is $1.65\,\mathrm{mW/cm^2}$. For optical pumping of the atoms to the $5S_{1/2}, F = 2, m_F = 2$ Zeeman state an 'optical pumping' laser resonant with the transition $5S_{1/2}, F = 2 \rightarrow 5P_{3/2}, F = 2$ is applied with σ^+-circular polarization.

2.1.2 Zeeman effect on the hyperfine ground states

Rubidium atoms can be magnetically trapped in either of the two hyperfine ground states. The Zeeman energy of these states in presence of a static magnetic field B can be expressed by the Breit-Rabi formula [Breit and Rabi, 1931, Ramsey, 1956], for the case of vanishing orbital angular momentum,

$$E_{F,\,m_F}(B) = (-1)^F \frac{1}{2}\hbar\,\omega_{\mathrm{hf}} \sqrt{1 + \frac{4m_F}{2I+1}\,x + x^2} + \mathrm{const.} \tag{2.1}$$

$$x = \frac{(g_I + g_s)\mu_{\mathrm{B}} B}{\hbar\,\omega_{\mathrm{hf}}} \quad . \tag{2.2}$$

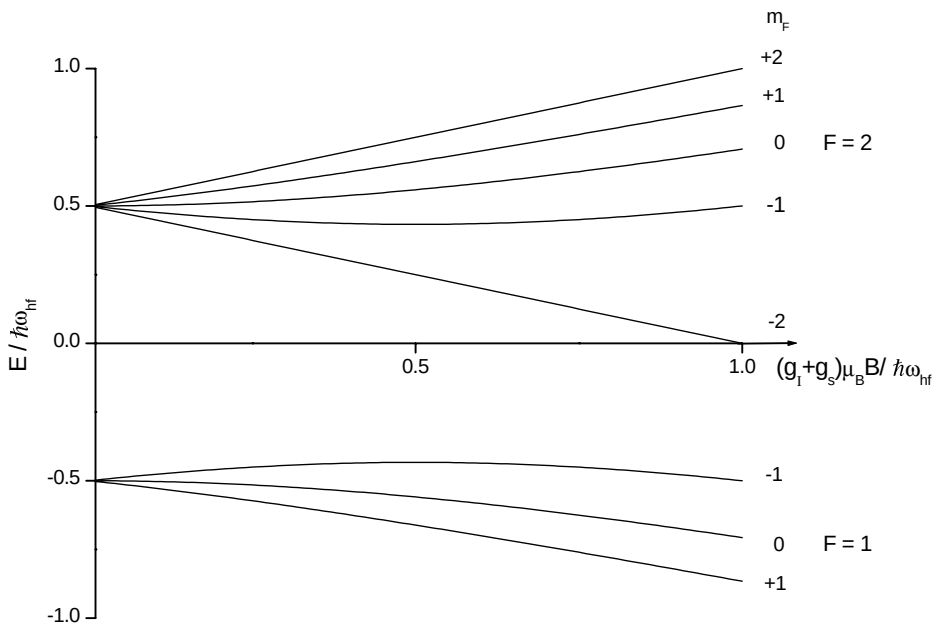

FIGURE 2.2: *Zeeman-effect of the hyperfine ground state: The energies of the magnetic sublevels and the parameter* $(g_I + g_s)\mu_B B$ *representing the magnetic field are normalized to the hyperfine splitting* $E_{\rm hf}$ *of the ground state. It is possible to magnetically trap the four 'low field seeking' states* $|F = 2, m_F = 2\rangle$, $|F = 2, m_F = 1\rangle$, $|F = 2, m_F = 0\rangle$, *and* $|F = 1, m_F = -1\rangle$, *of which the first one is used in this experiment.*

The values of the gyromagnetic factors g_I and g_s, the nuclear spin I, and the frequency of the hyperfine transition between the ground state levels $\omega_{\rm hf}$ are summarized in Table 2.1 and were taken from [Vanier and Audoin, 1988]. The contribution of the nuclear angular momentum can be neglected, as $g_I \ll g_s$. The resulting energies of the magnetic sublevels m_F are shown in Figure 2.2.

In typical magneto-static traps the Zeeman splitting $g_s \mu_B B$ is smaller than the hyperfine splitting $\hbar\omega_{\rm hf}$ of the ground state, and Equation (2.1) can be approximated by

$$E_{F,\,m_F}(B) = (-1)^F \left(\frac{1}{2}\,\hbar\,\omega_{\rm hf} + m_F\, g_F\, \mu_{\rm B}\, B + \frac{1}{16}(4 - m^2)\frac{(g_s\,\mu_{\rm B}\,B)^2}{\hbar\,\omega_{\rm hf}} \right) + \text{const.} \quad (2.3)$$

$$g_F = (-1)^F \frac{1}{2I+2} g_s \quad . \quad (2.4)$$

The first term in Equation (2.3) gives the 6.8 GHz hyperfine splitting of the rubidium ground state. The second term describes the linear Zeeman effect. The third term describes the quadratic dependency of the energy on the magnetic field strength, the so called 'quadratic Zeeman effect'. The states $|F = 2, m_F = \pm 2\rangle$ are pure spin states, for

g-factor nucleus	g_I	0.995×10^{-3}
g-factor electron	g_s	2.0023
nuclear spin	I	$\frac{3}{2}$
hyperfine energy	ω_{hf}	$2\pi \cdot 6.8346826128(5)\,\mathrm{GHz}$

TABLE 2.1: Some atomic properties of ^{87}Rb.

which the quadratic Zeeman effect is absent. For the trapped state $|F = 2, m_F = 1\rangle$ a significant shift of the Zeeman energy (10 % relative to the linear Zeeman effect) occurs for a magnetic field strength of 300 G.

2.2 Magnetic trapping and Ioffe-quadrupole configuration

The principle of magnetic trapping is based on the interaction of the magnetic moment $\boldsymbol{\mu}$ of the atom with an external magnetic field $\boldsymbol{B}(\boldsymbol{r})$. The interaction energy is given by

$$E = -\boldsymbol{\mu} \cdot \boldsymbol{B}(\boldsymbol{r}) \quad , \tag{2.5}$$

where $\boldsymbol{\mu} = m_F g_F \mu_{\mathrm{B}} \boldsymbol{F}/\hbar$ and $\boldsymbol{F}$ is the total angular momentum of the atom. The orientation of the magnetic moment relative to the direction of the magnetic field is quantized. Once the atom is polarized in a certain Zeeman-state m_F, it is driven towards either high ('high field seekers') or low ('low field seekers') magnetic fields depending on the sign of the gyromagnetic factor g_F, if $m_F \neq 0$. As has been proven by [Wing, 1983], in a spatial region of a inhomogeneous magnetic field free of electric currents only magnetic field minima but no maxima can exist. Thus, only atoms in low field seeking states can be trapped in a magnetic field minimum. In the low magnetic field limit the three trapped states of rubidium are $|F = 1, m_F = -1\rangle, |F = 2, m_F = 1\rangle$ and $|F = 2, m_F = 2\rangle$. Due to the quadratic Zeeman effect also the state $|F = 2, m_F = 0\rangle$ can be trapped in a low magnetic field. For this thesis the experiments were done with atoms in the $|F = 2, m_F = 2\rangle$ state. The simplest way to create a trapping magnetic field geometry is to use a pair of anti-Helmholtz coils producing a static spherical quadrupolar field. This geometry was used for the first demonstration of magnetic trapping of neutral atoms (sodium) [Migdall et al., 1985]. However, in spherical quadrupolar traps the life time of the thermal atomic sample is limited by atomic loss at the trap center where the magnetic field vanishes and the polarization of the gas is not conserved [Petrich et al., 1995]. At the magnetic field zero in the trap center the atoms undergo transitions to non-trapped Zeeman states. In order to circumvent this so called 'Majorana loss', different trapping geometries have been developed. One solution is the so called 'TOP-trap' [Petrich et al., 1995] employing a time varying magnetic field to create a finite magnetic field value in the center. This was used for the first observation of Bose-Einstein condensation in rubidium atoms [Anderson et al., 1995]. For this thesis a 'Ioffe-quadrupole' (IQ) magnetic trapping configuration is used. As shown in Figure 2.3, this is

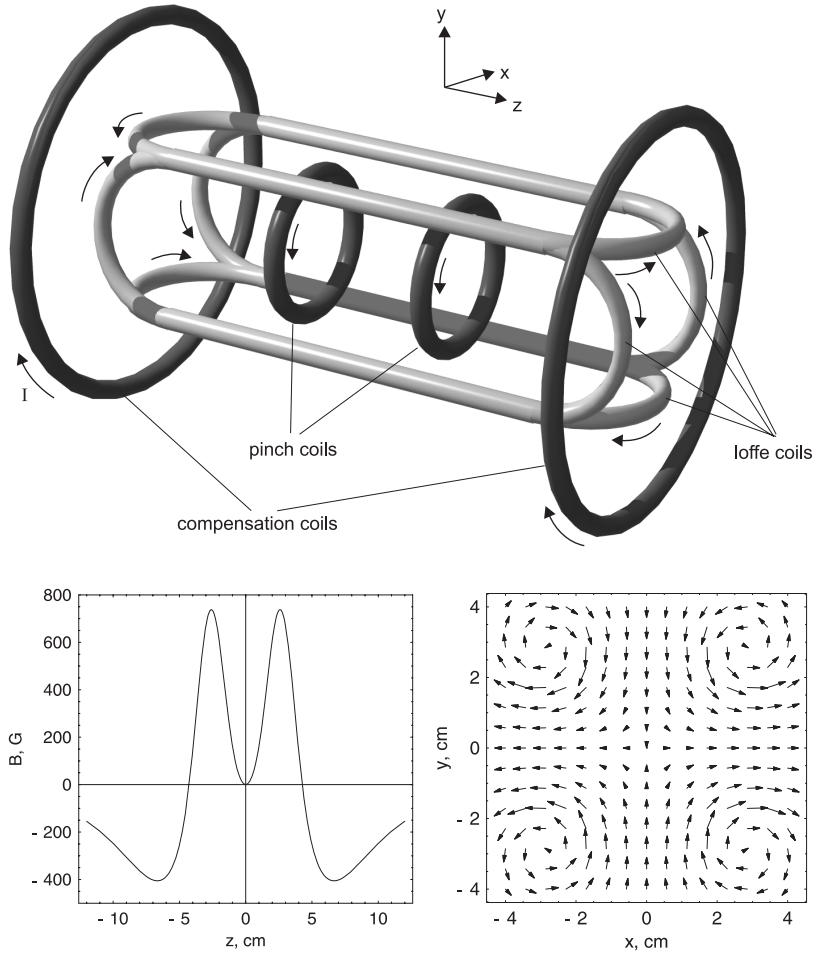

FIGURE 2.3: *The Ioffe-quadrupole magnetic trap geometry: The coils (top) produce a potential with axial symmetry. The direction of the currents I is indicated by the small arrows. Four 'race-track' shaped coils are combined to form four bars generating a linear quadrupole field (bottom right) for transverse confinement. The two pinch coils create a magnetic field minimum for confinement along the z-direction (bottom left). The large magnetic field of the pinch coils is reduced by the compensation coils to a small value of about* 1 *G, preventing Majorana loss.*

a magneto-static magnetic with non-zero minimum magnetic field for avoiding Majorana depolarization, as described by [Pritchard, 1983]. Often this trapping configuration is called 'Ioffe-Pritchard' configuration. The trapping potential has a cylindrical symmetry. For confinement along the radial direction a two-dimensional quadrupole magnetic field is used. The quadrupole field is produced by four 'race-track' shaped so called 'Ioffe coils'. The straight parts of these coils form four current bars, the so called 'Ioffe bars',

carrying currents in alternating directions and producing the radial quadrupole field. The absolute value of the quadrupole field increases linearly in radial direction with gradient α. The magnetic field produced by the curved sections of the Ioffe coils can be neglected, as these parts are positioned far from the trap center and cancel each other on the symmetry axis of the trap. The confinement along the direction of the symmetry axis is provided by the field in the z-direction produced by two pinch coils. As the currents in these coils have the same orientation and their separation exceeds the Helmholtz distance, a field minimum is created. The magnetic field along the symmetry axis is to a large extend quadratic with a curvature β. The large central magnetic field produced by the pinch coils is largely compensated by two so called compensation coils, placed at large distance from the trap center, to yield a small but finite offset value B_0. If B_0 is large enough, Majorana loss is prevented and a long life time of the trapped sample can be anticipated. In order to estimate the offset magnetic field needed to prevent transitions to untrapped Zeeman states, consider an atom moving with the thermal velocity v_T from outside towards the trap center along the radial direction. The atom is in a trapped Zeeman state with respect to the local direction of the magnetic field as a quantization axis, which is pointing in the radial plane. When passing through the center, the trapped Zeeman state is coupled to untrapped states by the offset magnetic field pointing in the axial direction. During crossing through the center, the direction of the atomic magnetic moment will adiabatically follow the local direction of the magnetic field, and the atom will remain in a trapped state, if the following condition for the Landau-Zener parameter Γ_{lz} [Zener, 1932, Rubbmark et al., 1981], is fulfilled:

$$\Gamma_{\mathrm{lz}} = \frac{(g_F \mu_{\mathrm{B}} B_0)^2}{\hbar\, m_F g_F \mu_{\mathrm{B}}\, \alpha\, v_T} \gg 1 \quad , \tag{2.6}$$

where $v_T = \sqrt{8 k_{\mathrm{B}} T/\pi\, m}$ is the thermal velocity of the gas. For the trapped gases described in this thesis, the temperature ranges up to 1 mK, in which case an offset magnetic field of $B_0 > 0.3\,\mathrm{G}$ should be sufficient to suppress Majorana loss to the 10^{-5} level in a single pass. The magnetic fields inside the coil assembly can be represented in cylindrical coordinates by [Luiten, 1993][†], [Bergeman et al., 1987]

$$\begin{aligned} B_\rho(\rho,\phi,z) &= -\alpha\rho\sin(2\phi) - \frac{1}{2}\,\beta\rho\,(z-z_0) \\ B_\phi(\rho,\phi,z) &= -\alpha\rho\cos(2\phi) \\ B_z(\rho,\phi,z) &= B_0 + \frac{1}{2}\beta\,(z-z_0)^2 - \frac{1}{4}\,\beta\rho^2 \quad . \end{aligned} \tag{2.7}$$

Therefore,

$$|\boldsymbol{B}| = \sqrt{\left(B_0 + \frac{\beta}{2}\,(z-z_0)^2\right)^2 + \left(\alpha^2 - \frac{\beta}{2}\,B_0 + \alpha\beta\,(z-z_0)\sin(2\phi)\right)\rho^2 + \frac{\beta^2\rho^4}{16}} \quad . \tag{2.8}$$

[†]Please note the difference in the definition of the magnetic field curvature β used here in contrast to the definition used in the cited publication.

Close to the center for $(B(\rho,\phi,z)-B_0)/B_0 \ll 1$ the magnetic field can be approximated by the harmonic field profile

$$B(\rho,z) = B_0 + \frac{1}{2}\left(\frac{\alpha^2}{B_0} - \frac{\beta}{2}\right)\rho^2 + \frac{1}{2}\beta\, z^2 \quad . \tag{2.9}$$

Along the radial direction, for $z = 0$ the harmonic approximation is valid over a radius of

$$\rho_{\mathrm{h}} = \frac{B_0}{\alpha}\left(1 - \frac{\beta\, B_0}{2\alpha}\right)^{-\frac{1}{2}} \tag{2.10}$$

from the trap center. Within this radius the corrections due to anharmonic orders are less than 25 %. From the harmonic potential expressed by Equation (2.5) with the magnetic field of Equation (2.9) the harmonic trap frequencies can be identified:

$$\omega_z = \sqrt{\frac{\mu_{\mathrm{B}}\, g_F\, m_F}{m}\,\beta} \quad , \tag{2.11}$$

$$\omega_\rho = \sqrt{\frac{\mu_{\mathrm{B}}\, g_F\, m_F}{m}\left(\frac{\alpha^2}{B_0} - \frac{\beta}{2}\right)} \quad . \tag{2.12}$$

For a strong radial confinement the radial frequency is dominated by the term α^2/B_0, and thus can be adjusted by changing B_0 with the help of the compensation coils. This adjustment is used for the final stage of adiabatic compression of the trapped cloud as will be described in Section 6.2. In order to evaluate the depth of the magnetic trap it is necessary to calculate the exact field at a distance from the trap center near the magnetic field coils (compare Section 3.3). Exact expressions of the magnetic fields generated by closed loops and straight bars of zero thickness can be found in [Bergeman et al., 1987]. For this thesis similar expressions have been derived for the magnetic field of a 'half-loop' representing the turns of the 'race-track' coils. With the help of these expressions the field was calculated allowing for the finite size of real wires by numerical integration over the cross section. It was found that in the region of interest the result was not significantly deviating from the magnetic field as calculated by Equation (2.8) for the same trapping parameters α, β, and B_0.

2.3 The ideal Bose-Gas

2.3.1 Bose-distribution function and Bose-Einstein condensation

In the following the theoretical results, which are necessary to describe trapped Bose-gases within this work, are briefly introduced. Expressions for the density distribution of the trapped gas and the transition temperature are obtained. A more detailed description can be found in [Bagnato et al., 1987, Walraven, 1996, Huang, 1963]. The trapped gas of bosons is described within the framework of the grand canonical ensemble. The atoms are trapped in an external potential $U(\boldsymbol{r})$ and occupy the single-particle motional states of the trap with the eigenenergies ϵ_k. The occupation number of these states is given by

the Bose-distribution

$$\langle n_k \rangle = \frac{1}{\mathrm{e}^{(\epsilon_k - \mu)/k_\mathrm{B}T} - 1} = \sum_{l=1}^{\infty} \exp(-l\,(\epsilon_k - \mu)/k_\mathrm{B}T) \quad . \tag{2.13}$$

For a given temperature the chemical potential is fixed by

$$N = \sum_k \langle n_k \rangle \quad . \tag{2.14}$$

At large temperature μ is large and negative. As the gas is cooled μ approaches the ground state energy ϵ_0 from negative values, until at the critical temperature T_C it becomes equal to ϵ_0. For given N the occupation number of the ground state N_0 becomes at T_C a macroscopic fraction of the total number of atoms, while μ and the number of atoms in the exited states become fixed. In the limit $T \to 0$ all atoms will end up in the ground state. This phenomenon is called Bose-Einstein condensation (BEC). In typical BEC experiments with ultra-cold gases in harmonic traps, the number of atoms is large and the energy associated to the temperature is big compared with the level spacing, $k_\mathrm{B}T \gg \hbar\omega$. The total number of atoms in exited states can be written as

$$N - N_0 = \int_0^\infty \mathrm{d}\epsilon\ \rho(\epsilon) \frac{1}{\mathrm{e}^{(\epsilon-\mu)/k_\mathrm{B}T} - 1} \quad , \tag{2.15}$$

where N_0 is the occupation of the ground state and $\rho(\epsilon)$ is the density of states of the gas trapped in the external potential $U(\boldsymbol{r})$, given by

$$\begin{aligned} \rho(\epsilon) &= \frac{1}{(2\pi\hbar)^3} \iint_{-\infty}^{+\infty} \mathrm{d}\boldsymbol{r}\mathrm{d}\boldsymbol{p}\ \delta\!\left(\epsilon - U(\boldsymbol{r}) - \frac{p^2}{2m}\right) \\ &= \frac{2\pi(2m)^{3/2}}{(2\pi\hbar)^3} \int_{U<\epsilon} \mathrm{d}\boldsymbol{r}\ \sqrt{\epsilon - U(\boldsymbol{r})} \quad . \end{aligned} \tag{2.16}$$

By changing from the sum of Equation (2.14) to the integration $\epsilon_0 = 0$ can be assumed. Above the phase transition the density distribution $n(\boldsymbol{r})$ of the cloud can be found with the normalization relation $N = \int \mathrm{d}\boldsymbol{r}\ n(\boldsymbol{r})$ and Equations (2.15) and(2.16) as

$$n\,(\boldsymbol{r}) = \frac{1}{\Lambda_T^3}\ g_{\frac{3}{2}}\!\left(\tilde{z}\,\mathrm{e}^{-U(\boldsymbol{r})/k_\mathrm{B}T}\right) \quad , \tag{2.17}$$

with the thermal de Broglie wavelength

$$\Lambda_T = \sqrt{\frac{2\pi\hbar^2}{m\,k_\mathrm{B}\,T}} \quad , \tag{2.18}$$

the fugacity $\tilde{z} = \mathrm{e}^{\mu/k_\mathrm{B}T}$ and the poly-logarithm function $g_\alpha(x) = \sum_{k=1}^{\infty} x^k/k^\alpha$. Independently of the trap geometry one finds, that BEC occurs, if in the center of the trap the so called degeneracy parameter $n(0)\Lambda_T^3$ is reaching the critical value ($\mu = 0$)

$$n(0)\Lambda_T^3 = g_{\frac{3}{2}}(1) = 2.612\ldots \quad . \tag{2.19}$$

Here $g_n(1) = \zeta(n)$, where $\zeta(n)$ is Rieman's ζ-function. Equation (2.19) reflects the feature that BEC occurs, if the thermal wavelength of the atoms in the gas is becoming on the order of the separation between the atoms. In case of an harmonic potential, e.g. in the center of a Ioffe-quadrupole trap, the density of states (2.16) is found to be

$$\rho_{\mathrm{ho}}(\epsilon) = \frac{1}{2}(\hbar\bar{\omega})^{-3}\epsilon^2 \quad , \tag{2.20}$$

with the with the mean trap frequency $\bar{\omega}$ defined as

$$\bar{\omega} = \left(\omega_\rho^2\,\omega_z\right)^{\frac{1}{3}} \quad . \tag{2.21}$$

The number of atoms in excited states follows by substituting Equation (2.20) into Equation (2.15) and evaluates to

$$N - N_0 = g_3(1)\left(\frac{k_{\mathrm{B}}T}{\hbar\bar{\omega}}\right)^3 \quad . \tag{2.22}$$

At the phase transition $N_0 = 0$ and one can solve for the critical temperature

$$T_{\mathrm{C}} = \frac{\hbar\bar{\omega}}{k_{\mathrm{B}}}\left(\frac{N}{g_3(1)}\right)^{\frac{1}{3}} \approx 0.94\,\frac{\hbar\bar{\omega}}{k_{\mathrm{B}}}N^{\frac{1}{3}} \quad . \tag{2.23}$$

2.3.2 The trapped gas in the classical regime

In the classical regime, where $|\mu| \gg k_{\mathrm{B}}T$ and $\mu < 0$, and thus $\tilde{z} \ll 1$, one finds with Equation (2.17) the density in the trap center

$$n(0) = \frac{1}{\Lambda_T^3}\,g_{\frac{3}{2}}(\tilde{z}) \approx \frac{1}{\Lambda_T^3}\,\tilde{z} \quad . \tag{2.24}$$

The thermal wavelength is in the classical regime much smaller than the separation between the atoms. From Equations (2.15), (2.16), and (2.24) it can be seen, that in the classical regime the number of atoms can be written as

$$N = n(0)\Lambda_T^3 Z_1 \quad , \tag{2.25}$$

with the classical canonical partition function for a single atom

$$Z_1 = \frac{1}{(2\pi\hbar)^3}\iint_{-\infty}^{+\infty}\mathrm{d}\boldsymbol{p}\,\mathrm{d}\boldsymbol{r}\;\mathrm{e}^{-(U(\boldsymbol{r})+p^2/2m)/k_{\mathrm{B}}T} \quad . \tag{2.26}$$

Defining the reference volume of the gas $V_e \equiv N/n(0)$ one finds

$$V_e = \Lambda_T^3 Z_1 \quad , \tag{2.27}$$

and the degeneracy parameter

$$n(0)\Lambda_T^3 = \frac{N}{Z_1} \quad . \tag{2.28}$$

In many cases the magnetic trapping potential belongs to the class of so called 'power-law' potentials, which can be written in the form $U(x,y,z) \propto |x|^{1/\delta_1} + |y|^{1/\delta_2} + |z|^{1/\delta_3}$ with $\delta = \sum_i \delta_i$ [Bagnato et al., 1987]. For example, $\delta = 3/2$ describes the harmonic trap and $\delta = 3$ the spherical-quadrupole geometry. In case of power-law potentials a simple form of the single-atom partition function can be found

$$Z_1^{\delta} = A_{\mathrm{PL}}^{\delta} \, (k_{\mathrm{B}}T)^{\delta+\frac{3}{2}} \, \Gamma\!\left(\frac{3}{2}+\delta\right) \quad , \tag{2.29}$$

where A_{PL}^{δ} is a constant, which depends on the strength of the potential. $\Gamma(x) \equiv \int_0^{\infty} \mathrm{d}t \; t^{x-1}\mathrm{e}^{-1}$ is the Euler gamma function. In case of the Ioffe-quadrupole trap with $B_0 = 0$, the single-atom partition function can be expressed by Equation (2.29) for $\delta = 5/2$. In the general case of the Ioffe-quadrupole trap the single-atom partition function can be expressed by the sum of two power-law contributions [Luiten et al., 1996, Pinkse et al., 1997, 1998]

$$\begin{aligned} Z_1^{\mathrm{IQ}} &= Z_1^{\delta=\frac{3}{2}} + Z_1^{\delta=\frac{5}{2}} \\ &= 6A_{\mathrm{IQ}} \, (k_{\mathrm{B}}T)^4 \left(1 + \frac{2U_0}{3k_{\mathrm{B}}T}\right) \quad , \end{aligned} \tag{2.30}$$

where $U_0 \equiv \mu_{\mathrm{B}} \, g_F \, m_F B_0$, and where the trap dependent constant A_{IQ} is related to the parameters α and β, of the Ioffe-quadrupole trap through

$$A_{\mathrm{IQ}} = \frac{(2\pi^2 m)^{\frac{3}{2}}}{(2\pi\hbar)^3 2 \, (\mu_{\mathrm{B}} \, g_F \, m_F \alpha)^2 \sqrt{\mu_{\mathrm{B}} \, g_F \, m_F \beta/2}} \quad . \tag{2.31}$$

In case of the harmonic trap in the classical regime it follows from Equations (2.17) and (2.28)-(2.31) that the density distribution has a Gaussian shape

$$n(\boldsymbol{r}) = \frac{N}{(\pi)^{3/2} \prod_i r_{0,i}} \, \mathrm{e}^{-\sum_i \left(\frac{r_i}{r_{0,i}}\right)^2} \quad , \tag{2.32}$$

with a 1/e-radius of the cloud in the i-direction

$$r_{0,i} = \frac{1}{\omega_i}\sqrt{\frac{2k_{\mathrm{B}}T}{m}} \quad , \tag{2.33}$$

depending on the harmonic frequencies ω_i.

2.3.3 Adiabatic compression

Thermodynamic properties of the gas can be evaluated from statistical properties with the relation between the canonical partition function Z and the free energy $F = E - TS$

$$Z = \frac{Z_1^N}{N!} \equiv \mathrm{e}^{-F/k_{\mathrm{B}}T} \quad . \tag{2.34}$$

The internal energy E can be expressed as

$$E = Nk_{\mathrm{B}}T\left(\frac{3}{2}+\gamma\right) \quad , \tag{2.35}$$

where

$$\gamma \equiv \left(\frac{T}{V_e}\right)\frac{\partial V_e}{\partial T} \quad . \tag{2.36}$$

The first term in Equation (2.35) represents the kinetic energy, whereas the second term, which is proportional to γ, represents the contribution of the potential energy. Starting from Equation (2.34) and using Equations (2.28), (2.35), and Stirling's formula $\ln(N!) \approx N\ln(N) - N$ one finds that the degeneracy parameter can be written as [Pinkse et al., 1997]

$$n(0)\Lambda_T^3 = \mathrm{e}^{\frac{5}{2}+\gamma-\frac{S}{Nk_{\mathrm{B}}}} \quad . \tag{2.37}$$

For power-law traps in the classical regime the relation $\gamma = \delta$ holds. In case of the Ioffe-quadrupole trap γ can be found by evaluating the Equations (2.26), (2.27), and (2.30)

$$\gamma_{\mathrm{IQ}} = \frac{\frac{3}{2}+\frac{3k_{\mathrm{B}}T}{2U_0}\frac{5}{2}}{1+\frac{3k_{\mathrm{B}}T}{2U_0}} \quad . \tag{2.38}$$

During an adiabatic change of the of the trapping potential, where the entropy S and the atom number N are conserved, temperature and density are changing. The degeneracy parameter stays constant unless γ is varied by changing the 'shape' of the potential. The reversible change of the degeneracy parameter by changing the shape, i.e. the δ parameter, of the power law potential, and thus γ, was first experimentally demonstrated for magnetically trapped hydrogen by [Pinkse et al., 1997]. Adiabatic compression of the gas in the Ioffe-quadrupole trap, as discussed in Chapter 6.2, will result in a change of the temperature as well as the degeneracy parameter of the gas. From Equation (2.37) it follows that for the compression from some initial (index i) to final (index f) trapping parameters

$$\frac{n_f(0)\Lambda_{T,\,f}^3}{n_i(0)\Lambda_{T,\,i}^3} = \frac{\mathrm{e}^{\gamma_f^{\mathrm{IQ}}}}{\mathrm{e}^{\gamma_i^{\mathrm{IQ}}}} \quad . \tag{2.39}$$

The final temperature and density has to be determined by solving (2.39) numerically. In the special case of adiabatic compression in a harmonic trap the simple relation

$$T_f = T_i\frac{\bar{\omega}_f}{\bar{\omega}_i} \tag{2.40}$$

can be obtained. Equations (2.39) and (2.40) are valid, if the change of the trapping potential is done adiabatically. During the compression of a harmonic trap the density of states remains unchanged. The adiabaticity is then given, if the condition

$$\frac{\mathrm{d}\omega}{\mathrm{d}t} \ll \omega^2 \tag{2.41}$$

is fulfilled. A more detailed discussion of the adiabaticity criterium in this case is given in [Ketterle et al., 1999].

2.4 The weakly interacting Bose-gas

In the physics of ultra-cold, dilute alkali gases the elastic interaction between the atoms play an important role. For example, the density profile $n_c(\boldsymbol{r})$ of the Bose-Einstein condensate is deviating from the Gaussian shape of the ground state of the harmonic potential because of elastic interaction. At low energies elastic collisions happen in the s-wave scattering limit. Scattering can be described by the use of the pseudo potential [Huang, 1963]

$$V(\boldsymbol{r}-\boldsymbol{r}^{'}) = g\,\delta(\boldsymbol{r}-\boldsymbol{r}^{'}) \quad , \tag{2.42}$$

with the interaction parameter

$$g = \frac{4\pi\hbar^2 a}{m} \quad . \tag{2.43}$$

In the case of rubidium the interaction is repulsive and the positive value of the triplet scattering length is $a = (106\pm4)\times a_0 = 57.7\times10^{-10}\,\mathrm{m}$ [Roberts et al., 1998, Boesten et al., 1997] with Bohr's radius $a_0 = 0.529\times10^{-10}\,\mathrm{m}$. The use of the s-wave approximation is justified as long as the condition $|R_0/\Lambda_T| \ll 1$ is fulfilled, where $R_0 \equiv (C_6\,m/(2\hbar^2))^{1/4}$ is the range of the potential. As in case of ^{87}Rb the van der Waals coefficient is $C_6 = 4700\pm50\,\mathrm{a.u.} = 4.3\times10^{-76}\,\mathrm{J\,m^6}$ [Roberts et al., 1998] and hence $R_0 = 73\times10^{-10}\,\mathrm{m}$ the s-wave scattering approximation is justified for temperatures much smaller than 1 mK. It is noted here that for temperatures around 400μK the elastic collisional cross section of ^{87}Rb is enhanced due to the presence of a d-wave resonance [Burke et al., 1998]. At typical densities of $n = 10^{15}\,\mathrm{cm^{-3}}$ the so called gas parameter is small $n\,a^3 \ll 1$, and only binary elastic collisions have to be considered. If the correlations between the atoms manifest themselves only over a short range, i.e. at a range much smaller than the size of the gas cloud, the gas can be described in terms of a mean field theory [Bogoliubov, 1947]. For $T < T_C$ the macroscopic wave function $\phi(\boldsymbol{r})$ of the condensed part of the trapped gas obeys in the equilibrium case the so called time-independent Gross-Pitaevskii (GP) Equation [Goldman and Silvera, 1981, Huse and Siggia, 1982]

$$\left(-\frac{\hbar^2\nabla^2}{2m} + U(\boldsymbol{r}) + g\,|\phi(\boldsymbol{r})|^2\right)\phi(\boldsymbol{r}) = \mu\,\phi(\boldsymbol{r}) \quad . \tag{2.44}$$

At high densities $n_c(\boldsymbol{r}) = |\phi(\boldsymbol{r})|^2$ and if repulsive interaction ($a > 0$) is considered, the mean field interaction $g\,n_c(\boldsymbol{r})$ becomes dominant over the kinetic energy, which is on the order of $\hbar\,\omega_\rho$. In the case that

$$g n_c(\boldsymbol{r}) \gg \hbar\omega_\rho \tag{2.45}$$

the kinetic term in the GP Equation (2.44) can be neglected. This is known as the Thomas-Fermi approximation. In this case the GP equation can easily be solved, and the density distribution of the condensate is a result of the balance between the external potential and the repulsive mean field interaction:

$$n_c\,(\boldsymbol{r}) = \frac{1}{g}\,(\mu - U(\boldsymbol{r})) \quad . \tag{2.46}$$

In the case of a harmonic potential with trap frequencies ω_i, the density profile of the cloud has a parabolic shape. The density vanishes where the potential energy surpasses

the chemical potential. Thus, the 'Thomas-Fermi' radius R_i of the cloud in the i-direction is given by

$$R_i = \frac{1}{\omega_i}\sqrt{\frac{2\mu}{m}} \quad . \tag{2.47}$$

By integrating over the density distribution the number of condensed atoms is calculated to be

$$N_0 = \int \mathrm{d}\boldsymbol{r}\, n_\mathrm{c}(\boldsymbol{r}) = \left(\frac{2\mu}{\hbar\,\bar{\omega}}\right)^{\frac{5}{2}} \frac{a_\mathrm{ho}}{15\,a} \quad , \tag{2.48}$$

where $a_\mathrm{ho} = \sqrt{\hbar/m\bar{\omega}}$ is the harmonic oscillator length.

2.5 Evaporative cooling

Evaporative cooling is a powerful cooling method that does not suffer from the limitations encountered with optical cooling methods, such as the Doppler-limit and the recoil-limit. For all experiments in which BEC was achieved evaporative cooling was used as the final cooling stage. Evaporative cooling was first realized in an experiment with trapped atomic hydrogen [Hess et al., 1987]. A review on evaporative cooling is given by [Walraven, 1996, Ketterle and van Druten, 1996].

2.5.1 Evaporative cooling model

In the following the principle of evaporative cooling is briefly sketched. The description is based on the model of evaporative cooling introduced by [Luiten et al., 1996, Walraven, 1996]. Evaporative cooling is based on the preferential removal of atoms above a certain truncation energy ϵ_t from the trap and subsequent thermalization by elastic collisions. For constant truncation barrier ϵ_t (plain evaporation) elastic collisions between atoms in a trap produce atoms of energies higher than ϵ_t, which are 'evaporated' from the trap. The evaporation rate per atom can be expressed as

$$\tau_\mathrm{ev}^{-1} = \frac{\dot{N}_\mathrm{ev}}{N} = n(0)\, v_T\, \sigma\, \mathrm{e}^{-\eta} \frac{V_\mathrm{ev}}{V_\mathrm{e}} \quad , \tag{2.49}$$

where $\sigma = 8\pi a^2 = 7.9 \times 10^{-16}\,\mathrm{m}^2$ is the elastic collisional cross section, and

$$\eta = \frac{\epsilon_\mathrm{t}}{k_\mathrm{B} T} \tag{2.50}$$

is the truncation parameter. Here $V_\mathrm{ev} \approx V_\mathrm{e}$ is the effective volume for evaporation [Walraven, 1996]. As atoms are evaporated from the trap, the mean energy per atom is decreased and hence the gas cools. As the temperature decreases, η becomes larger and the evaporation rate is exponentially suppressed. A continuous cooling process can be realized by reducing ϵ_t (forced evaporative cooling) for instance in a way that η remains constant. It can be shown that for forced evaporative cooling at constant η

$$T \propto N^{\alpha_\mathrm{ev}} \quad , \tag{2.51}$$

when the efficiency parameter

$$\alpha_{\mathrm{ev}} \equiv \frac{\mathrm{d}\ln(T)}{\mathrm{d}\ln(N)} \tag{2.52}$$

only depends on the value of the truncation parameter η. During cooling also the effective volume is decreasing. For power-law traps this can be expressed by

$$V_{\mathrm{e}} \sim T^{\delta} \quad , \tag{2.53}$$

where $\delta = 5/3$ describes the Ioffe-quadrupole trap at high temperature (linear limit) and $\delta = 3/2$ describes the Ioffe-quadrupole trap at low temperature (harmonic limit). Importantly, in spite of the massive loss of atoms due to the evaporation process, the density $n(0)$ in the trap center can remain constant or even increase provided $\alpha_{\mathrm{ev}} \geq 1/\delta$, as can be seen by combining Equations (2.51) and (2.53) as well as the definition $V_{\mathrm{e}} \equiv N/n(0)$. In order to realize such a density increase, large η and thus slow evaporation is necessary. If the increase of the density is so strong that the elastic collisional rate $\tau_{\mathrm{el}}^{-1} \sim n(0)\, v_T \sim n(0)\, T^{1/2}$ increases, although the temperature decreases, the so called 'runaway' evaporative cooling regime is reached: The evaporation process proceeds faster and faster for decreasing temperature. The runaway condition can be expressed as

$$\frac{\mathrm{d}\ln\left(n\sqrt{T}\right)}{\mathrm{d}\ln(N)} = 1 - 2\,\alpha_{\mathrm{ev}} < 0 \tag{2.54}$$

In practice, the efficiency of evaporative cooling is limited by atomic loss from the trap, which in case of rubidium is caused by collisions with particles from the vacuum background (see Section 6.3) and at high densities is caused by three-body recombination. In general the atomic loss rate τ_i^{-1} for an i-body loss process can be expressed by the rate constants G_i

$$\tau_i^{-1} \equiv \frac{\dot{N}_i}{N} = -G_i\, n(0)^{i-1} \frac{V_{i\mathrm{e}}}{V_{\mathrm{e}}} \quad , \tag{2.55}$$

where the reference volumes for i-body collisions are defined as

$$V_{i\mathrm{e}} \equiv \int \mathrm{d}\boldsymbol{r} \left(\frac{n(\boldsymbol{r})}{n(0)}\right)^{i} \quad . \tag{2.56}$$

For two- and three-body loss processes ($i = 2, 3$) the reference volume can be calculated numerically, whereas for background collisions this volume is the reference volume as introduced in Equation (2.27). Evaporative cooling is most efficient for a large ratio R_i of the evaporation rate to the dominant loss rate, the so called 'ratio of good to bad collisions', which is given by

$$R_i \equiv \frac{\dot{N}_{\mathrm{ev}}}{\dot{N}_i} = \frac{n(0)\, v_T\, \sigma \frac{V_{\mathrm{ev}}}{V_{\mathrm{e}}}\, \mathrm{e}^{-\eta}}{n^{-1}(0)\, G_i \frac{V_{i\mathrm{e}}}{V_{\mathrm{e}}}} \equiv \frac{1}{\lambda_i} \frac{V_{\mathrm{ev}}}{V_{\mathrm{e}}}\, \mathrm{e}^{-\eta} \quad . \tag{2.57}$$

Here,

$$\lambda_1 \equiv \frac{\tau_i^{-1}}{\tau_{\mathrm{el}}^{-1}} = \frac{n^{i-2}(0)\, G_i}{v_T\, \sigma} \frac{V_{i\mathrm{e}}}{V_{\mathrm{e}}} \quad , \tag{2.58}$$

where the elastic collisional rate $\tau_{\rm el}^{-1}$ is defined as

$$\tau_{\rm el}^{-i} \equiv n(0)\, v_T\, \sigma \quad . \tag{2.59}$$

In typical BEC experiments with alkali gases at the beginning of evaporative cooling only background collisional loss has to be considered. In case of the Ioffe-quadrupole trap a numerical calculation of the efficiency parameter $\alpha_{\rm ev}$ as a function of η and λ_i is presented in [Valkering, 1999]. From the calculation follows that for an optimal choice of η and for

$$\lambda_i \lesssim 10^{-2} \tag{2.60}$$

forced evaporative cooling in the runaway regime, i.e. $\alpha_{\rm ev} > 1/2$, can be achieved (see Section 7.1. Once the threshold condition for runaway evaporative cooling is fulfilled, it is desirable to perform the cooling in such a way, that at the BEC transition the maximum number of atoms remains. This can be achieved by choosing an optimized time dependence of $\eta(t)$ in order to maximize $\alpha_{\rm ev}$. A simulation of forced evaporative cooling with the goal to find the optimized trajectory $\eta(t)$ for the conditions of this experiment was performed by [Valkering, 1999]. The calculation was based on the kinetic model of [Luiten et al., 1996, Walraven, 1996]. As a result it was found that evaporative cooling to the BEC transition within a few seconds is possible for typical initial conditions as used for the present experiment (compare Section 7.1). The optimal time dependence of the truncation energy $\epsilon_{\rm t}(t)$ is almost linear. As the analysis shows, only close to the BEC transition it is advantageous to evaporate faster, because the density has increased to a value where 3-body losses are important.

2.5.2 Rf-evaporative cooling

The energy selective removal of the atoms from the trap is done by driving transitions to untrapped Zeeman states by applying an oscillating magnetic field of angular frequency $\omega_{\rm rf}$. The covered frequency range lies typically in the radio frequency regime from 500 kHz to 50 MHz. The atoms undergo the transitions only at positions where the resonance condition

$$\mu_{\rm B}\, g_F |B(\boldsymbol{r})| = \hbar\, \omega_{\rm rf} \tag{2.61}$$

is fulfilled. Therefore, the truncation energy ϵ_t at which atoms in the state m_F are removed from the trap is related by Equation (2.5) to the rf-frequency $\omega_{\rm rf}$ as

$$\epsilon_{\rm t} = m_F \hbar\, (\omega_{\rm rf} - \omega_0) \quad , \tag{2.62}$$

where $\omega_0 = \mu_{\rm B}\, g_F |B(0)|/\hbar$ is the resonance frequency at the center of the trap. Due to their thermal motion the atoms are passing with different velocities through the trap. This can equivalently be seen as an atom at rest experiencing a time varying magnetic field. In which state the atoms leave the resonance region depends on the rate of change of the magnetic field, e.g. the velocity of the atoms, and on the strength of the oscillating rf-magnetic field. In case of low velocity and high rf-magnetic field amplitude the atom adiabatically undergoes the transition to the untrapped state. In the opposite case the atom remains in a trapped state after a non-adiabatic passage through the region of resonance. For a two-level atom the transition probability has been calculated in a

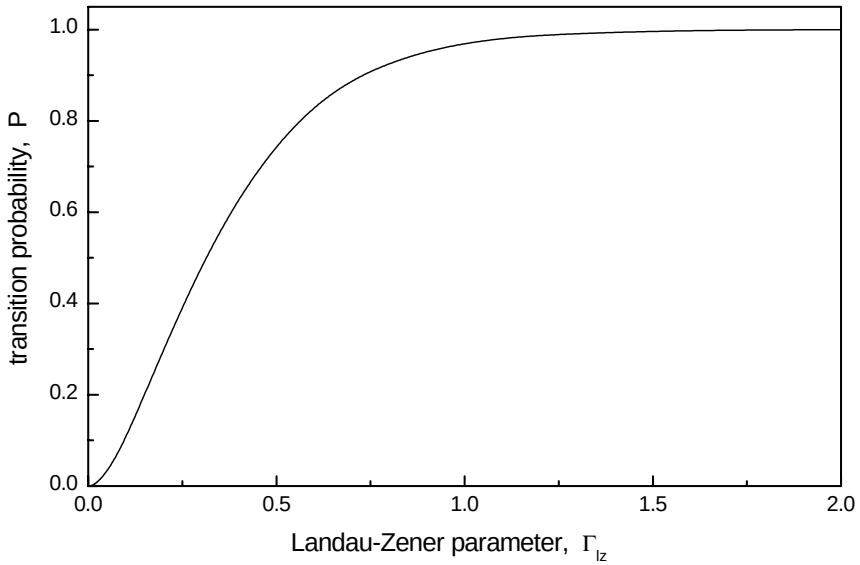

FIGURE 2.4: *For the adiabaticity parameter* $\Gamma_{\rm lz} \equiv 1$ *the transition probability to an untrapped state of the five level atom is about* 97%.

Landau-Zener picture by [Zener, 1932, Rubbmark et al., 1981]. In case of the $F = 2$ state of rubidium the 5 Zeeman levels $|F = 2, m_F = -2, \ldots, +2\rangle$ have to be considered. Atoms are originally trapped in the state $|F = 2, m_F = +2\rangle$. Assuming a linearly polarized oscillatory field with amplitude $B_{\rm rf}$ along the x-axis perpendicular to the trapping field $B(t)$, the magnetic field can be expressed as

$$\boldsymbol{B}(t) = B(t)\,\hat{\boldsymbol{e}}_z + B_{\rm rf}\,\cos(\omega_{\rm rf} t)\,\hat{\boldsymbol{e}}_x \quad . \tag{2.63}$$

The time dependent Hamiltonian (2.5) becomes then

$$\mathbb{H}(t) = \frac{\mu_{\rm B}\, g_F}{\hbar}\, B(t)\,\mathbb{F}_z + 2\omega_R \cos(\omega_{\rm rf} t)\,\mathbb{F}_x \quad , \tag{2.64}$$

with the Rabi frequency $\omega_{\rm R} = \mu_{\rm B}\, g_F B_{\rm rf}/(2\hbar)$. The set of time dependent Schrödinger equations for this Hamiltonian has been solved numerically for an atom passing through the resonance region being initially in the $m_F = +2$ state. After the passage the atom is in a superposition of all Zeeman states with the amplitudes $c_i, i \in \{-2, \ldots, +2\}$. From the result of the numerical calculation [Valkering, 1999] the probability of the atom being in an untrapped state $P = |c_{-2}|^2 + |c_{-1}|^2 + |c_0|^2$ can be calculated. The probability is dependent on the Landau-Zener parameter

$$\Gamma_{\rm lz} = \frac{\hbar\,\omega_R^2}{\mu_{\rm B}\, g_F\, 2 v_T\, ({\rm d}B/{\rm d}r)} \quad . \tag{2.65}$$

As shown in Figure 2.4 for $\Gamma_{\rm lz} \equiv 1$ the atom is removed from the trap with a probability of about 97%. For a given temperature and rf-magnetic potential a minimum magnetic field

amplitude has to be applied in order to ensure an adiabatic passage. If one assumes, that the atom which is to be removed from the trap moves with twice the thermal velocity v_T, it follows from (2.65) that for constant transition probability B_{rf} decreases as $\sqrt[4]{T}$. It is noted here, that [Vitanov and Suominen, 1997] the Landau-Zener transition probability of a multi-level system is related to that of a two-level system by recursion relations. At high truncation energies, e.g. for large magnetic fields, the quadratic Zeeman effect leads to incomplete evaporation [Desruelle et al., 1999] as will be further discussed in Section 8.5. A strong rf-magnetic field leads to an effective reduction of the oscillation frequencies of the atoms in the trap. An upper boundary on the rf-magnetic field amplitude, which may be applied, is imposed by the energy shift of the magnetic sublevels caused by the oscillatory magnetic field. By diagonalizing the Hamiltonian (2.64) the energy eigenstates ('dressed' states) of the trapped atom in presence of the rf-field can be found. Writing the energy of the trapped state up to second order in the static magnetic field for a given ω_{rf} and ω_{R}, yields the effective trap frequency of the trap. In case of the Ioffe-quadrupole trap the effective trap frequencies ω_i^{eff} are given by

$$\omega_i^{\mathrm{eff}} = \omega_i \left(\left(\frac{\omega_R}{\omega_0 - \omega_{\mathrm{rf}}} \right)^2 + 1 \right)^{-1/4} \quad . \tag{2.66}$$

In case of low detuning from the trap center and large Rabi- frequency the effective trap frequency can be strongly reduced, even to the point that the confinement is lost.

Chapter 3

Experimental apparatus and methods

For the realization of Bose-Einstein condensation of alkali atoms a big variety of experimental techniques have to be implemented. First of all, laser cooling and trapping methods are used to create a precooled atomic cloud. Therefore, a number of laser beams are needed, which are frequency stabilized close to the optical transitions of the atoms. In case of rubidium this requires laser light in the near-infrared regime at a wavelength of 780 nm (see Section 2.1.1) that can be generated by diode lasers. As diode lasers are comparably reliable devices, a number of them can be combined in an integrated table-top laser system, which is described in Section 3.1.

The ultra-cold gas is contained in an ultra-high vacuum (UHV) chamber as described in Section 3.2. As excitation of the gas by the thermal background is negligible, no additional precautions for thermal shielding are required. This important feature can be fully exploited in experiments with alkali atoms. This is in contrast to experiments on magnetic trapping of atomic hydrogen, where a cryogenic environment is required to load the trap [Hess et al., 1987, van Roijen et al., 1988].

By designing the UHV chamber to be compact the whole vacuum assembly fits on top of a standard size optical table. Interestingly, the vacuum system can be made very compact, as only light fields and magnetic fields are required to manipulate and investigate the samples and these fields can be applied with components outside the vacuum. This approach to minimize the number of components inside the vacuum also avoids problems related to vacuum compatibility at the 10^{-11} mbar level.

The magnetic trap coils described in Section 3.3 are build around the vacuum cell. As a strong confinement and at the same time fast switching has to be achieved, water cooled magnetic field coils of a low winding number carrying currents of up to 400 A are necessary.

Evaporative cooling to the BEC phase-transition makes a broad-band source of radio-frequency radiation (see Section 3.4) unavoidable to the electronic environment of the setup.

The typical size of a Bose-Einstein condensate is 5-100 μm. Thus optical absorption imaging of the condensate involves the use of a calibrated microscope as described in Section 3.5.

Reproducible experiments with a Bose-Einstein condensate require control over a sequence of 250 operations separated by precise time intervals varying from 1 μs to several seconds. For this purpose a real-time automation hard- and software system was developed. It manages the control and allows the immediate data analysis of the experiments in parallel with the measurements. This system, for which the newest hard- and software technologies have been employed is not further described in this thesis. The software has been made available to other research groups.

In order to combine all these techniques a strong emphasis has been put on compactness, reliability and flexibility during the building stage. In this way it was possible to create a setup, which provides the experimental flexibility and reliability to investigate Bose-condensed matter.

3.1 The laser system

The diode laser system is shown in form of a block diagram in Figure 3.1. The system occupies one half of an optical 1.5 m×2.4 m table. The laser beams are guided directly or via optical fibers towards the optical setup around the vacuum system located on the other half of the table.

Starting point is a grating stabilized diode laser [Wieman and Hollberg, 1991, Ricci et al., 1995] (TUI Optics, DL100), housing a single spatial and spectral mode laser diode (Hitachi, HL7851G, 50 mW). The grating stabilized output power is 25 mW. A power of 1.9 mW is used for frequency stabilization employing Doppler-free absorption spectroscopy. The frequency of the light is stabilized to the 'cross-over' signal between the two hyperfine transitions of the ^{87}Rb D-2 line: $|5S_{1/2}, F = 2\rangle \rightarrow |5P_{3/2}, F = 3\rangle$ and $|5S_{1/2}, F = 2\rangle \rightarrow |5P_{3/2}, F = 1\rangle$. By using a sideband-free, polarization-sensitive spectroscopy method [Suter, 1997], the frequency was stabilized to a bandwidth of 700 kHz. The diode laser and stabilization method are described in an undergraduate thesis [Garrec, 1996].

The primary (23 mW) laser beam is split into four beams, each of which is frequency shifted by an acousto-optical modulator (AOM) in double-pass configuration. This provides independent and precise frequency control over the four beams, in which the AOMs are driven by voltage controlled oscillators (VCO) connected to the computer control.

The first beam (1.8 mW) is frequency shifted close to the transition $|5S_{1/2}, F = 2\rangle \rightarrow |5P_{3/2}, F = 3\rangle$ with an adjustable detuning ranging from -55 to $+70$ MHz. This transition is used to drive the atomic beam source described in Chapter 4. This beam is used for injected locking of a single mode laser diode (Hitachi, model as above) [Bouyer, 1993]. After spatial filtering with a pinhole, this diode provides 34 mW of injection locked power.

The second beam (5.8 mW) is shifted into resonance with the transition $|5S_{1/2}, F = 2\rangle \rightarrow |5P_{3/2}, F = 3\rangle$. It serves as a probe beam for the analysis of the atomic beam source. From this beam a part is split off serving as a beam block ('plug beam') for the atomic beam (see Chapter 4).

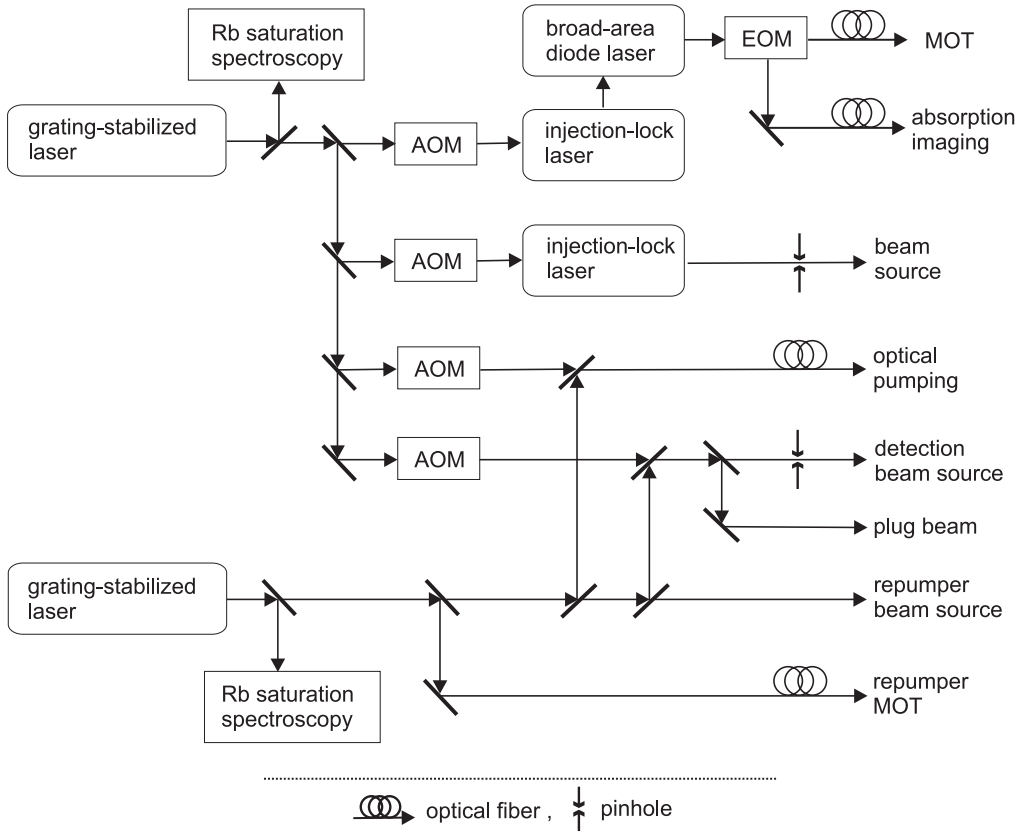

FIGURE 3.1: *Block diagram of the diode laser system. The frequencies of two grating stabilized diode lasers are attached to the ^{87}Rb D-2 line by Doppler-free spectroscopy. The beams are frequency shifted by acousto-optical modulators (AOM) and amplified by injection locking of three other diode lasers including a broad area diode laser (BAL).*

The third beam (8.4 mW) is shifted into resonance with the transition $|5S_{1/2}, F = 2\rangle \rightarrow |5P_{3/2},\ F = 2\rangle$ using an AOM in single pass configuration. It is used to spin-polarize the gas by optical pumping and for 'depumping' of the atomic loading beam (see Section 6.1).

The fourth beam (2.2 mW) split from the grating stabilized laser is shifted to the transition $|5S_{1/2}, F = 2\rangle \rightarrow |5P_{3/2}, F = 3\rangle$ with an adjustable detuning ranging from -65 to $+10$ MHz needed for magneto-optical trapping and sub-Doppler laser cooling of the atoms collected in the MOT. For this purpose a power exceeding 100 mW is desired (compare Section 5.2). This is realized using a 'broad-area diode laser' system (BAL) [Goldberg et al., 1993, Abbas et al., 1998, Gehring et al., 1998, den Boer et al., 1997, Praeger et al., 1998] has been set up. In this work the BAL was integrated in the laser system and has been demonstrated to be very useful and comparably cheap instrument for Bose-Einstein condensation experiments involving laser cooling and trapping [Shvarchuck

Purpose	Hyperfine transition of the D-2 line ($5S_{1/2} \rightarrow 5P_{3/2}$)	Range of detuning, (MHz)	Power, (mW)
1. Magneto-optical trap (MOT)	$F = 2 \rightarrow F = 3$	-70 to $+15$	130
2. Absorption imaging	"	"	"
3. Atomic beam source	"	-55 to $+70$	34
4. Optical pumping (OP)	$F = 2 \rightarrow F = 2$	0 , fixed	1
5. Probe	$F = 2 \rightarrow F = 3$	-70 to $+15$	1
6. Plug beam	"	"	0.5
7. Repumper beam source	$F = 1 \rightarrow F = 2$	0 , fixed	1.9
8. Repumper MOT	"	"	8
9. Repumper OP	"	"	0.4
10. Repumper probe	"	"	0.1

TABLE 3.1: *Overview over purposes and properties of the laser beams produced by the laser system.*

et al., 2000]. Here, the operation principle of the BAL setup is sketched: First, the light power is raised to the level of 34 mW by using an injection-lock laser. Aside from raising the power this has the advantage of producing a laser beam with a highly stable position and direction. This beam is then injected into a 2 W broad area laser diode and amplified in a double pass configuration to typically 400 mW. Typically the amplified output deviates strongly from a single spatial mode pattern. Thus, only 130 mW remain after spatial filtering by a single mode optical fiber. The intensity of the output beam from the BAL system can be adjusted by an electro-optical modulator (EOM, Gsänger, LM 0202 P) with an extinction ratio of 1 : 1000. While conserving the power, the light can be redirected to the side port of the EOM, while the power in the main beam used for the MOT is reduced. The beam exiting the side port is used for absorption imaging of the trapped atomic cloud (Section 3.5).

In order to provide laser power driving the repumping transition another grating stabilized diode laser identical to the first one is used. It is frequency stabilized to the transition $|5S_{1/2}, F = 1\rangle \rightarrow |5P_{3/2}, F = 2\rangle$ by using Doppler-free absorption spectroscopy together with a frequency modulation (FM) technique [Bjorklund et al., 1983, Drever et al., 1983]. The achieved line-width is 200 kHz. The laser beam (15.5 mW) is split four times for the different purposes given in Figure 3.1. As the repumping transition is driven resonantly and only weak saturation is necessary, low optical power is sufficient and no further amplification is needed. In case of the detection beam for the atomic beam source and the optical pumping beam the repumping beam is overlapped at beam splitters before spatial filtering takes place.

The properties of the different laser beams and their purposes are summarized in Table 3.1.

3.2 The vacuum system

The vacuum system is build on the optical table next to the laser system. It is shown in Figure 3.2, which is a combination of a technical drawing of the central part of the vacuum system and a schematics of the pump arrangement. The central part consists of two vacuum chambers build on top of each other. These are connected through a small differential pumping hole. The lower chamber is a rubidium vapor cell connected to a rubidium reservoir. This cell serves to realize the atomic beam source. The upper one is a ultra-high vacuum (UHV) chamber that consists of two parts, a quartz cell, around which the magnetic trap is build, and a metal manifold for pumping and monitoring of the atomic beam.

The vapor cell can be filled with rubidium vapor up to the saturated vapor pressure of rubidium at room temperature, approximately 6×10^{-7} mbar [Roth, 1990]. By heating the rubidium reservoir to a temperature of about 120 °C for a short while evaporated rubidium is slowly filled into the vapor cell. The vapor cell is pumped by a 2 l/s ion pump (Varian) and via the differential pumping hole connecting it to the UHV chamber. The UHV chamber is pumped by a 40 l/s ion pump (Varian). This pump is connected by a metal tube (CF40) with a conductance of of 60 l/s. It is installed in a distance of about 80 cm from the manifold. At this distance the distortion of the magnetic trapping field by the pump magnets may be neglected. For the same reason the vacuum chamber and the optical bread-board around it are made of non-magnetic metals such as stainless steel (316 Ti) and aluminum. In order to enhance the pumping speed for reactive gases (like alkalis, hydrogen, and air) by an order of magnitude a titanium sublimation pump (about 200 cm^2) has been installed in a side arm of the main tube. During pump down and bake out of the system a quasi-oil-free combination of membrane pump and turbo pump (Balzers, models TPU-062H and MZ-2T) is used, connected to the second port of the ion pump. During bakeout the vapor cell is pumped via a bypass valve. After baking the metal parts of the system to 350 °C and the glass parts to 200 °C for a few days the pressure dropped below the detection limit of 3×10^{-11} mbar of the ionization gauge (Varian, model UHV-24 nude, with X-ray enhanced detection limit). After activating the titanium sublimation pump this drop was observed to be more rapid. But it turned out, that it is not necessary to reactivate the pump in order to maintain the low pressure. In order to obtain a realistic reading of the pressure inside the UHV glass cell the ionization gauge was installed on the vacuum manifold. Ultimately, the life time of the atomic cloud in the magnetic trap (compare Section 6.3) is a decisive indicator for the quality of the vacuum.

The vacuum manifold is a standard cube (CF40) on top of a standard hexagon (CF16). To these metal parts two quartz cells are connected providing the experimental chambers with excellent optical access. To avoid multiple reflection of the laser beams in the cell walls, the walls carry an optical anti-reflection coating on the outer surfaces with a reflectivity lower than 0.2% for 0° incidence at 780 nm. The two glass cells consist of a rectangular part with a length of 65 mm and 150 mm respectively, and a square outer cross section of $30 \times 30\,mm^2$. The thickness of the walls is 4 mm. To allow a bakeout the cell is made out of quartz. For a Helium partial pressure of 5×10^{-3} mbar in the atmosphere a helium gas load through the cell walls of 1×10^{-12} mbar·l/s is calculated. In combination with a vacuum conductance of the cell of 10–20 l/s, this allows a sufficiently

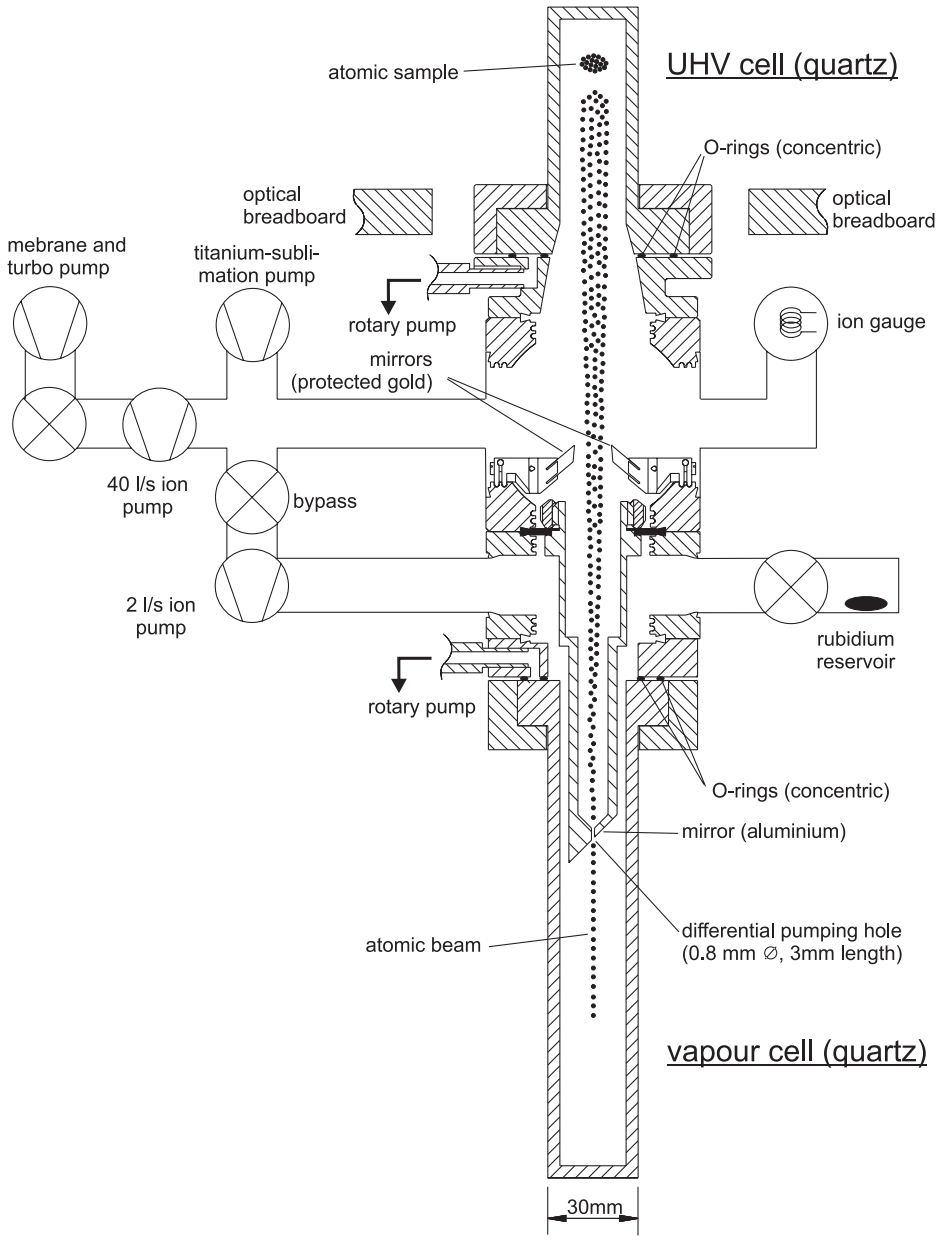

FIGURE 3.2: *Central part of the vacuum system (technical drawing) with two quartz cells as experimental chambers and arrangement of the pumps (schematics). The two chambers are connected by a differential pumping hole. The lower chamber contains rubidium vapor up to* 4×10^{-7} *mbar. In the upper ultra-high vacuum chamber a pressure lower than* 3×10^{-11} *mbar is achieved.*

low helium partial pressure inside the cell.

The rectangular parts of each cell is fused to a circular quartz disc with a central hole. The disc is clamped onto a metal flange. In first experiments a metal ring with a soft core and two knife edges (Carbone Lorraine, model Helicoflex Delta) has been used to provide a helium leak-tight glass-to-metal sealing. In this way a short non-magnetic glass to metal transition was realized leading to a distance between the atomic beam source and the magnetic trap of only 25.5 cm. This is of great importance for the recapture of the atoms from the divergent atomic beam (Section 5.2).

The glass to metal joint proved to be not reliabe. A finite element analysis of the stress inside the glass lead to a new design in which the force onto the clamps is applied in a more balanced way, and concentration of the stress at the corners of the rectangular part of the cell is avoided. However, from almost all groups in this field, which are using a similar design, broken cells have been reported. For the present work a differential pumping solution was used employing two concentric O-rings (Viton) as soft glass-to-metal sealing rings. After careful cleaning and prebaking of the rings the vacuum load originating from the O-rings is dominated by permeation of ambient gases through the rings. Between the pair of concentric rings a low vacuum of approximately 10^{-3} mbar was created by a rotary pump. This strongly reduces the permeation rate by six orders of magnitude. With this differential pumping method the permeation rate is estimated to be as low as 2×10^{-13} mbar·l/s, which does not limit the pressure in the chamber.

Inside the vacuum three optical mirrors are mounted, two covered with a protected gold coating and one consisting of polished solid aluminum. They allow to apply laser beams for cooling and trapping. The aluminum mirror is part of the wall separating the vapor cell from the UHV chamber. It has a central hole of 0.8 mm diameter and 3 mm length. This differential pumping hole allows a pressure ratio of about $\kappa = 3 \times 10^{-3}$ between the pressure in the UHV and the vapor cells.

As the atomic beam source is operated at comparably high rubidium partial pressure of 4×10^{-7} mbar (compare Chapter 4), it is important to consider the atomic flux through the trapping region that originates from the vapor cell when the atomic beam source is switched off. This flux should be small compared to the flux through the capture region originating from the UHV background. In the present geometry the solid angle which is covered by the differential pumping hole seen from the cloud is $\delta\Omega = 2 \times 10^{-7}$. A small calculation shows that the ratio of the background flux to the flux from the vapor cell can be estimated to be $\kappa/(4\,\delta\Omega) \approx 3 \times 10^3$. Thus, the direct flux from the vapor cell is negligible.

3.3 The Ioffe-quadrupole magnetic trap

The field geometry of the Ioffe-quadrupole type magnetic trap [Pritchard, 1983], as described by Equation (2.9), can be achieved by different configurations. The so called 'baseball' and 'three coil' configuration [Bergeman et al., 1987] require a low number of magnetic field coils and the 'cloverleaf' configuration [Mewes et al., 1996a] provides an good optical access in the radial direction. The Ioffe-quadrupole configuration can also be realized in miniaturized wire-traps [Reichel et al., 1999] contained inside the vacuum chamber.

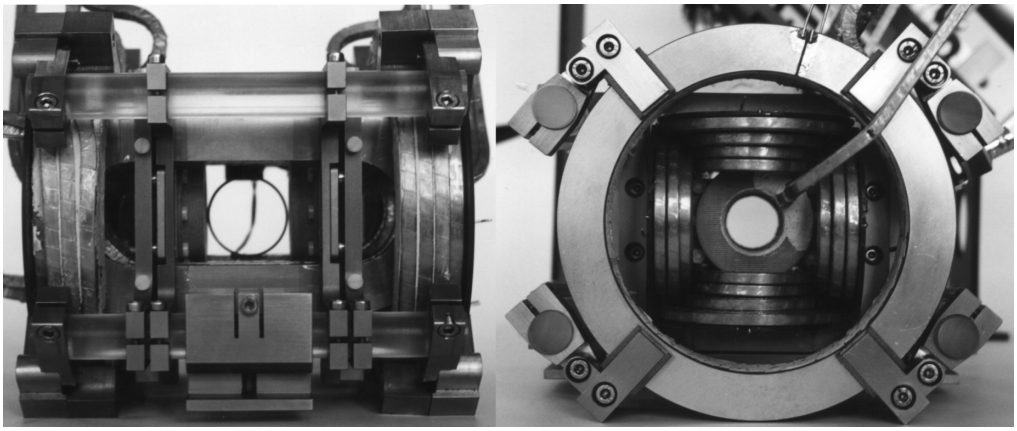

FIGURE 3.3: *Ioffe-quadrupole magnetic trap. Left: View along the radial direction. Right: View along the horizontal symmetry axis. The magnetic field coils are made of water cooled copper tubes dissipating* $5.4\,kW$ *at* $400\,A$*. The thermally stable mount is designed like a bench system with four quartz rods.*

The magnetic field coil configuration realized in this work is shown in Figure 2.3. It consists of eight individual coils, which are electrically and mechanically independent. This has a number of advantages: The strengths of the confinement in longitudinal and radial direction ('aspect ratio') can be controlled to a large extent independently. The current of one of the pinch coils can be reversed in order to create an anti-Helmholtz configuration used for the magneto-optical trap. By assembling the Ioffe-bars from four individual coils unwanted effect of the endings on the central magnetic field is minimized. Moreover, the mutual inductance between the Ioffe-coils and the dipole coils is minimized. By reducing the current in one of the four Ioffe coils, the center of the trap can be shifted in the radial direction (see Section 6.1). All coils are individually water cooled and suspended independently from four quartz rods in order to achieve high stability of the fields against thermal expansion of the coil system.

The actual magnetic trap, which is based on this coil configuration and built around the UHV glass cell, is shown in Figure 3.3. The design of the trap was optimized to provide strong confinement and rapid switching. This is best achieved with high currents and low self-inductance. Therefore, the coils have a low winding number and are made of water cooled copper tubes which allow a current of up to 400 A. To minimize the dead volume a choice was made for current wires with a square cross-section ($4 \times 4\,\mathrm{mm}^2$ for pinch and Ioffe coils, $5 \times 5\,\mathrm{mm}^2$ for the compensation coils) and thin ($25\,\mu\mathrm{m}$) capton isolation. Thus, it was possible to place the coils at a minimum distance to the cell (and the center of the trap) and to maximize the confinement. With a choice of the diameter of 2 mm (pinch and compensation coils) and 2.5 mm (compensation coils) of the hole used for water cooling a minimum rise in temperature has been realized. The cooling water is distributed to the coils in parallel, even where the coils are electrically connected in series. With a total throughput of $100\,\mathrm{cm}^3/\mathrm{s}$ (at 4.5 bar) and a current of 400 A the

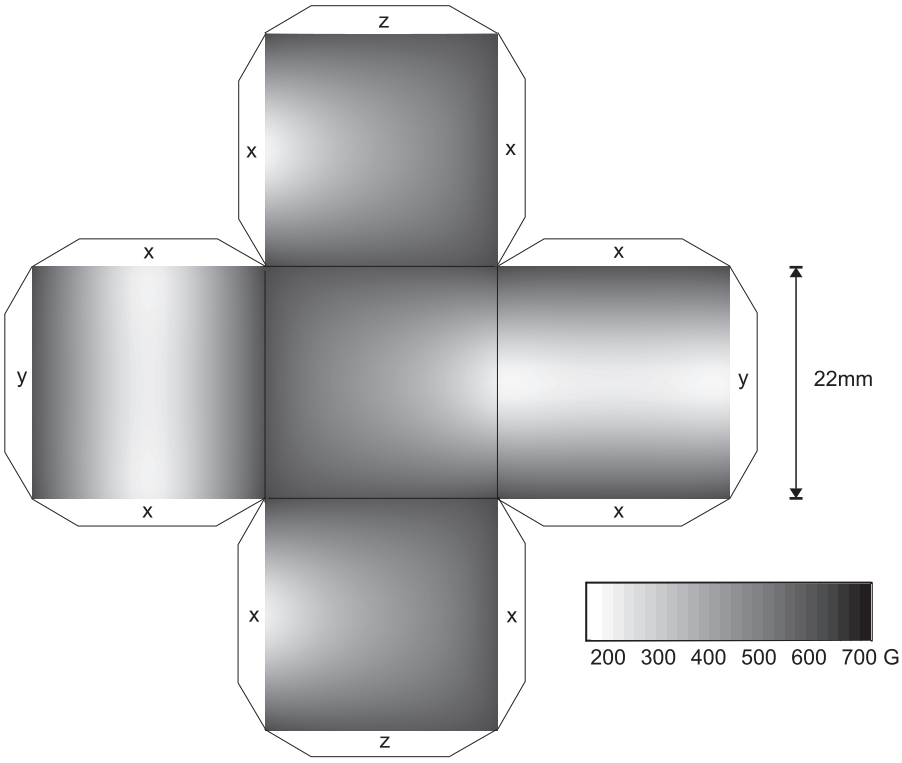

FIGURE 3.4: *The absolute magnetic field (calculation) at the walls of the vacuum cell (unfolded cube geometry with x-y-plane as the top plane of the quartz cell). Four equal minima in the x-y-planes, occurring where the field from the pinch coils is maximally cancelling the quadrupolar field, limit the trap depth to* 180 *G. This corresponds to a potential depth of* 12 *mK.*

total power dissipation by the coils is 5.4 kW (9.8 kW including the switching elements) causing an average rise of 10 K of the coil temperature.

All coils are rigidly mounted to an optical breadboard (see Figure 3.2), on which the optical setup for the MOT and as well as the imaging system are mounted.

Before installing the magnetic trap around the UHV cell, the magnetic field was tested by means of a Hall-probe. At a maximum current of 400 A a radial gradient of the quadrupole field of 353 G/cm and a curvature of 286 G/cm^2 of the field along the symmetry axis are achieved. The central magnetic field of 350 G produced by the pinch coils is compensated by the compensation coils. The distance between the two compensation coils is adjusted so that the central field fully compensated when driving also these coils at 400 A. Fine adjustment of the central magnetic field around typical values of a few Gauss is realized by changing the current in the compensation coils by means of a variable bypass resistor R. The small influence of the Ioffe coils on z-component of the central magnetic field has been measured to be -4.2 mG/A.

Choosing a central magnetic filed of 0.85 G the trap frequencies for the trapped state $|F = 2, m_F = 2\rangle$ are calculated from Equations (2.11) and (2.12) to be $\omega_z = 2\pi \cdot 21.6\,\mathrm{Hz}$ and $\omega_\rho = 2\pi \cdot 486.6\,\mathrm{Hz}$.

The depth of the magnetic trapping potential is limited by the value of the magnetic field at the walls of the UHV glass cell. In Figure 3.4 the absolute value of the magnetic field at the walls is shown in form of a density plot. In the planes perpendicular to the z-axis of the trap two magnetic field minima limit the depth of the magnetic field to a value of 180 G corresponding to 12 mK, if the trapped state $|F = 2, m_F = 2\rangle$ is considered. The minima are located, where the radial component of the field originating from the pinch coils is maximally compensating the quadrupole field.

The magnetic trap is controlled by the electronic setup sketched in Figure 3.5. The current is delivered by commercial high power supplies, A–C (Hewlett Packard, model HP6681A). The pinch coils are driven in series with the compensation coils, and so the fluctuations of the central magnetic field $\Delta B_0/B_0$ due to the current noise ($\Delta I/I \lesssim 10^{-3}$) of the power supplies are on the same order as the current noise and can be neglected. The value of the central field can be tuned by changing the current in the compensation coils by means of a variable bypass resistor, which for the sake of stability is consisting of a set of stable high power resistors (100 ppm/°C) mounted on a water cooled panel.

The current in the coils can be controlled in two ways: First, the programming voltage and current inputs of the power supplies can be controlled by analog outputs of the computerized automation system. Second, the current in te paths A–E can be controlled by IGBTs (IXYS, model IXGN200N60A). The characteristic curve of current vs. gate voltage of the IGBTs was measured. This allows accurate control of the IGBT currents by computer controlled adjustment of the gate voltage. Fast 'switch-off' of the currents can be performed by the IGBTs with help of the diodes D1–D6 (IXYS DSEI2×101) and the capacitors C1 and C2 preloaded to a constant voltage of $U = 200\,\mathrm{V}$. As the self inductance L of the Ioffe coils and the pinch + compensation coils are 26.5 μH and 32.8 μH respectively, the current of $I = 400\,\mathrm{A}$ is typically measured to vanish within $L \cdot I/U \approx 60\,\mu\mathrm{s}$. During the switching of the compensation coils a cross current through the bypass resistor is prevented by a the use of the additional dummy coil $L_d \approx 300\,\mu\mathrm{H}$ which produces the same but reverse voltage peak during switching as the compensation coils. The 'switch on' time is on the order of a few ms. It is determined by the regulation circuit and the maximum voltage (8 V) of the power supplies. As for some experiments fast switching of moderate currents through the pinch coils (80 A in 300 μs) is essential, an additional fast switching power supply D (Power Ten Inc.) and IGBT switches have been included in the design.

For driving the pinch coils in anti-Helmholtz configuration path A and C are used and the power supplies B and C deliver twice the current of supply A. The Ioffe coils are driven by two more power supplies of the same type. The shift of the quadrupole axis has been realized by partially bypassing the Ioffe coil number 1 with the help of the path D.

In order to fine tune the trapping fields, some additional shim coils are available. These coils consist of PCB boards having the same loop-like shape as the Ioffe and the compensation coils being directly mounted on top of them (compare Figure 3.3). With the copper layer on both sides of the boards loops with two windings are realized. These

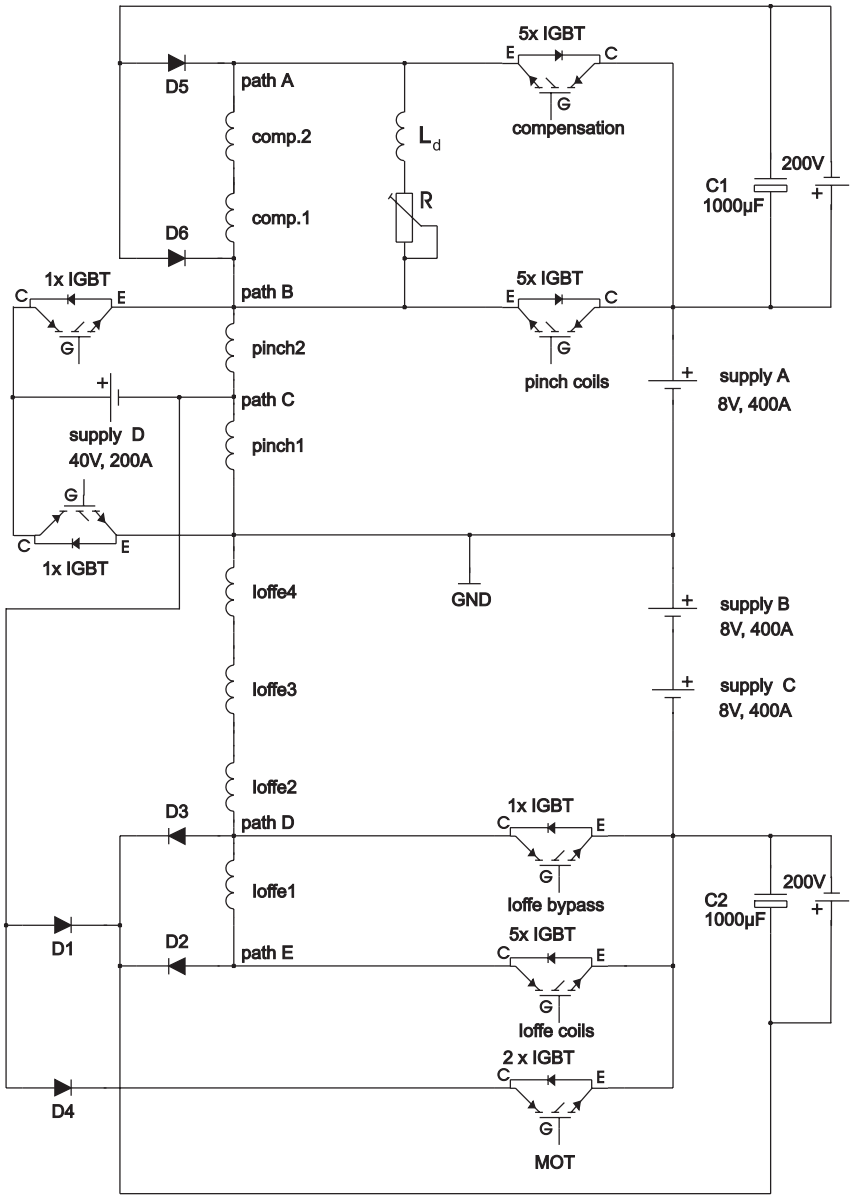

FIGURE 3.5: *Control circuit of the magnetic trap: The* 8 *coils of the trap carry currents up to* 400 *A. The currents are controlled by programming the power supplies and using the IGBT switches. The different paths A–E are used for the operation of the MOT, the compression of the magnetic trap and the compensation of the gravitational shift of the trap center.*

nominal current	400 A
gradient	$\alpha = 353\,\mathrm{G/cm}$
curvature	$\beta = 286\,\mathrm{G/cm^2}$
B_0-offset due to Ioffe coils	$-4.2\,\mathrm{mG/A}$
axial trap frequency	$\omega_z = 2\pi \cdot 20.6\,\mathrm{Hz}$
radial trap frequency	$\omega_\rho = 2\pi \cdot 477.4\,\mathrm{Hz}$ (at $B_0 = 0.85\,\mathrm{G}$)
switch-off time	$60\,\mu\mathrm{s}$
power dissipation	5.4 kW (coils), 4.4 kW (IGBT switches)
temperature rise	10 K on average

TABLE 3.2: Properties of the Ioffe-quadrupole trap: The given measured trap frequencies are in good agreement with the values calculated from the measured magnetic trapping parameters.

shim coils are, for example, used to modulate the magnetic trapping potential during the measurement of the trap frequencies (compare Section 6.4).

The properties of the magnetic trap are summarized in Table 3.2.

3.4 The radio frequency source

For evaporative cooling an oscillatory magnetic field ramped down in frequency from 50 MHz to 600 kHz is applied to the atoms. Therefore, a tunable broad band radio-frequency (rf) source was build [Valkering, 1999]. The rf-signal is generated by a frequency synthesizer (Wavetek, model 80). The frequency ramp is performed either with a voltage controlled oscillator (VCO) input or using the internal linear sweep of the generator. Using two of the analog outputs of the computer interface, the VCO input provides the possibility of using arbitrary waveforms for the ramp. The control signal is produced by adding the two signals from the analog outputs (12-bit resolution) with different gains. Coarse adjustment of the frequency is done in steps of 20 kHz to cover the desired frequency range, whereas fine adjustment in steps of 1 kHz is used at the final stage of the ramp. However, in this mode drifts of typically a few kHz on a time scale of an hour are observed. As this drift only occurs using the full dynamic range of the VCO, this problem can be circumvented by using the internal sweep generator for the initial ramp down and the VCO for the final stage (10 %) of the ramp. In most experiments only the VCO was used. The signal amplitude is set under (analog) computer control using a 60 dB variable attenuator. At the output of the attenuator the signal can be switched by a mechanical relays with a switching time faster than one millisecond. The signal is then amplified by 43 dB to yield a maximum power of 20 W into 50 Ω. For this we use an rf-power amplifier (Amplifier Research, model 25A250A).

The amplifier is connected to an rf-antenna located next to the quartz cell at a distance of 16 mm from the trap center (see Figure 3.3). The direction of the oscillatory magnetic field in the central region of the trap is pointing in horizontal direction perpendicular to the static magnetic field in order to obtain σ-polarization (compare Section 2.5.2).

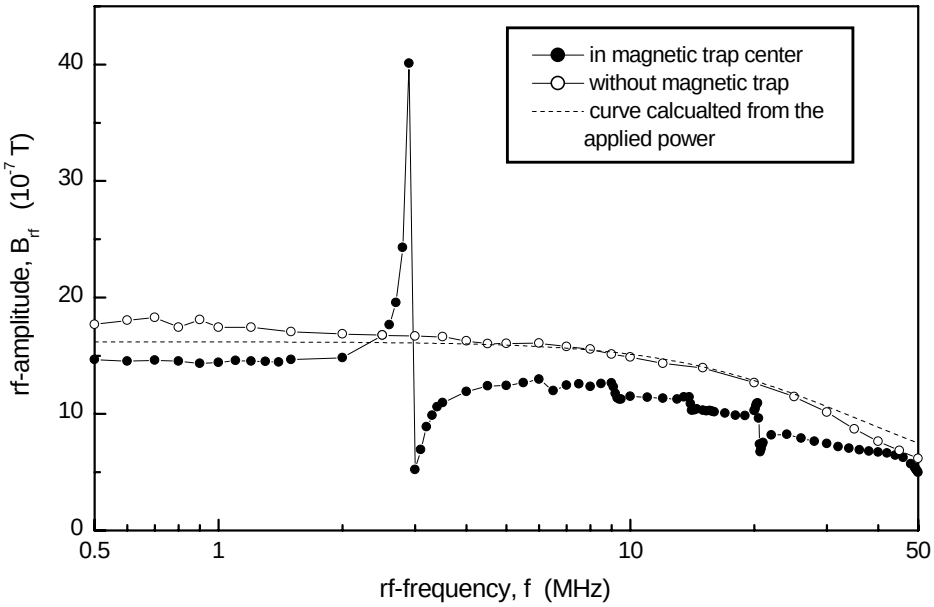

FIGURE 3.6: *Oscillatory magnetic field at the trap center radiated from the antenna. The value calculated on the basis of the power delivered to the antenna (dashed line) is compared to the measurements with a 'pick-up' coil (open circles). In the presence of the magnetic trap resonances occur (solid circles).*

The antenna is a coil with two loops with a diameter of 31 mm and is made of copper wire with a thickness of 1 mm. The diameter of the coil preserves good optical access to the trap (Figure 3.3, left), whereas the winding number was chosen to achieve the largest magnetic field at the upper edge of the frequency band. An identical coil used as a 'pick-up coil' is mounted directly onto the antenna. The signal received from this coil is connected to a 50 Ω input of a spectrum analyzer. In this way the power delivered to the antenna can be measured. Moreover, the two coils act as a 1 : 1 transformer, which in combination with the 50 Ω load improves the overall impedance matching to the amplifier.

The magnitude of the rf magnetic field in the trap center as a function of frequency was measured before installation of the trap assembly around the quartz cell. For this purpose, an 11 mm diameter pick-up coil was used replacing the sample in the center of the trap. The results are shown in Figure 3.6. Except for a resonance at 3 MHz the response is more or less flat and in fair agreement with the response calculated for the two coils in the absence of the trap assembly. Measuring the rf field in the absence of the trap assembly reveals that the resonance originates from mutual inductance with the trap coils.

3.5 The imaging system

For detection of the cloud absorption imaging is used. The general configuration is shown in Figure 5.1. The laser beam used for detection is spatially filtered by an optical single-mode fiber. After collimation, the beam passes horizontally, along the radial direction of the magnetic Ioffe trap through the UHV quartz cell, which contains the atomic cloud. The optical setup used for absorption imaging of the atomic cloud is shown in Figure 3.7. An image of the shadow of the cloud is created outside the vacuum chamber using a relay telescope of unit magnification ($M = 1$). This image is magnified by a microscope objective and thrown onto a CCD camera (Princeton Instruments, model TE/CCD-512EFT). Three different magnifications, $M = 0.25$, $M = 2.39$, and $M = 4$, have been used to match the image of the atomic cloud after release from the MOT and from the magnetic trap with the size of the CCD array (EEV 512×512 FMTR, $7.7\,\mathrm{mm} \times 7.7\,\mathrm{mm}$). The $M = 0.25$ is used for imaging of clouds released from the MOT. For clouds released from the magnetic trap $M = 2.39$ and $M = 4$ are used. The optical resolution of the imaging setup is given by $1.22\,\lambda/\mathrm{NA} = 6\,\mu\mathrm{m}$, where $\mathrm{NA} = 0.15$ is the numerical aperture of the telescope and $\lambda = 780\,\mathrm{nm}$ is the wavelength of the light. The $15\,\mu\mathrm{m} \times 15\,\mu\mathrm{m}$ size of the CCD pixels corresponds to $6.28\,\mu\mathrm{m}$ (M=2.39) in the object plane. The resolution and the magnification have been measured with the help of a calibrated test pattern replacing the cloud. The use of the telescope allows the application of a standard microscope objective with a small working distance. Moreover, by inserting a phase plate in the center of the telescope phase-contrast imaging method for non-destructive imaging [Andrews et al., 1996] of the atomic cloud can be applied.

In the following the typical parameters for the detection are discussed. Detection is done on the $5S_{1/2}, F = 2 \rightarrow 5P_{3/2}, F = 3$ transition (see Table 3.1). Following Lambert-Beer's law one can write the intensity distribution $I(y, z)$ of the detection light after

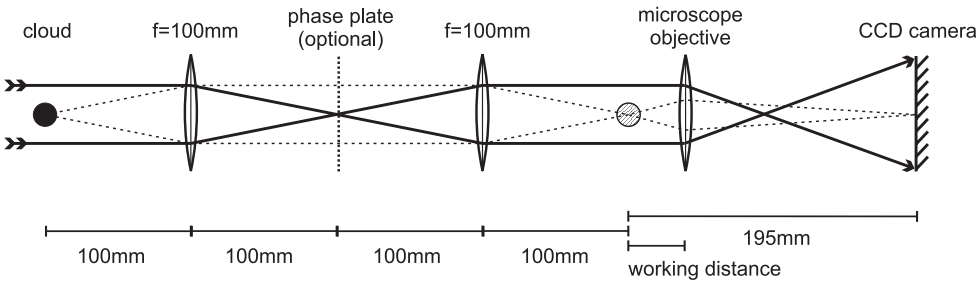

FIGURE 3.7: *Setup for absorption imaging: The atomic cloud creates a shadow in the center of the collimated detection beam. The confocal relay telescope creates an intermediate image of the cloud outside the vacuum cell. This allows the use of microscope objectives with short working distance. The magnified image is detected by a CCD camera. By inserting a phase-plate in the center of the telescope phase-contrast imaging can be applied.*

passing through the cloud as

$$I(y,z) = I_0(y,z)\,\mathrm{e}^{-D(y,z)} \quad , \tag{3.1}$$

where $I_0(y,z)$ is the intensity distribution of the detection beam before the absorption. The optical density profile

$$D(y,z) = \sigma_\pi\,\eta(y,z) \tag{3.2}$$

is given by the integrated density profile $\eta(y,z)$ of the density $n(x,y,z)$ of the cloud along the line of sight

$$\eta(y,z) = \int \mathrm{d}x\; n(x,y,z) \quad , \tag{3.3}$$

and the photon absorption cross section σ_π. As the detection light is linearly polarized, the cross section averaged over the possible π-transitions has to be considered, yielding

$$\sigma_\pi = \frac{7}{15}\,\frac{3\lambda^2}{2\pi}\,\frac{1}{1+(2\delta/\Gamma)^2} \quad . \tag{3.4}$$

The cross section depends on the detuning δ of the detection laser. Thus, with the choice of the detuning the desired optical density can be adjusted for a given $\eta(y,z)$. The 12-bit resolution of the analog to digital conversion of the CCD signal limits the detectable optical density to $D = 8$. In practice the observable optical density was limited to about $D = 5$, probably due to spectral background in the detection beam and scattered light in the optical path. By allowing a maximum optical density of 2.5, these effects could be neglected. At this optical density the photon-shot noise becomes of the order of the read-out noise of the camera.

In order to avoid blurring of the images of the expanded cloud the exposure time was typically set to $\tau = 200\,\mu$s, which is much shorter than the typical expansion time of 10 ms of the cloud. The intensity of the detection beam of $600\,\mathrm{mW/cm^2}$ for M=2.39 is then chosen to fully exploit the 130000 electrons well depth of the CCD pixels. The CCD chip has a specified quantum efficiency of 45 % at 780 nm. This intensity corresponds to weak saturation of the optical transition of typically $S_0 = 0.026$ at a detuning of -10 MHz. During the detection typically $N_\mathrm{p} = 100$ photons are scattered from each atom. The RMS displacement due to photon recoil transverse to the line of sight can be estimated with the recoil velocity of $v_\mathrm{rec} = 5.9\,\mathrm{mm/s}$ to be $\sqrt{N_\mathrm{p}/3}\,v_\mathrm{rec}\tau = 6.5\,\mu$m, [Ketterle et al., 1999]. As this is on the order of the of the optical resolution, it is neglected in the spatial analysis.

In order to extract the density profiles from the CCD images it is not necessary to measure the absolute intensity at the CCD camera, and to consider e.g. reflection loss at the imaging optics. Measurements of relative intensities $I(y,z)/I_0(y,z)$ suffice for this purpose. These are accurately measured by taking three images in the following way: First, an absorption image $I_\mathrm{abs}(y,z)$ of the cloud is taken in the manner described above. After the cloud dropped out of the field of view a second so called 'flat field' $I_\mathrm{ff}(y,z)$ image is taken with the same exposure. Afterwards, a third image is taken to record the background $I_\mathrm{bg}(y,z)$ without atomic cloud and without detection beam. The correct intensity ratio is then obtained by first subtracting the background image values before normalizing the absorption image to the flat field image as $I(y,z)/I_0(y,z) =$

$(I_{\mathrm{abs}}(y,z) - I_{\mathrm{bg}}(y,z))/(I_{\mathrm{ff}}(y,z) - I_{\mathrm{bg}}(y,z))$. In order to avoid systematic effects from the drift of the detection intensity, this procedure is repeated each time the density profile of an atomic cloud is measured.

Chapter 4

Two-dimensional magneto-optical trap as a source of slow atoms

This chapter has been published as:
Two-Dimensional Magneto-optical Trap as a Source of Slow Atoms,
K. Dieckmann, R. J. C. Spreeuw, M. Weidemüller and J. T. M. Walraven,
Physical Review A, **58**, 3891 (1998).

4.1 Abstract

We experimentally study the use of two-dimensional magneto-optical trapping (2D-MOT) for the generation of slow beams of cold atoms out of a vapor cell. A particularly high flux of 9×10^9 rubidium atoms/s at a mean velocity of 8 m/s, is obtained using a combination of magneto-optical trapping in two dimensions and Doppler cooling in the third dimension ($2D^+$-MOT). The resulting width of the velocity distribution is 3.3 m/s (FWHM) with a beam divergence of 43 mrad (FWHM). We investigate the total flux as a function of vapor cell pressure and determine the velocity distribution of our slow atom sources. For comparison, we also realized a Low-Velocity Intense Source (LVIS), first reported by Lu *et al.* [Phys. Rev. Lett. **77**, 3331 (1996)]. We find that the $2D^+$-MOT yields a significantly higher flux than the LVIS, even when used with an order of magnitude less laser power.

4.2 Introduction

Optical cooling and trapping in two dimensions have been applied successfully to the brightening of fast atomic beams [Riis et al., 1990, Nellessen et al., 1990, Scholz et al.,

1994]. The atomic beam is compressed and the atomic motion cooled in the two directions transverse to the beam axis. This two-dimensional cooling principle has been called an "atomic funnel", or also two-dimensional magneto-optical trap (2D-MOT). It is less well established that two-dimensional cooling, besides for the *brightening* of atom beams, is also a powerful technique for the *generation* of slow (< 30 m/s) atom beams. The generation of intense sources of slow atomic beams is of great interest for experiments on Bose-Einstein condensation [Anderson et al., 1995, Davis et al., 1995, Bradley et al., 1995]. One of the earliest and widely used techniques, is to slow down atoms from a thermal oven using the Zeeman slowing technique [Phillips and Metcalf, 1982]. More recently there have been efforts to use optical cooling techniques to extract slow atomic beams from low-pressure vapor cells. The most intense source of this kind so far, the so-called low-velocity intense source (LVIS) [Lu et al., 1996], is based on three-dimensional cooling.

In this paper we study two-dimensional cooling configurations which extract a beam of slow atoms directly out of a vapor cell. Although a two-dimensional cooling configuration seems an obvious geometrical choice for beam generation, experimental work has been limited. A two-dimensional technique achieving a relatively low flux of slow atoms has been demonstrated recently by Weyers *et al.*[Weyers et al., 1997]. A similar method to generate a very slow beam was recently described by Berthoud et al. [Berthoud et al., 1998]. We report here the experimental realization of two vapor-cell based sources for a slow and intense atomic beam, based on two-dimensional trapping and cooling. Our brightest source is based on a combination of a 2D-MOT and unbalanced optical molasses in the third, longitudinal direction ($2D^+$-MOT configuration). It yields a flux of slow atoms comparable to the LVIS [Lu et al., 1996], but requires an order of magnitude less laser power than employed in the original realization of the LVIS. We realized the LVIS with low laser power, so that we can compare the performance of the sources directly.

4.3 Experimental setup and principle of operation

The experimental setup is based on a two-chamber vacuum system. A rubidium vapor cell is formed by a rectangular quartz cuvette ($30\times30\times150$ mm^3). The vapor pressure is varied between a few 10^{-9} mbar and 5×10^{-7} mbar by heating a rubidium reservoir connected to the vapor cell. The vapor pressure is measured with a calibrated photo diode detecting the fluorescence induced by a laser beam of 1.4 mW power and 7 mm waist. The atom beam leaves the vapor cell in the upward vertical direction through a 0.8 mm diameter hole. It then enters an ultra high vacuum chamber where it is analyzed. The small hole at the same time allows for differential pumping.

The principal part of our experimental setup around the vacuum system is shown in Figure 4.1. Two sets of coils placed around the vapor cell are used to produce the desired inhomogeneous magnetic fields. A set of four racetrack shaped coils generates a cylindrical quadrupole field with a line of zero magnetic field along the symmetry axis. This quadrupole field is used for the 2D-MOT and $2D^+$-MOT configurations. A pair of anti-Helmholtz coils generates a spherical quadrupole field used in the LVIS.

The laser system consists of 50 mW diode lasers which are linewidth-narrowed by optical feedback from an external grating and frequency-stabilized by electronic feedback

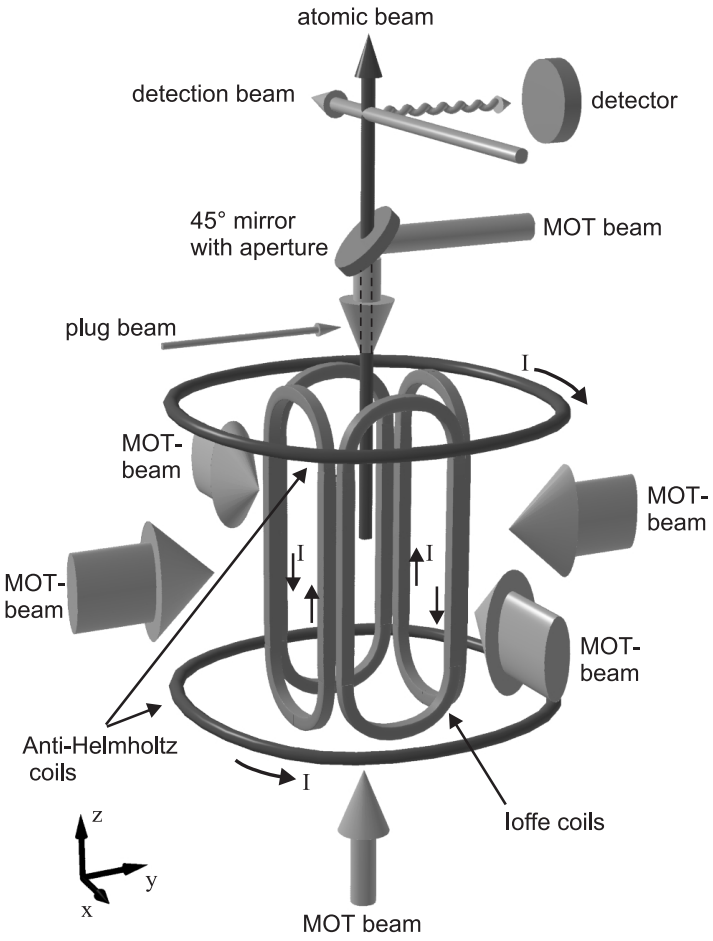

FIGURE 4.1: *Experimental setup: The rubidium vapor cell from which the atomic beam is extracted is located inside the four racetrack shaped magnetic field coils. These so called Ioffe-coils produce a two-dimensional quadrupolar magnetic field are used in the 2D-MOT and 2D$^+$-MOT configurations. The anti-Helmholtz coils are used for the three-dimensional quadrupolar field necessary for the LVIS configuration. The vertical MOT-beams used for the 2D$^+$-MOT and the LVIS are absent in the 2D-MOT case. After passing through an aperture in a 45 mirror into a ultrahigh vacuum chamber the atomic beam is detected by means of fluorescence.*

from Doppler-free saturated absorption spectroscopy in a Rb cell. The first, "cooling and trapping," laser is tuned a few linewidths to the red of the $5S_{1/2}, (F = 2) \rightarrow 5P_{3/2}, (F = 3)$ transition in ^{87}Rb. This laser acts as a master, to which another low power diode laser is slaved by injection locking, yielding a power of 34 mW filtered into a TEM_{00} mode. The second, "repumping," laser is resonant with the $5S_{1/2}, (F = 1) \rightarrow 5P_{3/2}, (F = 2)$ transition and is used for hyperfine repumping. The lasers and field coils are used in

three different combinations (2D-MOT, 2D$^+$-MOT and LVIS), using the experimental parameters listed in Table 4.1.

For the 2D-MOT we use two pairs of retroreflected cooling beams ($\sigma^+ - \sigma^-$ polarization). These beam pairs are perpendicular to each other and to the atomic beam axis, defined by the (vertical) line of zero magnetic field of the cylindrical quadrupole coils. The laser beams have an elliptical cross-section, with the larger waist $w_z = 24$ mm along the atomic beam axis and the smaller waist $w_\rho = 7$ mm perpendicular to it. Rubidium atoms from the background vapor passing through the cooling fields are cooled and driven towards the symmetry axis. Their velocity component v_z along the axis is conserved, since all cooling beams exclusively propagate in the horizontal plane. From this two-dimensional version of the magneto-optical trap (2D-MOT) two atomic beams emerge upwards and downwards, respectively, along the symmetry axis. Atoms with a high longitudinal velocity v_z do not spend enough time in the laser fields to be sufficiently cooled in the transverse direction. These atoms are filtered out by the 0.8 mm aperture. Because of this "filtering" for short interaction times the longitudinal velocity of atoms in the beam is small compared to the average velocity of atoms in the background of 270 m/s.

The 2D$^+$-MOT is an extension of the 2D-MOT, where we apply an additional pair of laser beams in the vertical (z) direction. The extra pair of beams cools the axial velocity v_z and thus enhances the capture of atoms with a large v_z. The intensities of the two vertical beams are adjusted independently. The highest atomic flux is found if the upward propagating beam is more intense than the downward one, so that radiation pressure is unbalanced, pushing the atoms upwards through the 0.8 mm whole. We used 0.6 mW of power in the downward beam and 2.1 mW in the upward beam, both beams having a waist of 7 mm. Furthermore, the downward propagating beam enters the vacuum from

	2D-MOT	2D$^+$-MOT	LVIS
Detuning δ	-1.7Γ	-3Γ	-3.3Γ
Field gradient:			
$\mathrm{d}B/\mathrm{d}z$ [G/cm]	0	0	13.6
$\mathrm{d}B/\mathrm{d}\rho$ [G/cm]	17.7	12.6	6.8
Laser waists:			
w_ρ [mm]	7	7	7
w_z [mm]	24	24	7
Laser power:			
$P\downarrow$ [mW]:	0	0.64	3.8
$P\uparrow$ [mW]:	0	2.1	5.2
$P\leftrightarrow$ [mW]:	16.4	15	10.4

TABLE 4.1: Experimental parameters of the three source configurations: Laser detuning is given in units of the natural linewidth ($\Gamma \approx 2\pi \times 6$ MHz). Magnetic field gradient and waist (radius at $1/e^2$ fraction of peak intensity) as well as power of the laser beams refer to the vertical (z,$\uparrow$,$\downarrow$) and horizontal (ρ,$\leftrightarrow$) direction.

the side and is reflected downward by a 45° aluminum mirror, in the center of which the 0.8 mm exit hole is drilled. Therefore the downward propagating beam contains a shadow along the axis so that atoms close to the axis are strongly accelerated out of the capture region by the upward propagating beam. We would like to notice here, that the two vertical laser beams have equal detunings as the transverse beams. A separate detuning of the vertical beams could lead to an enhanced axial capture velocity and thus a higher atomic flux.

For the LVIS, six intensity-balanced circularly polarized laser beams are combined with the spherical quadrupole field of the anti-Helmholtz coils. Also in the LVIS the downward propagating beam contains a shadow along the axis and atoms are driven out of the capture region by radiation pressure from the upward propagating beam. All laser beams have a circular cross-section with a 7 mm waist, limited by the available laser power. Due to this relatively small waist, the optimum magnetic field gradient is relatively large, $dB/dz = 15$ G/cm, about a factor three larger than in the original experiment by Lu *et al.* [Lu et al., 1996].

4.4 Diagnostics

The resulting cold atom beams are analyzed by detecting the fluorescence from a resonant probe laser beam located 130 mm above the exit hole. The probe has a power of 1 mW and a waist of 0.3 mm. A second, overlapping, beam with a power of 80 μW is used for hyperfine repumping. The fluorescence is measured using a calibrated photomultiplier tube (Hamamatsu 928). The photomultiplier signal is a measure for the local density of atoms passing through the probe beam. By translating the position of the narrow detection beam, the transverse density profile of the atomic beam can be resolved, and thus the divergence can be determined.

The longitudinal velocity distribution of the atomic beam is measured using a time-of-flight method, by suddenly switching off the atomic beam. This is accomplished by switching on an additional resonant "plug" laser beam that pushes the atoms away from the axis before they reach the exit aperture. From the time dependence of the decaying fluorescence signal $S(\tau)$ after switching off the atomic beam, the longitudinal velocity distribution $\Phi(v)$ can be deduced. Since the atom beam propagates vertically, the velocity distribution changes under the influence of gravity. The velocity distribution of the atom flux at the position of the plug beam is given by

$$\Phi(v) = -\frac{\tau}{\eta}\frac{d\,S(\tau)}{d\tau} \quad \text{, with} \quad v = \frac{L}{\tau} + \frac{g\tau}{2} \quad . \tag{4.1}$$

Here η is a calibration factor of the detection system, $L = 135$ mm is the distance between the plug and detection beams and g is the acceleration due to gravity. The integral $\int \Phi(v)dv$ gives the total flux in atoms/s.

4.5 Beam profiles and velocity distributions

The measured transverse density profiles of the atomic beams can well be fitted by a Gaussian. In the 2D-MOT and the 2D$^+$-MOT we observe atomic beam divergences

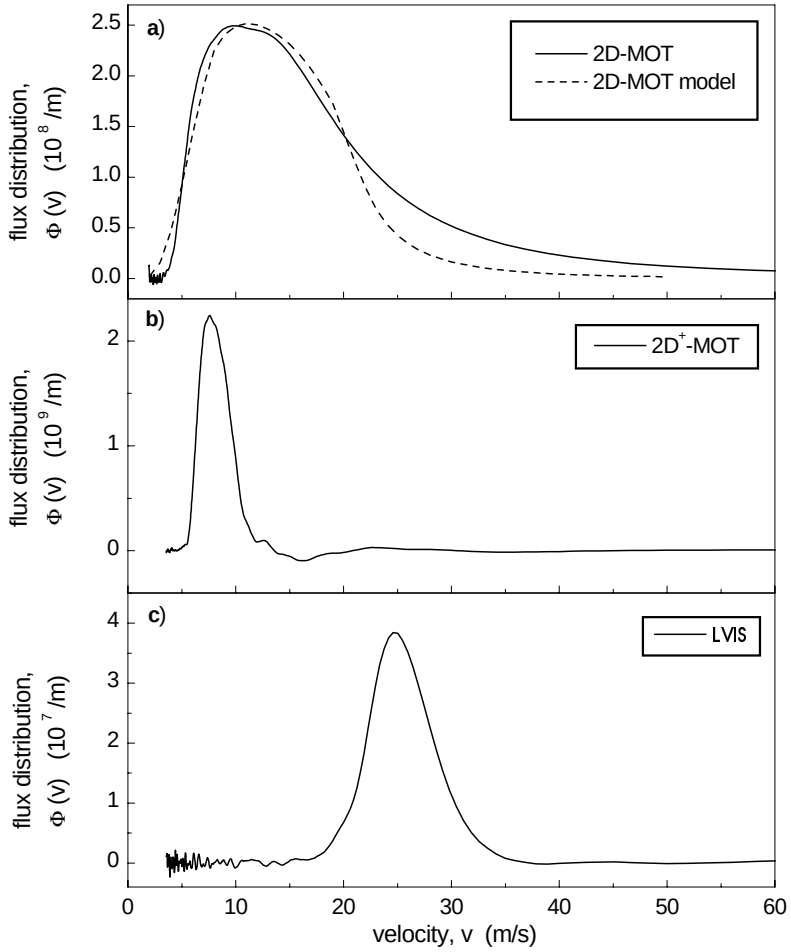

FIGURE 4.2: *Velocity distributions* $\Phi(v)$ *of the flux. a) Comparison of 2D-MOT and our simple model, b)* $2D^+$*-MOT, c) LVIS. The data are obtained by taking the derivative of the time-resolved photo multiplier signal (Equation (4.1)). The curves were measured at different background pressure in order to optimize the respective flux (Figure 4.3, a)). The small dip towards negative flux in b) around* $v = 17$ *m/s is an artifact resulting from a fluctuation of the time-of-flight signal.*

of 46 mrad and 43 mrad (FWHM), respectively, in the LVIS we find a smaller beam divergence of 27 mrad (FWHM). In all cases the value of the beam divergence seems to be limited geometrically by the angle subtended by the 0.8 mm exit hole as seen from the trapping region. Note that in our apparatus the distance from the edge of the trapping region to the exit hole is the same for the 2D-MOT and $2D^+$-MOT, but about twice as large for the LVIS, as we use different waists for the transverse laser beams (Table 4.1).

The measured velocity distributions of the flux $\Phi(v)$ at the level of the plug beam are shown in Figure 4.2. For the $2D^+$-MOT and LVIS the distributions are close to Gaussian, centered at a nonzero value. These distributions are determined by the *longitudinal* cooling process and subsequent acceleration out of the trapping region, by radiation pressure. There is a striking difference in average velocity - the mean value of the distribution $\Phi(v)$ - between the beams produced by the $2D^+$-MOT (8 m/s) and LVIS (26 m/s). This is due to the different intensities of the upwards propagating beams used in both cases, by which the atoms are accelerated out of the trapping region (Table 4.1). In both cases we observe a slight decrease of the mean velocity with increasing vapor pressure. If the pressure is increased, the atomic beam becomes optically dense. Thus, the radiation pressure from the upward propagating beam is reduced, which accelerates the atoms traveling in the shadow of the downward propagating beam. The widths (FWHM) of the velocity distributions of the $2D^+$-MOT and the LVIS are 3.3 m/s and 6.3 m/s. As the radiation pressure accelerating the atomic beam is higher in case of the LVIS, the velocity distribution of the LVIS is broader than that of the $2D^+$-MOT. In both cases we observe a reduction of the width of the velocity distributions with increasing pressure, i.e. with decreasing radiation pressure.

The flux distribution of the 2D-MOT is entirely different, because in this case there is neither longitudinal cooling nor an acceleration out of the trapping region. The velocity distribution here is determined by the *transverse* rather than the longitudinal cooling process. The basic features of the distribution are reproduced by a simple transverse cooling model, as will be discussed below.

4.6 Total flux and influence of collisions

The total flux of each of the the three atomic beam sources has been measured as a function of the rubidium vapor pressure. The pressure was varied up to the saturated vapor pressure at room temperature of about 4.8×10^{-7} mbar. The results are shown in Figure 4.3, a). In the absence of collisions the total flux should be proportional to the rubidium pressure. In all three cases this is indeed observed at low vapor pressure. In this regime the LVIS configuration produces a higher atomic flux than the 2D-MOT and $2D^+$-MOT. The LVIS works more efficient because of the presence of an optical confinement in all three directions. Atoms in the beam which do not travel collinear with the shadow of the downwards propagating beam enter the light field again. Due to the restoring force in all directions these atoms will be driven to the center again. Because of this *recycling* effect, almost all atoms, once captured, eventually are extracted via the exit hole [Lu et al., 1996]. By contrast, such atoms in the beam which do not pass through the exit hole, are lost in the 2D-MOT and $2D^+$-MOT cases.

At higher vapor pressure the measured curves deviate from a linear relationship. This shows, that collisions play a very important role in both the $2D^+$-MOT and the LVIS, causing the total flux to decrease as the pressure exceeds an optimum value. The LVIS reaches its maximum flux of 3×10^7 atoms/s at a vapor pressure of 2×10^{-8} mbar. The $2D^+$-MOT reaches its maximum flux of 9×10^9 atoms/s at a vapor pressure of 1.5×10^{-7} mbar. This flux is comparable to the original LVIS source reported by Lu *et al.* [Lu et al., 1996], but requires an order of magnitude less laser power. Thus, for a given

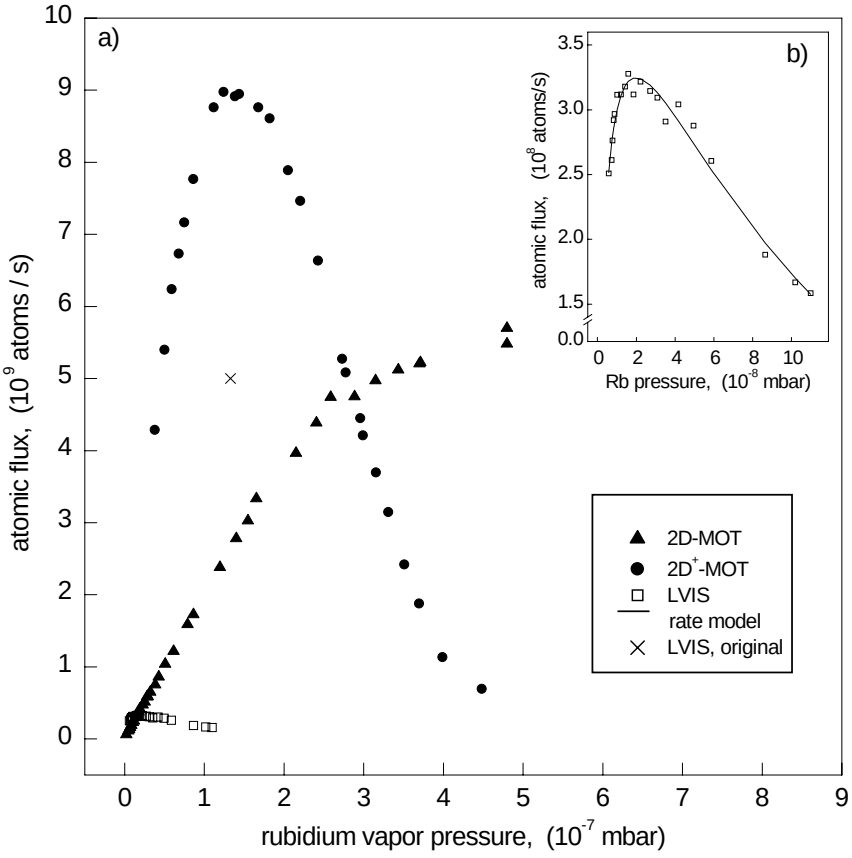

FIGURE 4.3: *Flux of the atomic beam versus rubidium vapor pressure: a) Comparison between the three experimental configurations. At low vapor pressure the flux increases linearly with the density in the background vapor. The flux of the 2D$^+$MOT configuration generated by means of 34 mW laser power exceeds that of the original LVIS [Lu et al., 1996], using 500 mW. b) Comparison of the measured pressure dependence of the LVIS flux with a simple rate model described by Equation (4.2).*

laser power and optimized vapor pressure, the flux from the 2D$^+$-MOT surpasses the one from the LVIS.

In the 2D-MOT collisions play only a minor role. The deviation from linearity is small, and the flux steadily increases even at the saturated vapor pressure. This marked difference is probably due to the absence of a pushing laser beam for the extraction of the atoms. The atoms that leave the 2D-MOT do no longer interact with the laser beam. In the 2D$^+$-MOT and LVIS, on the other hand, the extracted atoms are in the light field of the extraction laser beam. It is well known that collisions in the presence of

near-resonant light can have a very large cross-section [Julienne and Vigué, 1991], due to the strong resonant dipole-dipole interaction, described by a C_3/R^3 potential. Another reason why the 2D-MOT should be less affected by collisions is that the atoms spend a shorter time in the light field because their longitudinal velocity is left unchanged.

In order to include the effect of collisional loss in the extracted beam of the LVIS, we extend the simple rate model for the atomic flux Φ given in [Lu et al., 1996]:

$$\Phi = \frac{R}{1 + \Gamma_{\rm trap}/\Gamma_{\rm out}} \exp(-\Gamma_{\rm beam} t_{\rm out}) \quad . \tag{4.2}$$

In this equation R is the rate at which the trap captures atoms out of the background vapor, $\Gamma_{\rm trap}$ is the loss rate out of the trap due to background collisions, and $\Gamma_{\rm out}$ is the constant outcoupling rate of atoms from the cloud into the beam. Both R and $\Gamma_{\rm trap}$ are proportional to the background rubidium density $n_{\rm Rb}$. The extension here is the inclusion of an exponential loss factor $\exp(-\Gamma_{\rm beam} t_{\rm out})$. It represents the decay of the flux due to background collisions as the atoms travel towards the exit hole with rate $\Gamma_{\rm beam} \propto n_{\rm Rb}$, during a time $t_{\rm out} \approx 1$ ms. By fitting Equation (4.2) to our LVIS data, as shown in Figure 4.3, b), we determine the effective collision cross section for loss out of the beam, $\sigma_{\rm eff} = \Gamma_{\rm beam}/n_{\rm Rb}\bar{v} = 2.3 \times 10^{-12}{\rm cm}^2$, with $\bar{v}$= 270 m/s the average thermal velocity of the background Rb.

This value agrees well with a calculation assuming that atoms in the beam interact with background Rb atoms through a C_3/R^3 potential (resonant dipole-dipole interaction). Adapting the approach described in [Steane et al., 1992] for loss out of a beam rather than a 3D trap, we find

$$\sigma_{\rm eff} = 6.52 \left(\frac{C_3}{m v_{\rm esc} \bar{v}} \right)^{2/3} \approx 3 \times 10^{-12}{\rm cm}^2 \quad . \tag{4.3}$$

Here m is the mass of a ^{87}Rb atom and the escape velocity $v_{\rm esc} \approx 0.4$ m/s is the estimated transverse velocity kick needed to make an atom miss the exit hole.

4.7 Model for the 2D-MOT

The velocity distribution of the flux as well as the total flux of the 2D-MOT can be understood from a simple model of the transverse cooling process. The model uses a number of simplifications. The atomic transition is approximated by taking a $J = 0$ ground state and $J' = 1$ excited state with Landé g-factor $g = 1$. For the light force we take simply the sum of two spontaneous scattering forces from a counterpropagating beam pair, accounting for Zeeman and Doppler shifts. It has been argued by Lindquist *et al.* [Lindquist et al., 1992] that saturation effects in an inhomogeneous magnetic field can be neglected, because one beam of each counterpropagating pair is always closer to resonance.

The resulting force depends only on the combination $x + v_x\tau$ of horizontal position x and velocity v_x, where $\tau = 0.5$ ms is a characteristic time constant. This force is linearized around $x + v_x\tau = 0$ and truncated: $F(x + v_x\tau) = 0$ if $|x + v_x\tau| > x_c = 8$ mm. The resulting damped harmonic oscillator is underdamped for our experimental conditions,

with oscillation frequency $\omega/2\pi = 310$ Hz and damping rate $\gamma/2\pi = 266$ Hz. The spatial profile of the laser beams is ignored, assuming a uniform intensity inside the beams and zero outside.

Atoms enter the cooling region according to a Maxwell-Boltzmann distribution. They enter the cooling region either transversely or longitudinally ("funneling"). We take the axial velocity v_z as a conserved quantity. The transverse motion of an atom that enters the light field at position z is cooled during a transit time $(l-z)/v_z$, with l the position where the light field ends. After the atom leaves the light field at $z = l$ with transverse position and velocity (x, v_x), it may traverse to the exit hole, at $z = l + h$, during a time h/v_z. The atom can exit through the hole if $|x + v_x h/v_z| < R_h$, where R_h is the radius of the hole.

The velocity distribution resulting from this model is shown in Figure 4.2, a). Based on the model we find that the velocity distribution of the 2D-MOT flux is determined by three main processes. First, the main share of slow atoms, with velocity lower than about 20 m/s, result from transverse capture. Atoms enter the light field in a direction transverse to the axis, their transverse motion is damped and they leave along the axis. Atoms that are faster than about 20 m/s spend insufficient time in the light field for the transverse cooling to be effective. The value of 20 m/s, thus depends on the spatial extent of the laser fields along the axis of the transverse laser beams. Second, the tail of relatively fast atoms, $\gtrsim 20$ m/s is due to "funneling", i.e. atoms that enter the light field in the longitudinal direction, through the end cap of the cylindrical cooling region. Third, the absence of atoms at very low velocity is due to the finite transverse temperature reached by the 2D cooling field. The distance between the light field and the exit hole is about 20 mm. As the atoms traverse this distance, their finite transverse velocity leads them astray from the axis. As the corresponding beam divergence is comparatively high for slow atoms in longitudinal direction, slow atoms are filtered from the beam by the exit aperture.

The model predicts that collisional loss is essentially unimportant in the 2D-MOT as long as the rubidium pressure in the vapor cell is below about 2×10^{-7} mbar. Below this value, the total flux grows linearly with the rubidium pressure. If the pressure is further increased collisions cause the total flux to grow slower than linear. The model predicts that at even higher vapor pressure the flux will eventually decrease.

Considering the considerable simplifications made in the model, the agreement with the 2D-MOT data is quite reasonable, both for the velocity distribution and the total flux. A similar vapor-cell based source has recently been proposed by Vredenbregt *et al.* [Vredenbregt et al., 1998]. Their proposal predicts a velocity distribution that peaks at much higher velocities than we observe. The transverse capture of atoms was ignored and only funneled atoms were taken into account. In contrast, our model shows that most of the flux in our experiment is a result of transverse capture, with only the high velocity tail arising from funneling. The reduced presence of atoms with high velocities is essentially due to the fact that the time available for transverse cooling falls off as l/v_z.

4.8 Conclusion

The two-dimensional trapping geometry is very useful to produce slow atomic beams with low divergence out of a vapor cell. The continuous and transient character of the capture process reduces collisional loss from the background, so that high atomic flux can be achieved by increasing the background vapor pressure. Especially the $2D^+$-MOT employing additional cooling in the longitudinal direction yields a very high flux of almost 10^{10} atoms/s at 8 m/s and a narrow width of the velocity distribution of 3.3 m/s (FWHM). This was realized by means of comparatively low laser power. This source can be used for loading a magneto-optical trap, and thus provides an attractive alternative to loading from a Zeeman-slower or current double-MOT systems. It may also find promising application in atom interferometry, atom optics and atomic clocks based on fountains.

Chapter 5

Magneto-optical trap with high atom number

This chapter describes how the atomic beam source, which has been introduced in the previous chapter, is used to load the ultra-high vacuum magneto-optical trap (MOT). This is done with the goal to take benefit of the high beam flux and to achieve a high atom number after a short loading time. The measured atomic beam flux is compared to the measurements of the trap loading. It is demonstrated that the effective loading flux can be improved by avoiding loss from the atomic beam due to fluorescence light originating from the magneto-optically trapped cloud. After loading polarization gradient cooling is used to cool the cloud to a temperature below the Doppler limit, which is $144\,\mu$K for rubidium. Further, it is described how the temperature of the atomic cloud after sub-doppler cooling was minimized for the case of a large atom number.

5.1 Experimental setup

In Figure 5.1 the experimental setup is shown, which is build around the two glass cells of the vacuum system as described in Section 3.2. The lower half shows the magnetic field coils and the laser beams for the atomic beam source, which is described in Chapter 4. In the upper half the setup with the magnetic trap (compare Figure 2.3) and the laser beams for the MOT are depicted. Furthermore, the laser beam used for absorption imaging of the cloud and the CCD screen are indicated.

For the realization of the MOT the two pinch coils of the magnetic trap are used with the currents flowing in opposite directions. These coils generate a gradient per unit current of $0.73\,\mathrm{G\,cm^{-1}A^{-1}}$ for the spherical quadrupole field along the z-direction. A gradient of 29 G/cm is used during the loading phase of the MOT. Six independent laser beams, which are red detuned by 30 MHz with respect to the trapping transition, create the light fields of the MOT. The $1/e^2$-radius of the laser beams is 8.1 mm, so that a large capture region is covered. This is necessary as the Gaussian half width of the atomic

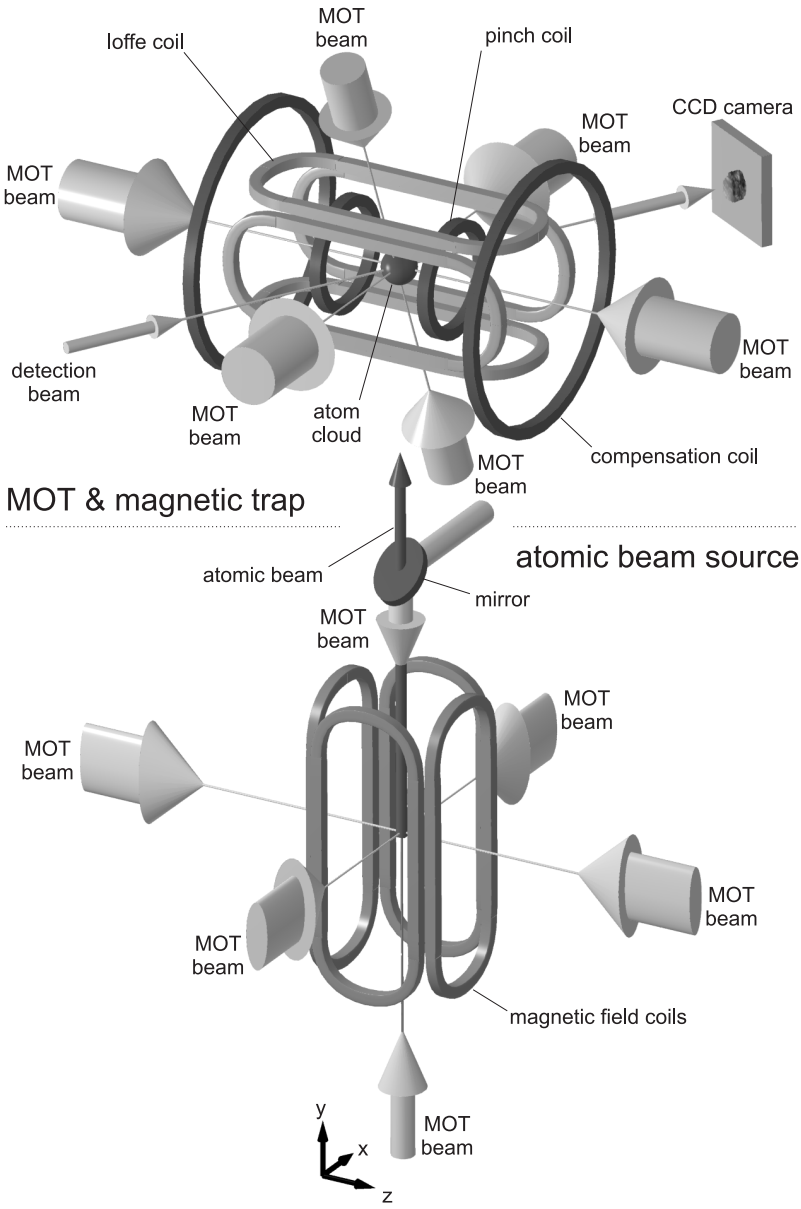

FIGURE 5.1: *Setup used for laser cooling and magnetic trapping: In the lower part the atomic beam source is shown. The atoms are recaptured from the atomic beam into a magneto-optical trap made of six laser beams and two pinch coils. The atomic cloud is at the same location loaded into the magnetic trap, which is made of the Ioffe, pinch, and compensation coils.*

loading beam at the recapture region is 9.1 mm, as extrapolated from the measurement of the beam width in the detection chamber presented in Section 4.5. With an optical power of 13.5 mW per beam the trapping transition is well saturated. The laser power is provided by a broad-area laser system (compare Section 3.1), which delivers up to 130 mW of spatially filtered light. Retroreflected beams would require only half of the laser power. However, this solution is not desirable in case of a large atom number in the cloud, as absorption of the light by the cloud leads to an imbalance of the spontaneous light force. The six laser beams are configured such that two counter-propagating pairs travel horizontally in x- and z-direction perpendicular to the surfaces of the vacuum glass cell.

To minimize the overlap with the atomic beam and avoid undesirable photon scattering of the atoms in the beam, the third pair of laser beams is configured with a small angle from the vertical axis (see Figure 3.2). The overlap with the atomic beam is further reduced by focusing this third pair and reflecting the beams off a small mirror, which is installed close to the atomic beam, towards a vacuum viewport. This configuration of the six MOT beams has the advantage, that the MOT beams do not have to be sent under 45° through the quartz cell. This avoids unwanted reflections at the inner surfaces of the quartz cell. (An anti-reflection coating of the inner surfaces of the quartz cell is technically not possible.) Moreover, in this configuration the magnetic field coils can be brought as close as possible to the quartz cell, and so the strongest possible magnetic confinement can be achieved.

5.2 Loading of the MOT

The MOT is loaded by the atomic beam source in $2D^+$-configuration (compare Chapter 4), which shows a narrow maximum of the atomic flux as a function of the background vapor pressure (compare Figure 4.3). In order to guarantee a reproducible atom number loaded into the MOT the vapor pressure in the source has to be kept stable. This is conveniently done by working with saturated vapor. At a room temperature of 24 °C the vapor pressure is about 3×10^{-7} mbar. At this pressure we achieve 30 % of the maximal flux leaving some room for further improvement. it is further noted here that after these measurements were carried, out new types of laser diodes became available (Sanyo DL-7410-001) providing 66 % more laser power yielding 53 % more atomic flux.

The atom number loaded into the MOT is measured as a function of the loading time by means of absorption imaging, as described in Section 3.5. The images were taken after sub-Doppler cooling, which is described in the next section, and after a period of free ballistic expansion. From the images the central profile along the vertical and horizontal directions were extracted. By a best fit of the profiles to a Gaussian shape (see Section 2.3.2) the dimensions and the maximum absorption of the cloud were determined. With the assumption that the size of the cloud along the direction of observation of the imaging laser beam equals the vertical size the number of atoms (compare Equations (2.32) and (2.33)) was deduced (In these two directions the gradient of the quadrupole magnetic field is equal.).

The measured loading curve is shown in Figure 5.2 (squares). The loading is compared with an exponential growth expression, $N(t) = N_{\mathrm{sat}}(1 - \mathrm{e}^{-t/\tau_{\mathrm{load}}})$, for the atom number,

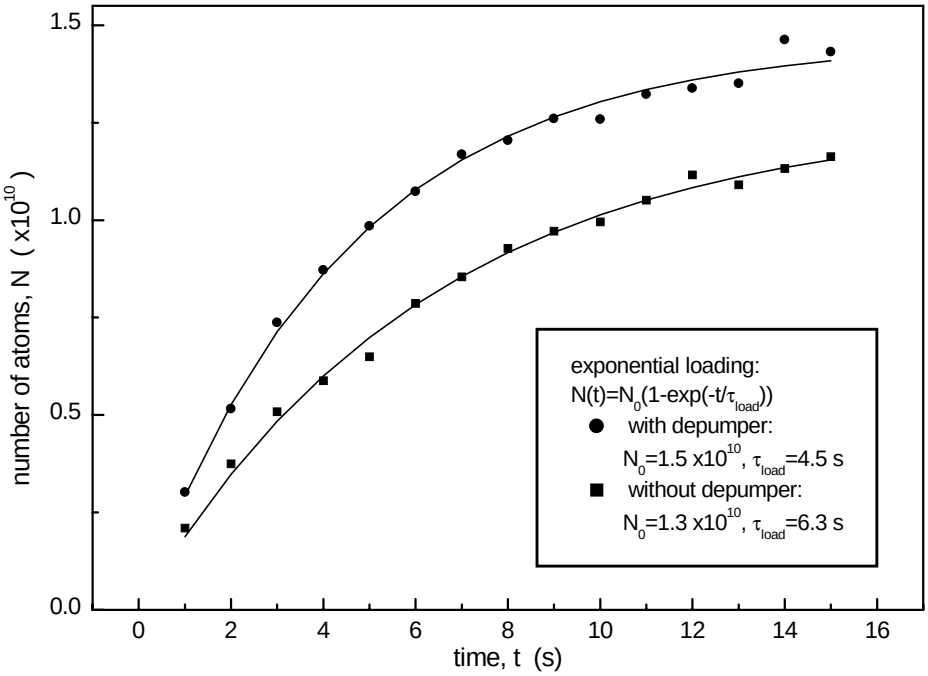

FIGURE 5.2: *Loading curve of the MOT: After* 10 *s typically* 10^{10} *atoms are loaded (squares). The transfer efficiency from the loading beam is about* 70 %. *It can be slightly enhanced (circles) by optically pumping the atoms in a state, which is dark for the trapping light ('depumping').*

where N_{sat} is the number of atoms in case of saturation and τ_{load} is the time constant of the loading process. This describes in good approximation the loading process even in the case of high atom number, where the atom loss from the trap due to intra-trap collisions is dominating the loss due to collisions with particles from the residual gases in the vacuum chamber [Anderson et al., 1994]. From a best fit to the loading curve $N_{\mathrm{sat}} = 1.3 \times 10^{10}$ and $\tau_{\mathrm{load}} = 6.3\,\mathrm{s}$ are obtained. The effective loading flux at short times is 2.1×10^9 atoms/s, whereas the measured atomic beam flux is measured to be 3×10^9 atoms/s. The transfer efficiency is thus about 70 %.

The loss of atoms from the loading beam can be explained by two mechanisms. First, as the loading beam is overlapping with the vertical MOT beams, atoms can be driven transversely out of the loading beam by photon recoil from scattered photons. Second, the fluorescence light emitted by the large MOT in the direction of the atomic beam leads to a net light force repelling the atomic beam from the recapture region of the MOT.

One possibility to further improve the effective loading flux is to optically excite the atoms of the atomic beam by an additional laser beam, before the atoms enter the vertical MOT beams. This so called 'depumping' beam drives the transition $|5S_{\frac{1}{2}}, F =$

$2\rangle \rightarrow |5P_{\frac{3}{2}}, F = 2\rangle$. From the exited state the atoms can decay to the state $|5S_{\frac{1}{2}}, F = 1\rangle$. From this state they are not excited by the trapping light anymore, until they are pumped back by repumping light, when they enter the recapture region. Therefore, the repumping light has to be overlapped with only the horizontal MOT beams and not with the vertical ones. The effect of using the depumping beam is demonstrated in Figure 5.2 (circles). The initial loading flux, the number of atoms in saturation and the loading time constant are slightly enhanced. However, also light resonant to the repumping transition is scattered from the MOT cloud towards the atomic beam. Therefore, the application of the depumping beam could be further improved by enlarging the overlap of the depumping beam with the atomic beam as it approaches the recapture region.

Another possibility to improve the loading flux is by using unbalanced beam intensities in the vertical pair of MOT beams, in order to partially compensate the MOT fluorescence.

For simplicity of the experiment the MOT is loaded without the use of the depumping light. In daily operation it takes 10 s to load the MOT with 10^{10} atoms. Due to imperfections in the alignment of the laser beams, the atomic cloud is not spherical as one would expect in the density-limited regime. The dimensions (radius at a 1/e-fraction of the peak density) of the cloud measured immediately after sub-Doppler cooling are $r_{0,\,y} = 3.1\,\mathrm{mm}$ and $r_{0,\,z} = 3.5\,\mathrm{mm}$.

A very similar result can be obtained by using a coil configuration that differs from the anti-Helmholtz configuration used in a standard three-dimensional MOT. As the central density in the MOT is limited by radiation trapping, the volume of the cloud has to be increased in order to trap a higher atom number. This can be realized by applying a strong magnetic field gradient produced by the Ioffe coils of the magnetic trap and a weak gradient produced by the pinch coils. This gives rise to a large trapped cloud elongated along the axis of the Ioffe-coils. It was found out, that it is possible to trap atom numbers comparable to the ones described above. This configuration is not used in the experiments, as at lower densities the transfer to the magnetic trap (Section 6.1) was found to be less efficient.

5.3 Loading of the MOT from vacuum background

In contrast to other experiments working with loading of the MOT in the UHV cell by a vapor cell based atomic source, in this experiment comparatively high vapor pressure used in the vapor cell. Therefore, it is necessary to experimentally investigate, whether the differential pumping, as described in Section 3.2, guarantees a sufficiently good vacuum in the UHV cell. For this purpose, the MOT was loaded without the use of the atomic beam. In absence of the loading beam residual loading of the MOT from background rubidium gas in the UHV cell can be observed [Anderson et al., 1994]. In this experiment an initial capture rate of $R = 2.6 \times 10^5\,\mathrm{s}^{-1}$ and an atom number of 1.6×10^6 after saturation were found. From the capture rate R the room temperature rubidium partial pressure P_{Rb} in the UHV cell can be estimated by [Gibble et al., 1992]

$$P_{\mathrm{Rb}} = \frac{R\,k_{\mathrm{B}}T}{\pi^2\,r_c^2\,v_c^4}\left(\frac{2\pi k_{\mathrm{B}}T}{m}\right)^{3/2} \quad , \tag{5.1}$$

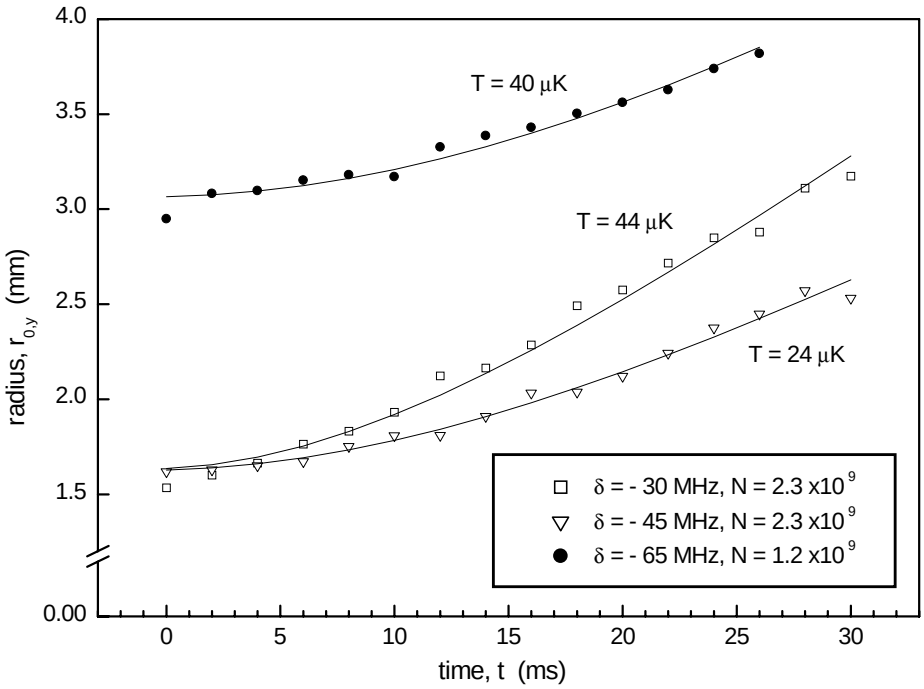

FIGURE 5.3: *Temperature measurement of the atomic cloud: With* 1.2×10^{10} *atoms a temperature of typically* $40\,\mu K$ *is achieved after* $15\,ms$ *polarization gradient cooling with a laser detuning of* $-65\,MHz$ *and peak intensity of* $9.5\,mW/cm^2$.

with the capture range $r_c = 11\,\mathrm{mm}$ and the capture velocity $v_c = (r_c\, h\Gamma/(2\lambda m))^{1/2} = 35\,\mathrm{m\ s^{-1}}$ for the given MOT parameters. The rubidium partial pressure was estimated to be on the order of $P_{\mathrm{Rb}} \approx 4 \times 10^{-12}\,\mathrm{mbar}$, which is negligible for atom trapping.

Furthermore, it was experimentally verified that the effusive beam which leaves the vapor cell through the differential pumping hole and points to the trapping region, does not noticeably contribute to the loading rate of the MOT. This follows, as the same loading rate was obtained while applying the plug beam, as described in Section 4.4, which removes atoms with velocities smaller than the capture velocity of the MOT from the effusive beam.

5.4 Temperature of the cold cloud after optical cooling

After loading, the trapped cloud is cooled by the method of polarization gradient cooling in $\sigma^+ - \sigma^-$ configuration [Dalibard and Cohen-Tannoudji, 1998]. The temperature of the cloud is deduced from a time-of-flight spectrum after free ballistic expansion of the cloud.

The density distribution of the expanded cloud is given by the convolution of the spatial distribution before the expansion, which is approximately Gaussian, with the Maxwell-Boltzmann velocity distribution of the atoms in the cloud. For collisionless expansion over a time τ_{exp} the 1/e-radius of the cloud is

$$r_{0,i}(\tau_{\mathrm{exp}}) = \sqrt{r_{0,i}^2(0) + \tau_{\mathrm{exp}}^2 2k_{\mathrm{B}}T/m} \quad . \tag{5.2}$$

In Figure 5.3 time-of-flight measurements for different experimental conditions are compared. In all measurements a cooling time of 15 ms has been used. From a best fit of Equation (5.2) to the data the temperature of the cloud was determined. The temperature was found to depend on the atom number. At high atom number, 1.2×10^{10} , polarization-gradient cooling typically results in a temperature of 40 μK (circles). This is significantly above the low temperatures of less than 10 μK which can be achieved with atom numbers below 10^7. The increase in the observed temperature is attributed to due a disturbance of the polarization gradient by fluorescence light, which is reabsorbed in the cloud [Cooper et al., 1994].

The temperature after polarization gradient cooling is within certain limits proportional to the dynamical Stark-shift parameter I/δ, e.g. the ratio of laser intensity I and detuning δ. This behaviour is demonstrated in Figure 5.3 by varying the detuning for a fixed small atom number (triangles and squares). To minimize the temperature at high atom number the maximal available detuning of -65 MHz was used. This detuning is limited by the band edge of the acousto-optic modulator used for control of the laser detuning. By reducing the laser intensity a small decrease of the temperature was observed, but also a significant drop in the number of atoms. Under typical conditions only 10 % of the atoms are lost. This was realized by applying a peak intensity of 9.5 mW/cm^2 for each of the MOT beams.

Chapter 6

Magnetic Trapping

After collecting the atoms in the MOT and polarization-gradient cooling the following experimental step towards BEC is magnetic trapping of the atoms. In order to magnetically trap the gas it has to be spin polarized. Therefore, the atoms are optically pumped into the state $|5S_{\frac{1}{2}}, F = 2, m_F = 2\rangle$. The trapping is realized by switching on a shallow magnetic potential preserving the size of the cloud ('size matching'). This transfer is followed by adiabatic compression of the cloud, which is done by slowly increasing the currents through the magnetic field coils. Aside from the procedural steps of loading the trap, in this chapter also the performance of the trap is described. Measurement of the lifetime of the sample in the compressed magnetic trap gives information on whether efficient evaporative cooling is possible and BEC can be achieved. Measurement of the harmonic trap frequencies is essential for subsequent quantitative analysis of the trapped Bose-gas in the degenerate regime.

6.1 Magnetic trap loading

After polarization-gradient cooling the gas is not spin polarized. Only a fraction of the atoms would be trapped when switching on the magnetic trap at this stage. In order to spin polarize the atoms, they are optically pumped into the state $|5S_{\frac{1}{2}}, F = 2, m_F = 2\rangle$ with respect to the symmetry axis of the trap (z-direction). During optical pumping the quantization axis is defined by applying a magnetic guiding field of 220 mG along the z-direction. For this purpose the Earth-field compensation coils are used. For the optical pumping two overlapping laser beams are applied also along the symmetry axis of the trap. One beam is tuned resonant with the optical pumping transition (compare Section 2.1.1), the other with the repuming transition. Both laser beams have σ^+-circular polarization with respect to the axis of quantization. The atoms are exited to the $|5P_{\frac{3}{2}}, F = 2\rangle$ state by $\Delta m_F = +1$ transitions. From this state they decay spontaneously into both hyperfine ground states, from where they are reexcited by the lasers. After a few cycles, the atoms are pumped into the $|5S_{\frac{1}{2}}, F = 2, m_F = 2\rangle$ state. They stay in this state, as they do not interact with the light fields anymore. In this way it is possible to

optically pump all parts of the gas cloud, although it is originally optically dense for the resonant light fields.

The efficiency of the optical pumping process is limited by reabsorption of unpolarized fluorescence light. This light pumps the atoms out of the dark state to undesired Zeeman states. For a long optical pumping time the efficiency will not be further increased, but the cloud will be heated due to continuous scattering of light.

In order to estimate the time needed for optical pumping the absorption cross-section averaged over the optical pumping and repumping transitions is calculated to be $\sigma_{\mathrm{abs}} = (3\lambda^2/8\pi) \approx 7 \times 10^{-10}\,\mathrm{cm}^2$. Assuming a density of the cloud of about $n = 10^{10}\,\mathrm{cm}^{-3}$, the penetration depth is on the order of $(n\sigma_{\mathrm{abs}})^{-1} = 140\,\mu\mathrm{m}$. Thus, the time needed for optical pumping of the cloud of 1 cm size is about 70 times longer, than the optical pumping time for a single atom. If one roughly assumes, that on the average a single atom has to scatter 20 photons before ending up in the $|F = 2, m_F = 2\rangle$ state, the optical pumping time for a single atom is in case of saturation $2\,\mu$s. This results in an optical pumping time for the entire cloud of approximately $140\,\mu$s. In the experiment the optimum optical pumping time was found to be $200\,\mu$s. In order to produce this short light pulse the optical pumping beam is switched by means of an AOM. The repumping laser is switched by a mechanical shutter. It is switched off a few milliseconds later than the trapping laser. This prevents the atoms from ending up in the $|5S_{\frac{1}{2}}, F = 1\rangle$ state. Atoms, which remain in the $|5S_{\frac{1}{2}}, F = 2, m_F = 1\rangle$ state due to inefficient optical pumping, are not trapped in the magnetic potential. These atoms fall out of the magnetic trap within the first 150 ms of magnetic trapping, as the gradient in the magnetic potential is not strong enough to support them against the gravitational force. The achieved efficiency of the optical pumping is about 40 %, as 4×10^9 atoms are trapped in the magnetic trap, starting with 10^{10} atoms in the MOT.

After optical pumping the magnetic trap is switched on for recapture of the atoms. The current through the pinch coils rises within 1.5 ms to its set value, followed by a 20 % overshoot. The total settling time is 10 ms. The current in the Ioffe coils is switched on within 2.5 ms with a 25 % overshoot and a settling time of 15 ms. As the current in the pinch coils rises faster than the current through the Ioffe coils, the axis of quantization is preserved during the initial rise of the currents. When the full current is reached the minimum value of the magnetic field inside the trap is 37 G. As the quadrupole field catches up with the axial field the magnetic moments of the atoms follow adiabatically the direction of the local magnetic field (compare Section 2.2).

To avoid heating of the gas cloud its size must be conserved in the transfer process. For $B_0 = 37$ G the trap is approximately harmonic over the size of the gas cloud. Therefore, the density distribution has a Gaussian shape (compare Section 2.3.2). For a given temperature the harmonic trap frequency ω_i in the i-direction has to be matched to the 1/e-radius $r_{0,i}$ of the cloud, according to Equation (2.17). For different values of ω_i the cloud would not be in thermal equilibrium and would start to expand or shrink after the transfer. This would lead to an increased temperature after thermalization.

In the experiment, the trap frequencies were adjusted, to minimize the temperature increase during the transfer process. The temperature of the transferred cloud was measured after a thermalization time of 4 s using the time-of-flight method as described in in Section 5.4. As the density distribution in the Ioffe-quadrupole trap is not Gaussian,

the time-of-flight method was applied only in the limit of long expansion times, where the density distribution of the trapped gas is of no importance.

Starting with a 3 mm gas cloud at a temperature of 40 μK the optimum trapping parameters were found to be $B_0 = 37\,\mathrm{G}$, $\alpha = 37\,\mathrm{G/cm}$, and $\beta = 36\,\mathrm{G/cm^2}$. This corresponds to a roughly isotropic trap of $\omega = 2\pi \cdot 7.5\,\mathrm{Hz}$. From an estimate based on Equation (2.33) one calculates $\omega = 2\pi \cdot 4.6\,\mathrm{Hz}$. A strict agreement is not to be expected, as for $\alpha < \beta\, r_z$ the radial confinement is significantly reduced as can be seen from Equation (2.8). In order to prevent atom loss the quadrupole gradient and with it the radial frequency as calculated by Equation (2.12) is slightly increased. Another reason for using a slightly stronger confinement is the increased temperature of the trapped cloud after the transfer, which is typically 66 μK. The rise in temperature during the transfer is attributed to momentum diffusion due to photon scattering during optical pumping or imperfections of the compensation of the gravitational shift described in the following paragraph.

Due to gravity the minimum of the magnetic trapping potential is not at the same position as the minimum of the magnetic field. For the harmonic potential the shift is

$$\Delta y_{\mathrm{grav}} = \frac{g_{\mathrm{earth}}}{\omega_\rho^2} \approx 4\,\mathrm{mm} \quad , \tag{6.1}$$

where g_{earth} is the gravitational acceleration of the Earth. However, the center of the cloud produced by the MOT is independent of gravity, as magneto-optical trapping is not based on a conservative potential. A motion of the center of mass of the cloud during and after the transfer to the magnetic trap has to be prevented, as it would result in an increased temperature after thermalization. Therefore, the center of the magnetic potential has to coincide with the center of the cloud. This is achieved by shifting the symmetry axis of the Ioffe-quadrupole field in the vertical direction, which can be realized by reducing the current in the upper one of the four Ioffe-coils I_{Ioffe1} relative to the current through the other Ioffe coils $I_{\mathrm{Ioffe2-4}}$ (compare Figure 3.5). For small variations of the currents the shift of the quadrupole axis is proportional to the relative difference of the currents $y_0\,(I_{\mathrm{Ioffe2-4}} - I_{\mathrm{Ioffe1}})/I_{\mathrm{Ioffe2-4}}$ with the constant $y_0 = 7.7\,\mathrm{mm}$. For compensation of the gravitational shift a current of 25 A is used in the Ioffe bypass (branch D).

6.2 Adiabatic compression

Crucial for efficient evaporative cooling is a high elastic collisional rate allowing a short thermalization time of the gas. Therefore, it is essential to adiabatically compress the magnetically trapped gas, until the condition for runaway evaporative cooling is met (compare Section 2.54). To realize the adiabatic compression the currents in the Ioffe- and pinch- and compensation coils are gradually increased to 400 A during a period of 6.615 s. Adjusting the offset magnetic field to $B_0 = 0.85\,\mathrm{G}$ by means of the bypass resistor results in trap frequencies of $\omega_z = 2\pi \cdot 21.6\,\mathrm{Hz}$ and $\omega_\rho = 2\pi \cdot 486.6\,\mathrm{Hz}$ as follows from Equations (2.11) and (2.12) and the trap parameters given in Table 3.2. These values are in good agreement with the measured trap frequencies presented in Section 6.4. After the adiabatic compression the temperature of the cloud is approximately 760 μK. During the adiabatic compression no significant atom loss was observed. At this temperature and

with the measured atom number of 4×10^9 , the peak density of the cloud is calculated to be $7 \times 10^{11}\,\mathrm{cm}^{-3}$. The elastic collisional rate as defined in Equation (2.58) was increased from approximately $\tau_{\mathrm{el}}^{-1} \equiv n(0)\,\sigma\,v_T = 3\,\mathrm{s}^{-1}$ before the compression, to $\tau_{\mathrm{el}}^{-1} = 275\,\mathrm{s}^{-1}$ after compression, with the thermal velocity $v_T = \sqrt{8 k_{\mathrm{B}} T/\pi\, m}$. Note that the thermalization rates are slightly smaller, as for the calculation of the elastic collision rate only the peak density is considered. The degeneracy parameter of the gas is $n(0)\Lambda_T^3 = 2 \times 10^{-7}$, many orders of magnitude away from quantum degeneracy (compare Equation 2.19).

During adiabatic compression the currents in the magnetic field coils were changed in four successive steps. The order of these steps depends on the technical possibilities provided by the electronic control of the trap currents, which is shown in Figure 3.5. In the following the steps are briefly described. Table 6.1 summarizes the the values of the magnetic trap parameters and the cloud temperature after each of the steps.

0. Start: The magnetic trap is switched on with a shallow confinement in order to recapture the optically pumped cloud (path A closed, path B open, compare Figure 3.5). The gravitational shift is compensated by reduction of the current in the upper Ioffe-coil (path D & E used).

1. Step: The cloud is radially compressed, by increasing the current through the compensation coils (opening path A) and decreasing B_0. At the same time the compensation of the gravitational shift of the position of the cloud in the magnetic potential is gradually switched off (closing path D). For this purpose, the current bypassed from the upper Ioffe coil is reduced to zero.

2. Step: For compression in the direction along the symmetry axis of the trap the current through the pinch coils is increased to 400 A (power supply A). Although at the same time the current through the compensation coils increases (path A), the central magnetic field B_0 does not remain constant, but increases. In order to keep the radial trap frequency constant during this step the current in the Ioffe coils is also increased (power supplies B & C). After this step the trapping potential is almost spherical.

3. Step: To increase the linear gradient of the quadrupole field the current in the Ioffe coils is increased to 400 A (power supplies B & C).

4. Step: In the last step full radial compression is achieved by lowering B_0. Almost the full current through the pinch coils runs also through the compensation coils (by closing path B). The exact value of B_0 is adjustable by the current running through the resistor bypassing the compensation coils. If no current runs through the bypass resistor, the central magnetic field is $B_0 = -2.8\,\mathrm{G}$ and negative with respect to the positive z-axis. Typically 4.3 A has to run through the bypass to adjust B_0 to a value of about 0.85 G.

In Table 6.1 the duration for the different steps is listed. The change of the trap parameters during the individual steps is realized by using continuous, arbitrary waveforms of the computer control. Duration Δt and update interval $\Delta\tau_{\mathrm{wf}}$ of the waveforms are listed in Table 6.1. The duration and form of the waveforms were designed to fulfill the

property	unit	0. Step	1. Step	2. Step	3. Step	4.Step
T	(μK)	66	154	275	573	758
T_{theory}	(μK)	-	98	285	450	748
ω_z	(Hz)	7	7	21.4	21.4	21.6
ω_ρ	(Hz)	8	19	19	50	486.6
B_0	(G)	37	8	75	75	0.85
Δt	(s)	-	2.815	1.5	0.3	2
$\Delta\tau_{\text{wf}}$	(ms)	-	10	30	15	10
I_{pathE}	(A)	50	50	191	400	400
I_{pathA}	(A)	0	33	310	310	400
I_{pathB}	(A)	42	9	90	90	0
I_{pathD}	(A)	25	0	0	0	0

TABLE 6.1: *Adiabatic compression takes place in four successive steps. The table summarizes the changes of the trapping parameters during the compression. The measured temperature increase after each compression step is compared to the value which is calculated by assuming adiabatic compression. The excess temperature increase after the first step is probably due to the deviation of the trapping potential from a power-law potential, which is used in the calculation.*

adiabaticity condition as discussed in Section 2.3.3. It was experimentally verified for each step, that with a slower compression rate no lower temperatures are achieved.

The measured temperatures after each step are compared with the temperatures calculated using Equation 2.39, which includes the temperature measured after the previous step and the change of the trap parameters during the step. The significant increase in temperature after the first step is probably due to imperfect matching of the trap shape to the size of the gas cloud after optical pumping. Moreover, the optical pumping process gives rise to a slight center-of-mass motion due to photon recoil, and results in a temperature increase. The excess temperature observed after the third step remains unexplained.

6.3 Life time of the magnetic trap

Next to a high elastic collisional rate, another important requirement for efficient evaporative cooling is a long life time of the magnetically trapped gas sample (see Section 2.54). After adiabatic compression, where the density of the cloud is about $7 \times 10^{11}\,\text{cm}^{-3}$, trap loss due to inelastic three body-recombination can be neglected [Söding et al., 1999]. Loss due to two-body spin relaxation has been theoretically predicted to be negligible even at high densities [Julienne et al., 1997], and has not been experimentally observed, yet. At the density of the compressed cloud the dominant loss of atoms from the magnetic trap is due to collisions with particles from the room temperature vacuum background.

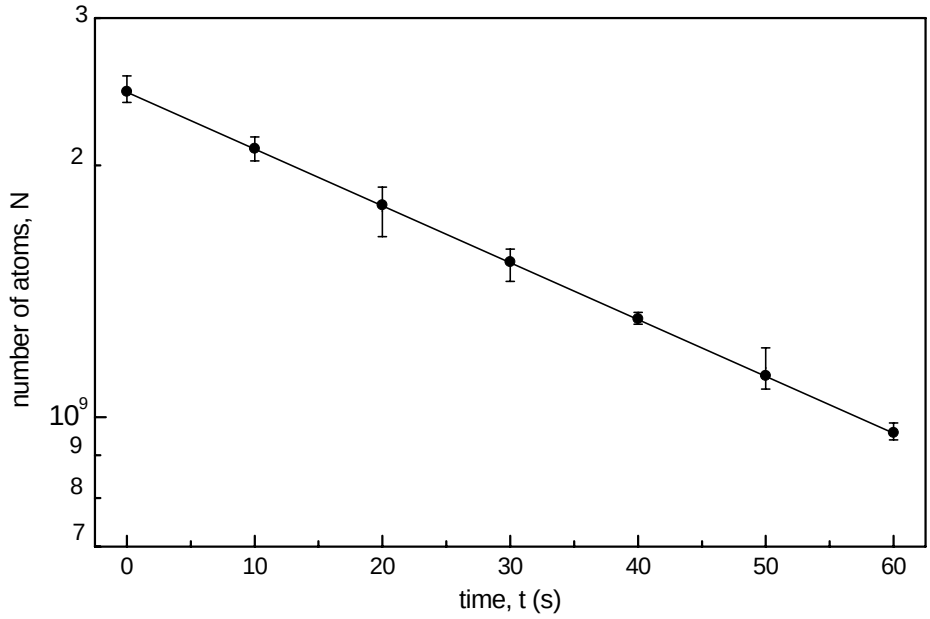

FIGURE 6.1: *Decay of the number of atoms due to background collisions. A fit to an exponential decay results in a life time of* 64 *s.*

The total loss rate $\dot{N}$ due to the background collisions is independent of the density and proportional to the number of atoms in the trap. Thus, the number of trapped atoms decays exponentially as $N(t) = N(0)\,\mathrm{e}^{-t/\tau_{\mathrm{bg}}}$, where τ_{bg} is the trap life time. The life time was measured by repeatedly performing loading and adiabatic compression of the trap as described above, and measuring the atom number after a variable trapping time. The atom number was measured by absorption imaging after release of the cloud from the trap as described in Section 5.2. The decay curve of the cloud is shown in Figure 6.1. Fitting the data to an exponential decay results in a magnetic trap life time of $\tau_{\mathrm{bg}} = 64\,\mathrm{s}$.

It was found that the magnetic trap life time depends on the value of the magnetic field B_0 in the trap center. This field is measured by repetitively applying an rf-evaporative cooling ramp (as will be described in Section 7.1), and lowering the final frequency, until all atoms are removed from the trap. The central magnetic field can then be calculated from the final frequency with the help of Equation (2.61). Increasing B_0 to a value of 2 G by changing the current in the compensation coils leads to an increase of the observed life time to 85 s. Further increase of B_0 does not increase the life time significantly. In the opposite case, at $B_0 = -1.4\,\mathrm{G}$, the life time is reduced to 45 s. The decrease in the life time is attributed to non-adiabatic spin transitions in the low magnetic field near the trap center (see Section 2.2).

6.4 Measurement of the harmonic trap frequencies

In the following the measurement of the harmonic frequencies of the magnetic trap is described. The axial and radial oscillations of the cloud are driven by modulating the magnetic potential. The oscillation is observed by imaging the cloud after a variable holding time.

The harmonic approximation of the magnetic trapping potential in the radial direction is only valid for small distances from the trap center. After adiabatic compression the harmonic radius of the trapping potential in radial direction, as defined by Equation (2.10), is $\rho_\mathrm{h} = 32\,\mu$m. This corresponds to a 1/e-radius of the Gaussian density profile of the trapped cloud at a temperature of $T = \rho_\mathrm{h}^2\,\omega_\rho^2\,m/(2k_\mathrm{B}) = 48\,\mu$K. As after adiabatic compression the temperature of the cloud is $760\,\mu$K, the cloud mainly covers the linear part of the trapping potential. For measurement of the trap frequencies in axial and radial direction the cloud was evaporatively cooled (see Chapter 7.1) to temperatures of $1\,\mu$K and $1.6\,\mu$K, respectively.

After evaporative cooling the trap oscillation was driven by sinusoidally displacing the center of the trapping potential by means of the tuning coils. A drive of five periods at a frequency of 20.64 Hz in the axial direction or ten periods at a frequency of 453 Hz in the radial direction was applied. After a variable holding time t the cloud was released from the trap and an absorption image was taken after 10 ms of ballistic expansion. From the absorption images the centroid of the cloud was determined. Figure 6.2 shows the axial and radial oscillations of the cloud centroid.

In order to determine the trap frequencies the measured positions $x_{z,\,\rho}(t)$ along the radial and axial directions of the cloud were fitted to an exponentially damped sinusodial function

$$x_{z,\,\rho}(t) = A\sin(\omega_{z,\,\rho}\,t + \phi)\cdot \mathrm{e}^{-\frac{t}{\tau}} + \text{const.} \quad . \tag{6.2}$$

where A is the amplitude of the oscillation, ϕ is a phase factor, and τ a damping time. An additional constant defines the center of the trap. The resulting values from the fit for the axial and radial trap frequencies are $\omega_z = 2\pi\cdot 20.64$ and $\omega_\rho = 2\pi\cdot 477.4$ Hz respec-

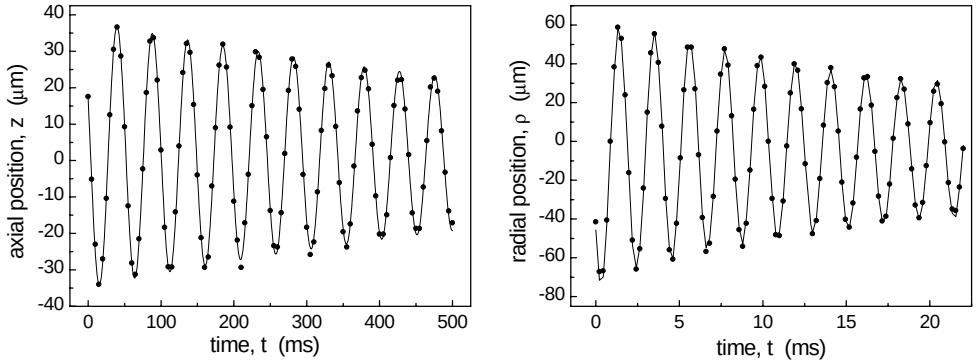

FIGURE 6.2:Harmonic trap oscillation of the cloud centroid. The fits correspond to an axial frequency of $\omega_z = 2\pi\cdot 20.64$ and a radial frequency of $\omega_\rho = 2\pi\cdot 477.4$.

tively. This is within 5 % (axial) and 1.9 % (radial) agreement with the trap frequencies calculated by Equations (2.11) and (2.12) and the magnetic field strengths of the trap as listed in Table 3.2. In order to measure the 0.85 G offset field in the trap center, the method as described in Section 7.2 was applied, which employs evaporative cooling to the bottom of the trap.

The trap oscillations exhibit damping with $\tau = 0.9\,\mathrm{s}$ for the axial and $\tau = 58\,\mathrm{ms}$ for the radial oscillation. This is attributed to dephasing as a result of the anharmonicity in the trapping potential.

Chapter 7

Evaporative cooling and Bose-Einstein condensation

This chapter describes the achievement of BEC in a cold cloud of rubidium atoms by forced evaporative cooling under 'runaway' conditions. The evaporation is forced by ramping down the frequency of an radio frequency magnetic field. The efficiency of the evaporation process with respect to the particle loss is evaluated. At a temperature slightly above 1 μK the BEC phase transition is reached. The formation of the condensate is observed by absorption imaging. A description of the analysis methods used to determine temperature, atom number, and chemical potential from the absorption images is included. It is shown that gas samples were produced which are in the transition region between the collisionless and the hydrodynamic regimes. As the last part of this chapter a demonstration of the so called 'atom laser' was added.

7.1 Evaporative cooling

Evaporative cooling is realized by following the principles as introduced in Section 2.5. Crucial for achieving Bose-Einstein condensation at the highest densities is to realize evaporative cooling in the 'runaway' regime. This is achieved by adiabatic compression of the cloud as described in the previous chapter. After the compression the cloud of 4×10^9 atoms has a temperature of $T = 760\,\mu$K and a central density of $n(0) = 7 \times 10^{11}\,\mathrm{cm}^{-3}$. From this follows an elastic collision rate of $\tau_{\mathrm{el}}^{-1} = 275\,\mathrm{s}^{-1}$. As discussed in Section 6.3, the dominant loss mechanism at this stage is background collisional loss with a measured loss rate of $\tau_{\mathrm{bg}}^{-1} = 1/64\,\mathrm{s}^{-1}$. Thus, the collisional ratio for background collisions is $\lambda_1 = \tau_{\mathrm{el}}/\tau_{\mathrm{bg}} = 5.6 \times 10^{-5}$. Therefore, the condition for runaway evaporative cooling as expressed by Equation (2.58) is fulfilled.

Evaporative cooling was performed by applying a radio-frequency field as described in Section 3.4. The starting frequency was 50 MHz corresponding to a truncation parameter of $\eta = 6.3$. In this way atoms up to an energy of $\epsilon_t = 4.7\,\mathrm{mK}$ were removed from the

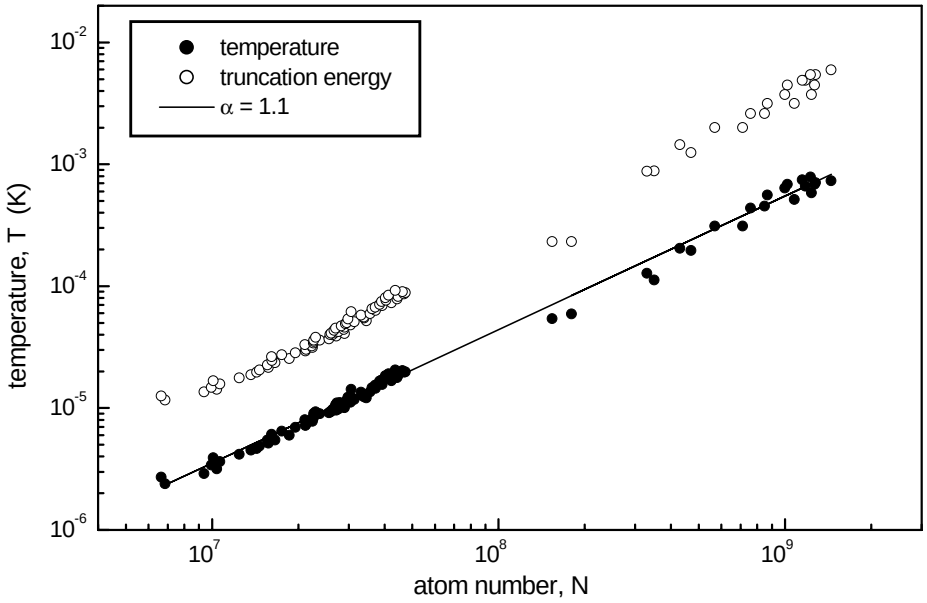

FIGURE 7.1: *Evaporative cooling towards Bose-Einstein condensation: Measured atom number and temperature (solid circles) and truncation energy (open circles) during evaporative cooling. The efficiency parameter* $\alpha_{\rm ev} = 1.1$ *obtained from the fit (solid line) is almost constant over the entire evaporation. Per order of magnitude temperature drop the number of atoms is decreased by evaporation by about one order of magnitude.*

trap. The frequency was then ramped down to values around 600 kHz for an offset field of $B_0 = 0.85$ G. The shape of the frequency ramp was chosen to be linear, as discussed in Section 2.5.1. An evaporation time of 10.6 s was optimal for yielding the highest atom number at the BEC transition temperature. Evaporative cooling in 2.14 s resulted in BEC with about 40% less atoms.

In order to induce adiabatic transitions to untrapped states during the evaporation, the weak dependence of the Landau-Zener parameter (see Equation (2.65)) on the gas temperature has to be considered. For this purpose, the applied magnetic field amplitude was reduced linearly from 110 mG to 40 mG, by changing the rf-power by means of the variable attenuator. These values were experimentally optimized to yield the highest number of atoms remaining at the end of the evaporative cooling ramp. It should be noted here, that for high truncation energies incomplete evaporation occurs due to the presence of the quadratic Zeeman effect (see Section 2.1.2). This effect has important practical consequences as it leads to a trapped cloud of atoms at high energies as will further be discussed in Chapter 8.

After finishing the evaporative cooling ramp, the rf-frequency and amplitude were kept constant for 50 ms. During this period of plain evaporative cooling the cloud was

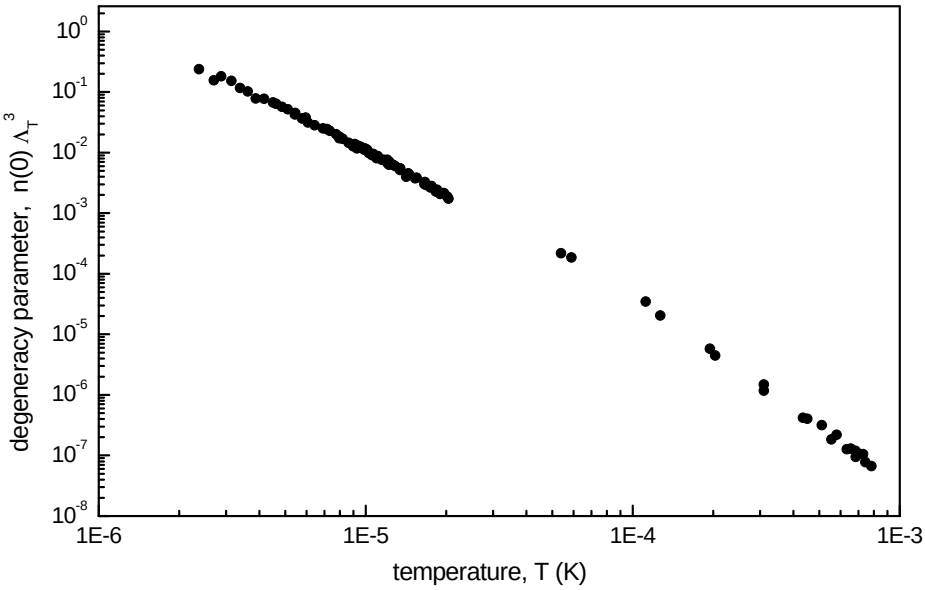

FIGURE 7.2: *The degeneracy parameter during forced evaporative cooling as calculated from the measured temperature and atom number: In this measurement the gas reaches a temperature of about* $2.4\,\mu K$ *with a degeneracy parameter of* $n(0)\Lambda_T^3 = 0.24$*, not yet in the degenerate regime. Further evaporative cooling leads to Bose-Einstein condensation.*

further cooled, and as the truncation energy remained constant, the truncation parameter increased. After this period the rf-power and the magnetic trap were switched off to let the cloud ballistically expand. After 8 ms expansion absorption images of the cloud were taken. Temperature and atom number were obtained from the density profiles of the absorption images as described in Chapter 5. Figure 7.1 (solid circles) shows how temperature and atom number decreased during evaporative cooling. For this measurement the trap was repeatedly loaded and the evaporation ramp was interrupted after various times in order to measure temperature and atom number. As during the evaporation process the expanded cloud was getting dilute and smaller, the detuning of the imaging laser beam and the magnification of the imaging system had to be adjusted to keep the optical density in the proper range.

As described in Section 2.5.1 the temperature depends on the number of atoms as $T \propto N^{\alpha_{\rm ev}}$. From the measurement one can see, that the efficiency parameter $\alpha_{\rm ev}$ remains to good approximation constant during the entire evaporation process. The value $\alpha_{\rm ev} = 1.1$, obtained from a best fit, is a clear indication, that evaporative cooling happens in the 'runaway' regime (compare Equation (2.54)). Figure 7.1 (open circles) shows also the truncation energy calculated from the final frequency of the ramp. At the final stage of evaporative cooling the truncation parameter is reduced to $\eta = 4.4$.

From the measured temperature and atom number and the magnetic trap parameters

α, β and B_0 (Table 6.1) the degeneracy parameter $n(0)\Lambda^3$ can be calculated with the help of the set of Equations (2.28), (2.30), and (2.31). The resulting degeneracy parameter as a function of the atom number is shown in Figure 7.2. In the presented measurements a maximum degeneracy parameter of 0.24 has been reached. In this case, the gas is at the border of the quantum degeneracy regime, where the theoretical description of Section 2.3.2 is still valid. The measurement shows that evaporative cooling is a powerful technique, which increases the degeneracy parameter of the gas by at least seven orders of magnitude within 10 s. By further evaporative cooling the quantum degenerate regime is entered and Bose-Einstein condensation is achieved.

7.2 Observation of Bose-Einstein condensation

As before, information on Bose-Einstein condensation of the cloud is gained from absorption images. Figure 7.3 shows a series of 14 absorption images, where the final truncation energy of the cooling ramp has been varied from 719 kHz ($\epsilon_t = 10.2$ mK) to 612.5 kHz ($\epsilon_t = 0$ mK). After finishing the evaporative cooling ramp the rf-frequency was kept constant for a period of 10 ms before the cloud was released from the trap. The expansion time after release from the trap has been $\tau_{exp} = 6.3$ ms. The sequence shows how the cloud shrinks as it is cooled (Figure 7.3, a)-c)). From Figure 7.3, d) on a very dense part appears in the center. This is the Bose-Einstein condensate, which is surrounded by the more dilute non-condensed, thermal cloud. Further cooling produces large and almost pure condensates (Figure 7.3, i)). The reduction of the truncation energy beyond this point leads to spilling of the condensate. From the value of the rf-frequency at which the cloud disappears completely (Figure 7.3, l)) the offset magnetic field in the center of the magnetic trap can be calculated. Equation (2.61) results in $B_0 = 875$ mG for this particular measurement. In the presence of the $B_{rf} = 40$ mG rf-magnetic field used at the end of evaporative cooling, the energy splitting of the Zeman states in the dressed state picture is +14 kHz at the resonance. Due to this power broadening the atoms are spilled from the trap even if the the rf-frequency is still above the resonance frequency for the trap center. Therefore, offset magnetic field in the trap center is about 40 mG smaller compared to the value calculated by Equation (2.61). The truncation energy is calculated by Equation (2.62) which yields 10.2 μK for the first picture of the series.

The presence of the condensate can be proved by analyzing density profiles obtained from the absorption images. In a first step the absorption function is transformed into a map of the optical density $D(y, z)$ with the help of Equation (3.1). From these optical density images the temperature, the total number of atoms and the number of condensed atoms can be obtained as follows: First, the total number of atoms can be derived by integrating the observed column density $\eta(y, z) = D(y, z)/\sigma_\pi$ over the y-z plane. As the information of the image is given as an array of pixel values, the integration is replaced by a summation over all pixels

$$N = \frac{\Delta_y \Delta_z}{\sigma_\pi} \sum_i \sum_j D(y_i, z_j) \quad , \tag{7.1}$$

where $\Delta_y = \Delta_z = 3.77\,\mu$m is the size of the region in the object plane which is imaged onto a single pixel. For the measurements shown in Figure 7.3, a detuning of the detection

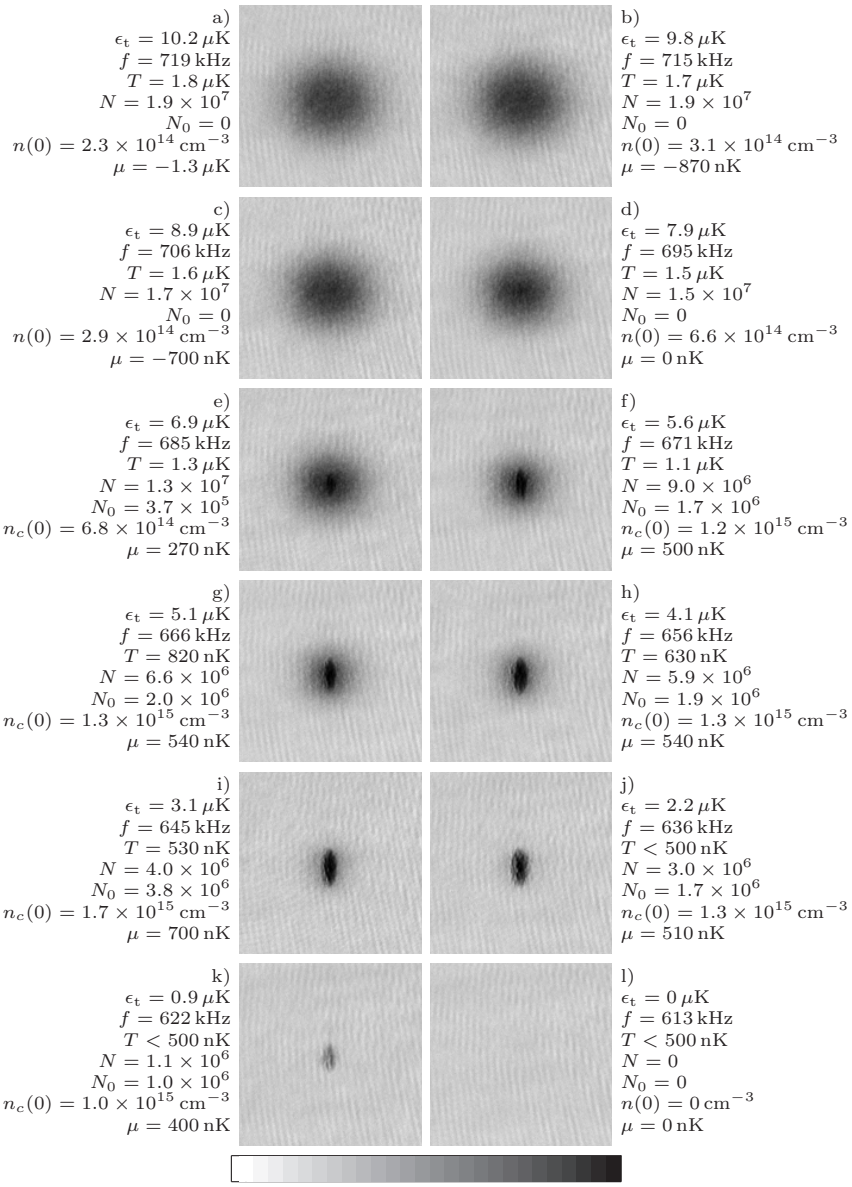

FIGURE 7.3: *Observation of Bose-Einstein condensation: The image series is taken for progressing evaporative cooling. The phase transition is reached at* $1.5\,\mu K$ *with* 1.5×10^7 *atoms (image d)). The condensate appears as a dense core in the center while the surrounding thermal component disappears. The highest number of condensed atoms is* 3.8×10^6 *(image i)). At low truncation energies the condensate is spilled from the trap. The size of the image is* $547 \times 547\,\mu m^2$*. The radial trap direction corresponds to the vertical direction in the image, whereas the z-direction is shown horizontally.*

laser of $-22\,\mathrm{MHz}$ was used, which corresponds to a photon absorption cross section of $6 \times 10^{-16}\,\mathrm{m}^2$.

Second, the central profiles of the optical density images are analyzed. Figure 7.4 shows profiles of the optical density along the axial and radial direction. The optical density profile $D_{\mathrm{th}}(y,z)$ is proportional to the column density profile of the thermal cloud $\eta_{\mathrm{th}}(y,z)$, which can be calculated by integrating the density profile given by Equations (2.17), and(2.9)

$$D_{\mathrm{th}}(y,z) = \sigma_\pi\, \eta_{\mathrm{th}}(y,z) = \sigma_\pi\, \eta_{\mathrm{th}}(0,0)\; \mathrm{g}_2\!\left(\tilde{z}\, \mathrm{e}^{-\frac{y^2}{y_0^2}-\frac{z^2}{z_0^2}}\right) / \mathrm{g}_2\left(\tilde{z}\right) \quad . \tag{7.2}$$

The curve obtained from a best fit of $D_{\mathrm{th}}(y,z)$ to the measured optical density profiles are compared to the data in Figure 7.4, a) and b). The temperature is deduced from the radial width y_0 of the profile $D_{\mathrm{th}}(y,0)$ (see [Ketterle et al., 1999])

$$T = \frac{m}{2k_{\mathrm{B}}} \left(\frac{\omega_\rho^2}{1+\omega_\rho^2\,\tau_{\mathrm{exp}}^2}\right) y_0^2 \quad . \tag{7.3}$$

It was found that the temperature obtained from the optical density profile along the z-direction was deviating from the temperature obtained from the profile along the radial direction even at long expansion times, the latter being lower. This deviation of about 50% remains unexplained. The thermal optical density profile was given in Equation (7.2) for a gas cloud in thermal equilibrium, in the absence of truncation of the energy distribution. For typical truncation parameters of $\eta > 4$ the systematic relative deviation due to the use of the equilibrium profile was estimated to be less than 10^{-3} and thus negligible. Well above the critical temperature the chemical potential can be determined by using the second fit parameter, which is the fugacity $\tilde{z}$

$$\mu = k_{\mathrm{B}} T\, \ln(\tilde{z}) \quad . \tag{7.4}$$

However, close to the critical temperature the value of the fugacity approaches unity, and the determination of the chemical potential becomes less precise. Below the critical temperature $\tilde{z} = 1$ is assumed. The central density of the thermal cloud can be derived from the fugacity and temperature by applying Equation (2.17).

In order to obtain information on the condensed cloud the Thomas-Fermi approximation is assumed, as discussed in Section 2.4. In the harmonic trap the density profile of the condensate is parabolic (compare Equation (2.46))

$$n_c(x,y,z) = n_c(0,0,0)\, \max\left\{1 - \frac{x^2}{R_x^2} - \frac{y^2}{R_y^2} - \frac{z^2}{R_z^2}, 0\right\} \quad , \tag{7.5}$$

where R_i are the dimensions of the condensed cloud. From the Literature ([Kagan et al., 1996]) it is known that during the expansion the parabolic density distribution of the condensate is preserved. This result holds for the collisionless regime, where $\omega_\rho \tau_{\mathrm{el}} \gg 1$. In the limit of a large aspect ratio of the unexpanded cloud, i.e. $\omega_\rho \gg \omega_z$ the dimensions

of the condensate evolve during the expansion as [Castin and Dum, 1996]

$$R_\rho(\tau_{\rm exp}) = R_\rho(0)\sqrt{1+\omega_\rho^2\,\tau_{\rm exp}^2} \quad , \tag{7.6}$$

$$R_z(\tau_{\rm exp}) = R_z(0)\left(1+\left(\frac{\omega_z}{\omega_\rho}\right)^2\left(\omega_\rho\,\tau_{\rm exp}\,\arctan(\omega_\rho\,\tau_{\rm exp})-\ln\left(\sqrt{1+\omega_\rho^2\,\tau_{\rm exp}^2}\,\right)\right)\right) \tag{7.7}$$

After integration of the parabolic density profile of the expanded cloud the optical density of the condensate images is found to be

$$D_{\rm c}(y,z)=\sigma_\pi\,\eta_{\rm c}(y,z,\tau_{\rm exp})=\sigma_\pi\,\eta_{\rm c}(0,0)\left(\max\left\{1-\frac{y^2}{R_y^2(\tau_{\rm exp})}-\frac{z^2}{R_z^2(\tau_{\rm exp})},0\right\}\right)^{\frac{3}{2}} \quad . \tag{7.8}$$

The curve obtained from a best fit of $D_{\rm c}(y,z)$ to the measured optical density profiles are compared to the data in Figure 7.4, e) and f). From the fit the size of the condensate in radial direction $R_\rho(\tau_{\rm exp})$ is obtained and with the help of Equations (7.6) and (2.47) the chemical potential is obtained

$$\mu=\frac{1}{2}m\,\omega_\rho^2 R_\rho(0)^2=\frac{m}{2}\left(\frac{\omega_\rho^2}{1+\omega_\rho^2\tau_{\rm exp}^2}\right)R_\rho^2(\tau_{\rm exp}) \quad . \tag{7.9}$$

The number of atoms follows from Equation (2.48)

$$N_0=\left(\frac{2\mu}{\hbar\bar{\omega}}\right)^{\frac{5}{2}}\frac{a_{ho}}{15a} \quad , \tag{7.10}$$

and the central density of the condensed cloud is given by

$$n_{\rm c}(0)=\frac{\mu}{g} \quad . \tag{7.11}$$

In Figure 7.4, c) and d) a optical density profiles of a cloud with both components, the thermal cloud and the condensate, are shown. The profiles are well described by the sum of the two optical density profiles of Equations (7.2) and (7.8). In practice, first the thermal profile is fitted from slightly beyond the Thomas-Fermi radius of the condensate on. The resulting curve is then subtracted from the data, and from a fitting procedure on the difference curve the condensate fraction is determined. Well below the critical temperature the thermal component outside the condensate region becomes so dilute that an accurate fitting procedure becomes impossible. Moreover, the presence of the interference fringes, which can be seen in the absorption images, leads to inaccuracy in the determination of the thermal optical density profile. In the present measurement the lowest detectable temperature is about 500 nK.

The temperature of the coldest measured cloud of the cooling sequence which shows no condensate fraction is taken as the critical temperature. With this procedure BEC occurs at a critical temperature of $T_{\rm C}=1.5\,\mu$K with $N=1.5\times10^7$ atoms and a critical peak density of $n_{\rm th}(0)=6.6\times10^{14}\,{\rm cm}^{-3}$. For rubidium gas samples this is the largest atom number at the critical temperature, which has been reported so far, and is

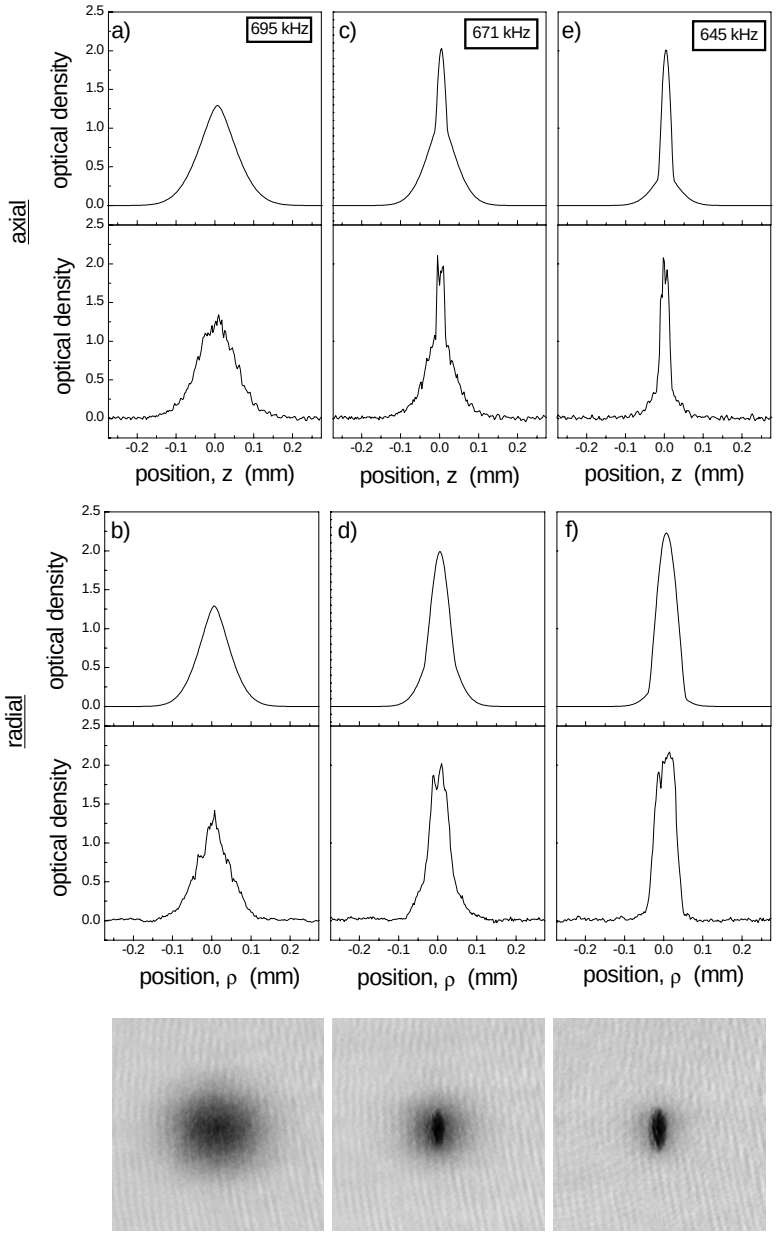

FIGURE 7.4: *Central optical density profiles along the z-direction (top) and along the radial direction (middle), as obtained from the absorption images (bottom) after* 6.3 *ms of expansion: The profiles of a cloud at the critical temperature (left), of a condensed cloud (middle), and an almost pure condensate (right) are compared to the theoretical curves as described in the text. The size of the image is* $547 \times 547\,\mu m^2$. *The radial trap direction corresponds to the vertical direction in the image, whereas the z-direction is shown horizontally.*

a consequence of the intense atom source and the steep magnetic trap developed in this experiment. The measured critical temperature is 16 % lower than the value of the critical temperature calculated from the atom number with Equation (2.23). From theoretical studies shifts of the critical temperature are expected. First, it is noted here that for a truncated energy distribution of the gas the evaluation of the integral in Equation (2.15) leads to a critical temperature in the limit of high truncation parameter η

$$T_{\mathrm{C}} = \frac{\hbar\bar{\omega}}{k_{\mathrm{B}}} \left(\frac{N}{g_3(1) - (1 - P(3,\eta))} \right)^{\frac{1}{3}} \quad , \tag{7.12}$$

where $P(x,\eta) \equiv \Gamma(x,\eta)/\Gamma(x)$ is the normalized incomplete gamma function and $\Gamma(x,\eta) \equiv \int_0^\eta \mathrm{d}t\; t^{x-1}\mathrm{e}^{-1}$ is the incomplete Euler gamma function. With $\eta = 5.1$ in the measurement presented in Figure 7.3 one finds a shift of +3.4 % of the predicted critical temperature with respect to Equation (2.23). Second, a shift in the critical temperature due to the interaction between the atoms on the order of −14 % for the current conditions was predicted by [Giorgini et al., 1996]. It is noted here that for the above described measurements 10 ms of plain evaporation at the end of the evaporative cooling ramp is used. This time is on the order of the time the condensate needs to form [Miesner et al., 1998, Gardiner et al., 1998]. For this reason it could be necessary to cool the gas slightly below the ideal gas value for the critical temperature to observe the condensate occurring. In measurements with 60 ms plain evaporation time at the end of the forced evaporative cooling ramp, a critical temperature of 1.5 μK with 8×10^6 atoms was observed, which is in good agreement with Equation (2.23). Clearly, a more systematic study of the formation of the condensate is desirable.

By further evaporative cooling of the gas below the critical temperature the number of atoms in the condensate increases to a maximum value of $N_0 = 3.8 \times 10^6$ at a density of $n_{\mathrm{c}}(0) = 1.7 \times 10^{15}\,\mathrm{cm}^{-3}$ and a chemical potential in units of temperature of $\mu = 700\,\mathrm{nK}$. The achieved chemical potential is much bigger than the harmonic oscillator energy for the radial direction in temperature units, which is 23 nK. Therefore, the condition described by Equation (2.45) is fulfilled, and the Thomas-Fermi approximation, which has been assumed above is justified. In order to determine, whether the gas is in the collisionless or hydrodynamic regime, the product of the trap frequency and the elastic collisional time has to be evaluated. This product is essentially the Knudsen number, the ratio the mean free path $1/(n\,\sigma)$ to the size of the sample. In the collisionless regime $\omega\,\tau_{\mathrm{el}} \gg 0.1$ and in the hydrodynamic regime $\omega\,\tau_{\mathrm{el}} \ll 0.1$. In the experiments under the conditions at the phase transition, a mean free path $\lambda_{\mathrm{mfp}} = 1/(n_{\mathrm{th}}(0)\,\sigma) = 1.7\,\mu\mathrm{m}$ and $\omega_\rho\,\tau_{\mathrm{el}} = 0.27$ and $\omega_z\,\tau_{\mathrm{el}} = 0.012$ are achieved, and the transition between collisionless and hydrodynamic regime is entered. This is comparable to the situation in BEC experiments with sodium [Stamper-Kurn et al., 1998b], where large gas samples with high atom numbers are achieved, but the elastic scattering cross section is about four times smaller compared to the case of rubidium. It is noted here that as the mean free path is smaller than the size of the sample, fast evaporative cooling must lead to temperature gradients in the gas. Presently, to the knowledge of the author no accurate theory is available to estimate temperature gradients in the sample in the transition region between the collisionless and the hydrodynamic regimes. Comment on the possibility to further explore the hydrodynamic regime will be given in Section 8.7.

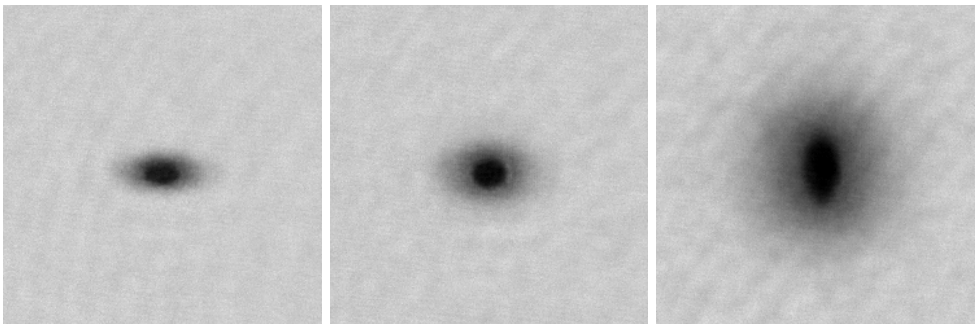

$\tau_{\mathrm{exp}} = 2.3\,\mathrm{ms}$	$\tau_{\mathrm{exp}} = 4.3\,\mathrm{ms}$	$\tau_{\mathrm{exp}} = 12.3\,\mathrm{ms}$
$r_{0,y} = 42\,\mu\mathrm{m}$	$r_{0,y} = 69\,\mu\mathrm{m}$	$r_{0,y} = 190\,\mu\mathrm{m}$
$r_{0,z} = 91\,\mu\mathrm{m}$	$r_{0,z} = 102\,\mu\mathrm{m}$	$r_{0,z} = 168\,\mu\mathrm{m}$
$R_\rho = 49\,\mu\mathrm{m}$	$R_\rho = 57\,\mu\mathrm{m}$	$R_\rho = 120\,\mu\mathrm{m}$
$R_z = 73\,\mu\mathrm{m}$	$R_z = 56\,\mu\mathrm{m}$	$R_z = 58\,\mu\mathrm{m}$

FIGURE 7.5: *Expansion of a Bose-condensed cloud: The thermal cloud changes from a prolate elliptical shape determined by the trapping geometry to an almost spherical shape reflecting the isotropic velocity distribution of the gas. The condensate reverses its aspect ratio during the expansion. The expansion is fastest in the direction of the strongest density gradient. The size of the image is* $767 \times 767\,\mu\mathrm{m}^2$. *The radial trap direction corresponds to the vertical direction in the image, whereas the z-direction is shown horizontally.*

Aside from analyzing the optical density profiles, another possibility of distinguishing between the thermal and condensed fractions of the cloud is to observe the aspect ratio during the free expansion of the cloud. In the Thomas-Fermi regime the kinetic energy of the atoms in the condensate can be neglected, and the shape of the trapped condensed cloud is a result of the balance between the external potential and the repulsive mean field interaction between the ^{87}Rb atoms (compare Equation (2.46)). As a result the Thomas-Fermi radius is much bigger as the size of the harmonic oscillator ground state, which would determine the condensate size for an ideal gas. As a consequence, the momentum spread of the condensate wavefunction is negligible and the expansion of the condensate is dominated by the repulsive mean field interaction. Once the confining forces are switched off, the cloud will expand fastest in the direction of the strongest density gradient, which is the radial direction. As already mentioned above (see Equations (7.6) and (7.7)) the parabolic shape of the cloud is preserved during the expansion. This behaviour can be seen in the absorption images in Figure 7.5, which show the evolution of a condensed cloud and the thermal component during the expansion. The images were taken after evaporative cooling to the same temperature and expansion times of 2.3 ms, 4.3 ms and 12.3 ms. Qualitatively, it can be seen from the pictures that the shape of the thermal cloud changes from a prolate ellipsoid ('cigar shape') to an almost isotropic sphere. The cylindrical symmetry of the magnetic confinement implies that the size of the cloud along the direction of observation is as big as the vertical size in the image. The isotropic shape at long expansion times reflects the isotropic velocity distribution of the atoms in the gas. However, it remains unexplained that at long expansion times the shape of the cloud

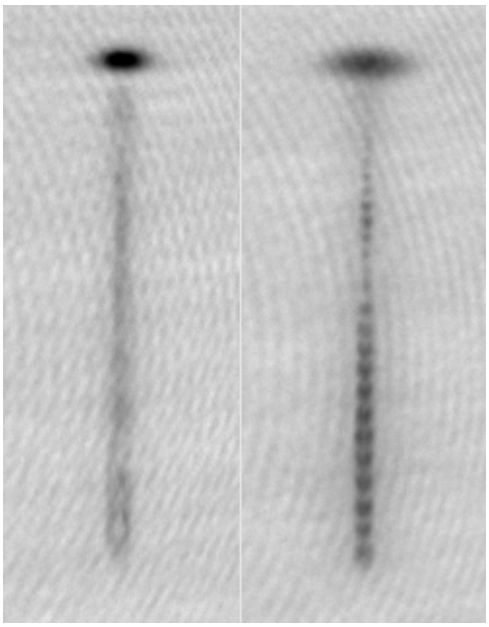

FIGURE 7.6: *Rf output coupler: Single frequency outcoupling (left) produces a continuous beam of atoms dropping out of the trap. Two frequency outcoupling (right) of the atoms at different energies of the trapping potential leads to interference of the atoms, which are accelerated by the earth gravitation. The size of the individual images is* $0.78 \times 2\,mm^2$.

deviates from being isotropic and the size of the cloud along the z-direction is slightly smaller than in the radial direction. In contrast to this, the shape of the condensed part changes from prolate to isotropic first, but at longer expansion times cloud is much longer in radial direction compared to the axial direction and becomes an oblate ellipsoid ('pancake' shape). In the image the condensed cloud appears to be elliptical again, but with a reversed aspect ratio, which is characteristic for the condensed cloud.

A second possibility to demonstrate the low momentum spread of the condensate wavefunction is to perform an experiment in which atoms are coupled out of the condensate by means of the rf-magnetic field also used for evaporation. This experiment was first carried out by [Bloch et al., 2000] in order to investigate phase coherence properties of the trapped gas, and is partially reproduced here. Rf-spilling at a truncation energy smaller than the chemical potential of the trapped condensate can be used to produce an atomic beam. Figure 7.6 (left) shows atoms dropping out of the magnetically trapped condensate over a period of 15 ms, if a single rf-frequency is used. If two oscillating fields rf-fields at two different truncation energies differing about $\Delta\epsilon_t \approx 100\,nK$ are used a modulation of constant spatial period over the outcoupled beam is observed, Figure 7.6 (left). This can be interpreted as the interference of two matter-waves which are coupled out of the trap at two different potential energies (two different rf-frequencies) and are

accelerated by the earth gravitation. As the momentum spread of the outcoupled atoms is low, the visibility of the pattern remains high over the observed dropping distance. In the literature the outcoupling of a beam of atoms from a condensate is often referred to as the realization of an so called 'atom laser'. However, investigation of second order phase correlation properties of the atomic beam is currently an open task.

Chapter 8

Cold clouds and Oort clouds

8.1 Introduction

Evaporative cooling in a magnetic trap as described in this thesis is a valuable tool to control the properties of ultra-cold gas samples at the BEC phase transition. A number of intrinsic phenomena related to BEC depend directly on the observation and control of temperature and atom number of the gas, e.g. the formation of the condensate [Miesner et al., 1998, Gardiner et al., 1998], the determination of the critical temperature [Ensher et al., 1996], the damping of elementary excitations [Jin et al., 1997, Fedichev et al., 1998], the existence of a critical velocity of a Bose-condensed gas [Raman et al., 1999], and Bosonic stimulation in inelastic decay of the condensate [Burt et al., 1997].

In the context of control over experimental parameters it is in particular interesting to study BEC related phenomena at the onset of the hydrodynamic regime with large samples of high density and atom number. Under these conditions the properties of quantum gases change fundamentally, but the control over the experimental parameters is difficult because of the presence of loss mechanisms and heat loads. A discussion of the origins of heating and loss has been presented by [Cornell et al., 1999, Myatt, 1997]. Here, two classes of processes should be distinguished. The first class concerns primary processes. At high densities intrinsic processes as three-body recombination and dipolar relaxation are limiting the life time of the sample. These inelastic density dependent processes give rise to particle loss as well as heating. Other primary limitations are due to the experimental techniques applied to produce the cold samples. Residual gases of the vacuum background can lead to collisional loss from the sample. Also photon scattering from near resonant stray light coming from an unshielded laser system leads to particle loss.

In addition to the above mentioned primary processes one may point to a class of secondary processes that give rise to particle loss and heating in a delayed fashion after a primary event. For example a grazing incidence collision with a background gas atom can result in a trapped atom of high energy. The presence of a cloud of such atoms will lead to heating of the cold cloud over extended periods of time.

In [Mewes et al., 1996a, Myatt, 1997, Burt et al., 1997, Stamper-Kurn et al., 1998a] the possible existence of a magnetically trapped cloud at energies much larger than the temperature of the cold cloud is discussed. In this context the name 'Oort cloud' was introduced. The name was given in analogy to the cloud of comets traveling far outside the orbit of Pluto, but being still bound to the gravitational field of the sun. The existence of this cloud was first proposed by the astronomer J. H. Oort [Oort, 1950].

Another example of a secondary process applies to the situation of small Knudsen numbers. In this case, the mean free path in the cold cloud is small and energetic atoms originating from an internal (3-body recombination) or external (Oort cloud) source will dissipate their energy in a cascade of collisions in the cold cloud.

Several groups reported heating and loss strongly depending on the density of the cold sample, but in the literature not much information can be found. So far, no comprehensive model of the underlying processes has been formulated. In general it was observed that heating and loss could be suppressed by limiting the depth of the magnetic trapping potential by means of an rf-shield preventing the possible build up of an Oort cloud. Also in the work for this thesis, if samples with a large particle number at high densities were produced, strong heating and loss in the absence of an rf-shield were observed.

In this chapter emphasis is put on the evidence for the existence and origin of Oort clouds as well as the consequences of the presence of an Oort cloud for the investigation of quantum gases. To investigate Oort cloud related phenomena cold clouds under conditions just above the BEC phase transition were used. Such clouds allow to study the essential phenomena and to trace the origin of the Oort cloud without the added complexity of the presence of a condensate. It will be demonstrated, how the effects of the Oort cloud on the cold cloud can be suppressed by means of rf-shielding. With the origin of the Oort cloud identified, a method for the reduction of the Oort cloud atom number will be demonstrated, and the effect of the Oort cloud on the cold cloud will be compared for large and reduced Oort clouds. The studies of secondary processes were done in the absence of an rf-shield, as in the presence of a rf-shield strong heating would lead to massive particle loss and could therefore not be distinguished from other loss processes. Finally, the consequences of the observations on the non condensed samples for the possibilities of entering the hydrodynamic regime with a Bose-Einstein condensate are discussed.

8.2 Time evolution of trapped cold clouds

Figure 8.1 shows how temperature, atom number, and density of an evaporatively cooled cloud are evolving in time. Evaporative cooling was followed by a trapping period t, during which the rf-power was switched off and the cloud was warming up. After this time the cloud was released from the trap. The expanded cloud was probed by absorption imaging. As the imaging is destructive the cloud was repeatedly produced for various trapping times t with the same initial conditions present after evaporative cooling. This procedure was carried out for two different initial conditions obtained by extending the evaporation ramp to different final temperatures. First, *Type I* clouds (circles) with 6.8×10^6 atoms at $1.6\,\mu$K temperature and $2.7 \times 10^{14}\,\mathrm{cm}^{-3}$ density were produced. This corresponds to a cloud of $r_{0,\rho} = 5.8\,\mu$m radial and $r_{0,z} = 135\,\mu$m axial size, and a

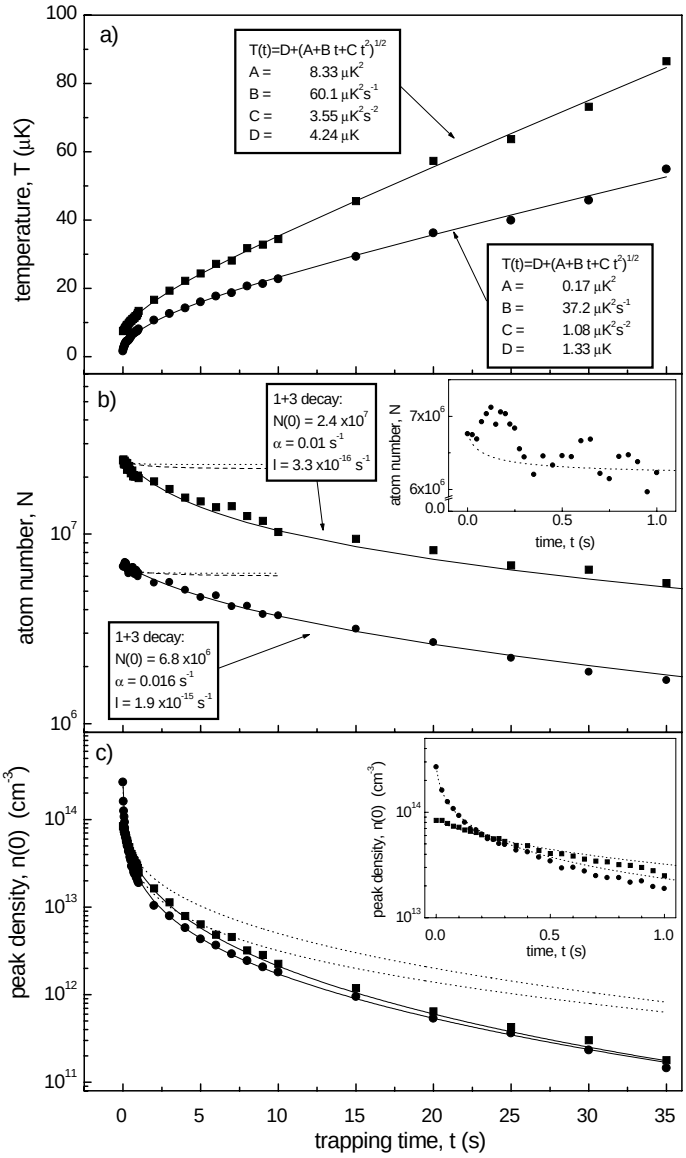

FIGURE 8.1: *Heating and loss of magnetically trapped clouds of Type I (circles) and Type II (squares). Based on the parameterization of temperature (solid line in a)) the density drop is calculated (dotted lines in c)). Including the parameterization of the atom number (solid line in b)) describes the density dependence (solid line in c)). Based on the density dependence the particle loss due to three-body recombination (dotted line in b)) and dipolar relaxation (dashed line in b)) is calculated.*

mean free path of $\lambda_{\rm mfp} = 4.7\,\mu$m, slightly smaller than the radial size. Therefore, under initial conditions the cloud is in the transition region between the collisionless and the hydrodynamic regime with a Knudsen number of $K_n = 0.8$. Here, the Knudsen number

$$K_n \equiv \frac{\lambda_{\rm mfp}}{r_{0,\rho}} \tag{8.1}$$

is defined as the ratio between the mean free path and the radial sample size. The second set of initial conditions, *Type II* clouds (squares), was a temperature of $7.5\,\mu$K with 2.4×10^7 atoms at $8.4 \times 10^{13}\,{\rm cm}^{-3}$ density. The dimensions of this cloud were $r_{0,\rho} = 12.6\,\mu$m and $r_{0,z} = 292\,\mu$m, with a $\lambda_{\rm mfp} = 15.1\,\mu$m mean free path. In this case $K_n = 1.2$.

The measurements exhibit strong heating of both types of cold clouds at initial rates of $20\,\mu$K/s (circles) and $6.8\,\mu$K/s (squares). After 10 s of trapping time the temperature increase becomes linear in time with rates of $1.2\,\mu$K/s (circles) and $2\,\mu$K/s (squares). The temperature behaviour can be nicely parametrized by the following test function

$$T(t) = D + \sqrt{A + B\,t + C\,t^2} \quad , \tag{8.2}$$

with the parameter values given in Figure 8.1,a). In this chapter emphasis is put on experiments with a large number of atoms. Transferring a reduced atom number into the magnetic trap leads to a reduced heat load.

The decay of the atom number is given in Figure 8.1,b). In order to parameterize the observed decays the data are fitted to an exponential decay where in addition a third order decay of the atom number is assumed

$$N(t) = \left(\frac{\alpha\, N^2(0)}{\alpha\, {\rm e}^{2\alpha t} - l N^2(0) + l N^2(0)\, {\rm e}^{2\alpha t}} \right)^{\frac{1}{2}} \quad . \tag{8.3}$$

The resulting parameters are shown as the solid lines in Figure 8.1,b).

The density as calculated for *Type I* and *Type II* clouds on the basis of measured temperature and atom number is shown in Figure 8.1,c). It is good to point out that the steep initial decline of the density is dominated by the rapid initial increase of the effective volume along with the temperature. To illustrate this point the dotted curves in Figure 8.1,c) show the density dependence calculated using the parameterization (Equation (8.2)) and neglecting the particle loss ($N \equiv$ const.). At short times the calculated curves describe the decline of the density, as can be seen from the inset. The calculated curves deviate for longer times when the particle loss contributes noticeably to the decrease of the density. If both parameterizations for the increase of temperature and for the atomic loss are taken into consideration, the decline of the density is well described (solid lines).

Based on the measured density dependence the three-body decay can be calculated using to the literature value of the rate constant $L = 1.8\,(5) \times 10^{-29}\,{\rm cm}^6{\rm s}^{-1}$ for the $|F = 2, m_F = 2\rangle$ state as measured by [Söding et al., 1999]. The result of this calculation is plotted in Figure 8.1,b), (dotted lines). For comparison also the dipolar decay is presented in Figure 8.1,b), (dashed lines). For this calculation the upper boundary of the rate constant $G = 2 \times 10^{-15}\,{\rm cm}^3/{\rm s}$ as given by [Julienne et al., 1997] was used.

Recent calculations suggest a value smaller than $1\times10^{-15}\,\mathrm{cm}^3/\mathrm{s}$ [Verhaar, 2000]. Rapidly, particle loss due to three-body recombination and dipolar relaxation becomes negligible. Only at short times three-body recombination is expected to enhance the decay, which is not inconsistent with the observed data. However, one should be reluctant in interpreting the observed evolution of the atom number in terms of intrinsic loss as for *Type I* clouds with slightly higher density even an initial increase of the atom number was found (see Figure 8.6,b)). Such an increase can possibly originate from atoms of the Oort cloud which have lost their kinetic energy after several collisions with atoms from the cold cloud and merge with the cold cloud.

The most striking feature of the data is the fast heating in presence of only a moderate particle loss. This heating rate can not be explained by relaxation heating, for instance due to three-body decay ('anti-evaporation') [Walraven, 1996]. This can explain initial heating rates of $0.8\,\mu\mathrm{K/s}$ and $0.3\,\mu\mathrm{K/s}$, much smaller than the observed initial rates for *Type I* and *Type II* clouds respectively. Clearly, it is likely that for gas clouds with a small atom number a substantial fraction of the recombination energy is dissipated in the cold cloud. Assuming full dissipation of the recombination energy to the highest vibrational level of the Rb_2 molecule ($\approx 1.1\,\mathrm{mK}$ [Verhaar, 2000]) results in a heat load of $4\times10^{-20}\,\mathrm{W}$, which is about a factor four bigger than the initial heat load of the sample.

A number of other possible origins of heating can also be excluded: First, during the measurements the atomic sample was carefully shielded from near resonant stray light from the laser system, which would induce atomic transitions to untrapped states. After such transitions the released hyperfine or Zeeman energy turns into kinetic energy of the atoms, which heat the cold cloud by collisions.

Second, rubidium atoms from the room temperature vacuum background gas can collide with atoms from the cold cloud. For grazing incidence collisions the kinetic energy transferred to the atoms in the cold can be smaller than the depth of the magnetic trap so that the atoms remain trapped, and the cloud is heated after thermalization by elastic collisions [Bali et al., 1999]. In order to obtain a measure for the amount of heating originating from background rubidium gas, the rubidium partial pressure in the UHV cell was reduced by desorbing the Rb atoms from the quartz cell with 250 W of light from halogen lamps put at a short distance of about 1 cm from the quartz surface. After a few minutes of exposure the rubidium partial pressure was reduced. The partial pressure was determined by measuring the capture rate from the background into the MOT without loading from the atomic beam source as has been described in Section 5.3. Although the accurate measurement of the *absolute* partial pressure depends critically on the knowledge of the capture velocity, the method allows to determine the *relative* reduction of the rubidium partial pressure. Even for a reduction of the rubidium partial pressure by a factor of 4 no reduction of the heating and atomic loss was noticed. It is emphasized here that with the argument presented in Section 5.3 it follows that also the effusive beam of rubidium atoms from the vapor cell does not contribute measurably to the observed heating and loss. This is in contrast to observations in experiments in which a Zeeman-slower is used as an atomic beam source. Due to limitations in differential pumping of the source significant rubidium partial pressure in the UHV cell can build up and contribute to the heating and loss [Aspect, 2000].

Third, it was also verified that no significant change in heating and losses occurred

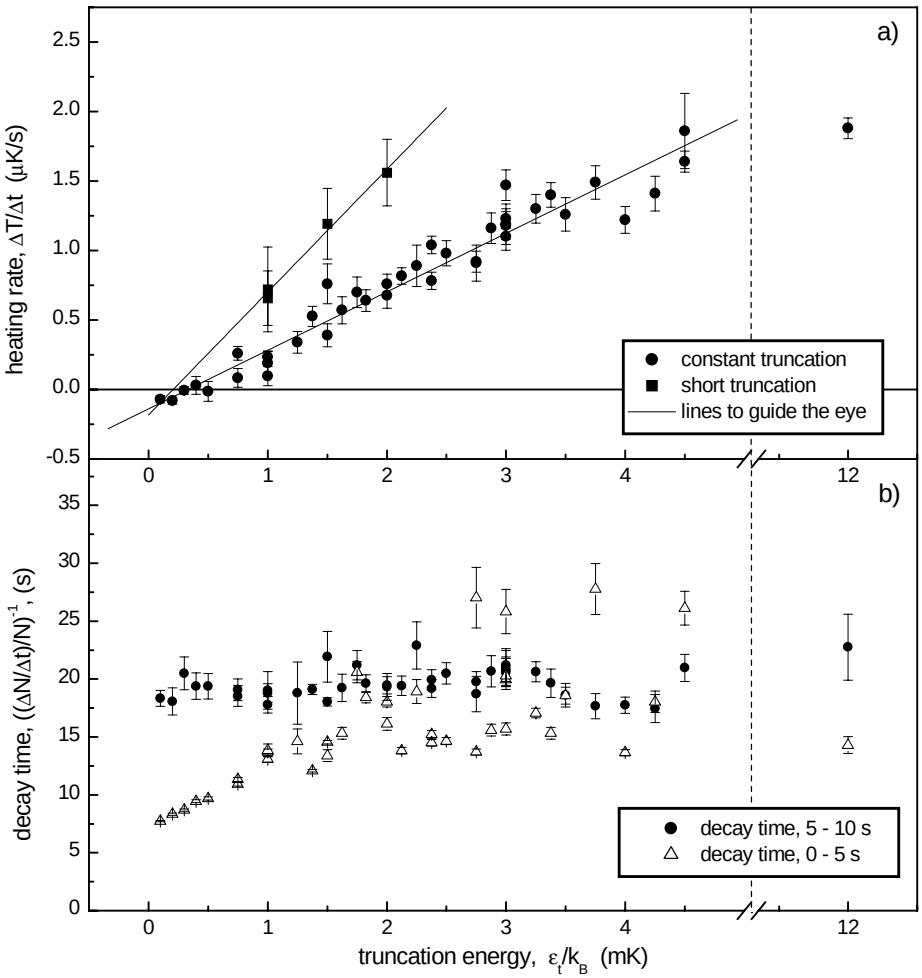

FIGURE 8.2: *Heating rate a) and decay time b) of a magnetically trapped cloud. The solid data points are obtained from measuring between* 5 *s and* 10 *s, the open triangles in b) are obtained after the first five seconds. During trapping rf-shielding was applied constantly (circles, triangles) at a truncation energy* ϵ_t. *In another measurement (squares), after* 4 *s of trapping at* $\epsilon_t = 4.7\,mK$, *the rf-shield was ramped down within* 0.5 *s to a final energy* ϵ_t *before set to* 4.7 *mK again. The error-bars result from averaging over 5 repeats.*

when the vacuum restgas pressure (air) was increased to the 10^{-10} mbar level.

In the literature rf-shielding methods are described to minimize the heating of the cold cloud [Cornell et al., 1999]. The argument presented is that atoms from an Oort cloud can give rise to a substantial heat load on the sample. This can be avoided by lowering

the depth of the trapping potential using an rf-shield. To investigate the effects of rf-shielding on the heating rate and particle loss the truncation energy ϵ_t of the rf-shield was varied between $100\,\mu$K and 4.5 mK. Without the shield the trap depth was 12 mK. For these measurements a '*Type I* -like' evaporatively cooled sample with 1.5×10^7 atoms at a temperature of $2.7\,\mu$K and a density of $2.4 \times 10^{14}\,\mathrm{cm}^{-3}$ was repeatedly produced. After evaporative cooling the truncation energy was increased to a constant value followed by a magnetic trapping time during which the cloud warmed up and the atom number was decaying. The measured heating and loss rates are the averaged quantities for the change in temperature and atom number between 5 s and 10 s, Figure 8.2, (circles). At these times the density has dropped to below $10^{13}\,\mathrm{cm}^{-3}$. As shown in Figure 8.2 the heating rates were strongly reduced by the rf-shield. With increasing truncation energy the heating rate increases linearly to a value of about $2\,\mu$K/s. This is supporting the picture in which an Oort cloud gives rise to the observed heating. It is remarkable that the 18 s decay time observed in the interval $5 - 10$ s does not significantly depend on the truncation energy. Therefore, it is concluded that the observed decay is uncorrelated with the heating. As background collisions with rubidium and air restgas particles can be excluded, another loss process has to be assumed, but remains so far unexplained.

The initial decay over the first five seconds is shown in Figure 8.2, b), (triangles). For low truncation energies the decay time is seen to decrease. As under these conditions the density decay due to heating as observed in Figure8.1, c), is strongly reduced, enhanced particle loss due to density dependent loss mechanisms must become visible. The initial decay time of 7 s observed for the lowest truncation energy is consistent with this picture. Three-body recombination loss was studied for low truncation energies by [Söding et al., 1999, Schuster et al., 2000].

Further evidence for the existence of an Oort cloud is obtained by applying a temporary rf-shield. For the measurement shown in Figure 8.3 (open circles) again a '*Type I* -like' cold sample was produced with the same initial conditions as used in the measurements presented in Figure 8.2. In a first measurement (solid circles) after evaporative cooling the truncation energy was set constantly to $\epsilon_t = 4.7$ mK. In a second measurement (open circles) after 4 s of magnetic trapping a rf-frequency ramp was started for a period of 0.5 s. The frequency was ramped down linearly such that a truncation energy of $\epsilon_t = 420\,\mu$K was reached. Subsequently, the truncation energy was reset jump wise to $\epsilon_t = 4.7$ mK. As can be seen from the plot after applying the rf-ramp, the heating rate was strongly reduced by a factor of 6 from $2.5\,\mu$K/s to approximately $0.43\,\mu$K/s. The latter measurement was repeated with different final truncation energies of the ramp. The observed residual heating rate is shown in Figure 8.2. The data suggest that it is possible to further suppress the residual heating rate by extending the truncation ramp to lower final truncation energies and to perform the ramp less steep. At the same time the data put an upper limit for the heating rate which is continuously generated, as e.g. heating due to background collisions. For the same measurement no significant change in the decay of the atom number was observed. This is consistent with the above described case where the truncation was applied constantly. Before the heating rate caused by an Oort cloud is studied in more detail, first a more direct method for the detection of the Oort cloud is introduced in the following sections.

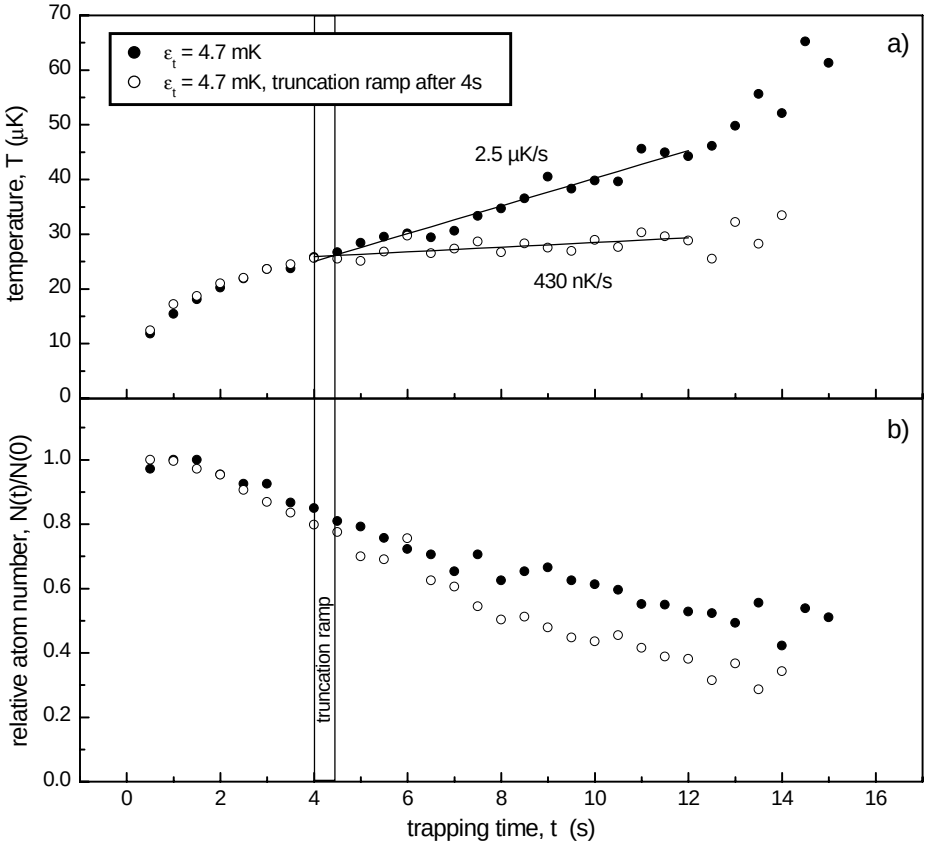

FIGURE 8.3: *Temperature a), and atom number b) of a magnetically tapped cloud of initially* 2.3×10^7 *atoms at* $2.7\,\mu K$*: For a deep trap heating at* $2.5\,\mu K/s$ *occurs (solid circles). Ramping down the trap depth at* $4\,s$ *over a period of* $0.5\,s$ *from a truncation energy of* $4.7\,mK$ *to* $420\,\mu K$ *(open circles) heating can be permanently reduced to* $0.43\,\mu K/s$*, whereas no significant change in the atomic loss was found.*

8.3 Observation of the Oort cloud

This describes how the Oort cloud can be detected by release of the contents from the magnetic trap and subsequent recapture into a MOT. By first spilling the cold cloud out of the magnetic trap with the radio frequency knife before the release only atoms at high energy, the atoms of the Oort cloud, are recaptured. From a time-of-flight (TOF) analysis the Oort-cloud atom number and energy distribution is obtained.

As the Oort cloud is populated with only a few atoms over a wide energy range, it is not possible to achieve a detectable optical density for absorption imaging. In order to demonstrate the presence of the Oort-cloud and measure its atom number, the atoms were released from the magnetic trap and recaptured into a MOT. This was done after initially

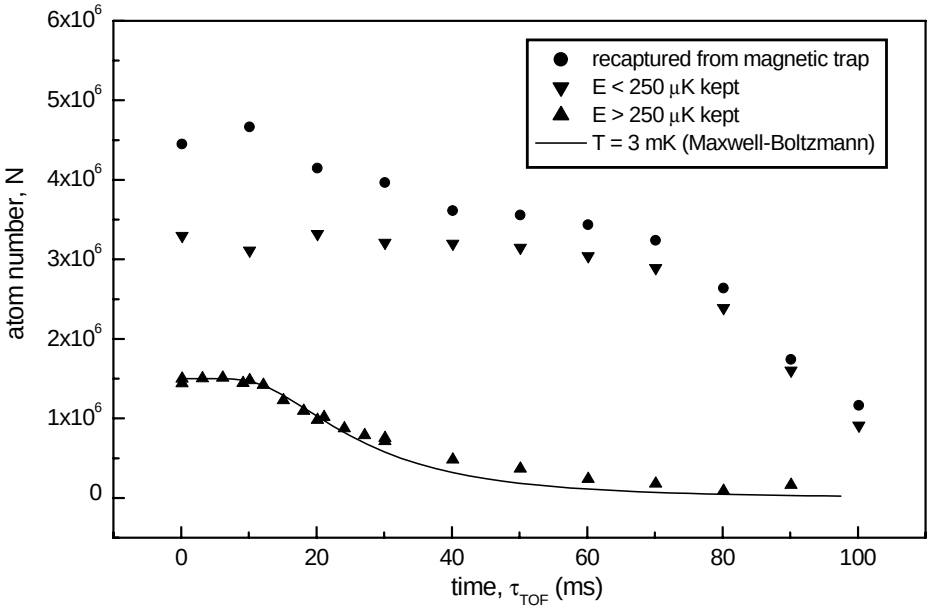

FIGURE 8.4: *Time-of-flight measurement of the number of atoms captured after release from the magnetic trap into a MOT. If the full trap contents were recaptured, a bimodal time-of-flight spectrum was measured (cirles). Before release from the magnetic trap atoms at energies* $> 250\,\mu K$ *were spilled out of the trap by an rf-knife and not recaptured (triangles down), resulting in a TOF spectrum of the cold gas cloud with less atoms left at short times. After spilling atoms of energies* $< \epsilon_t = 250\,\mu K$ *only atoms from the Oort cloud were recaptured (triangles up) vanishing after short times in the TOF spectrum. The calculated TOF spectrum of* $3\,mK$ *thermal cloud (solid line) is in fair agreement with the observation for the Oort cloud.*

producing an evaporatively cooled cloud of about 10^7 atoms at a temperature of $2\,\mu$K (*Type I* cloud). The evaporative cooling ramp was followed by a period of 60 ms magnetic trapping, during which the radio frequency was kept constant. Subsequently, the atoms were released from the magnetic trap. In order to recapture the rapidly expanding Oort-cloud into a MOT additional power supplies were used allowing to switch on the MOT magnetic fields within $300\,\mu$s. By choosing a $14.6\,$G/cm magnetic field gradient along the z-direction and a laser detuning of $-25\,$MHz the capture range of the MOT was extended over the whole vacuum quartz cell. Again, it was advantageous to work with a MOT with large laser beam diameters at high laser power so that the whole magnetic trapping volume was covered. Significant loading of the MOT from the vacuum background was prevented by limiting the MOT trapping time to 50 ms before the atoms were released again, and subsequently, the number of atoms was measured by absorption imaging as described in Section 5.2. In order to measure the energy distribution of the atoms in the cloud the expansion time τ_{TOF} between the release and recapture was varied, and by

measuring the number of atoms still being recaptured a time-of-flight (TOF) spectrum was obtained. During the expansion atoms with high energy will stick to the walls of the vacuum cell first and will not be recaptured.

Figure 8.4 (circles) shows the TOF spectrum obtained by this measurement procedure. The TOF spectrum shows a bimodal structure. At short times ($\tau_{\mathrm{TOF}} < 40\,\mathrm{ms}$) corresponding to high energies the number of recaptured atoms drops by about 10^6 atoms. This reflects fast atoms of the Oort cloud to escaping from the capture range of the MOT. At longer times ($\tau_{\mathrm{TOF}} > 50\,\mathrm{ms}$) the number of atoms vanishes as the cold cloud expands and also drops out of the capture region.

In a second measurement (triangles down), a rf-knife was used to spill atoms from the magnetic trap after evaporative cooling and before the release. The rf-knife was ramped from a truncation energy of $\epsilon_t = 4.7\,\mathrm{mK}$ down to $\epsilon_t = 250\,\mu\mathrm{K}$ in order to remove the Oort-cloud atoms from the trap. As a consequence, the first step in the TOF spectrum is not observed.

In the third measurement (triangles up), the cold cloud was spilled from the magnetic trap by applying a rf-truncation ramp starting from $\epsilon_t = 250\,\mu\mathrm{K}$ to the bottom of the trap. The obtained TOF spectrum shows how the Oort cloud escapes from the capture region. At $\tau_{\mathrm{TOF}} = 0\,\mathrm{ms}$ the number of Oort cloud atoms is read out. In this measurement at the end of evaporative cooling about 1.5×10^6 atoms were found populating the Oort cloud at energies $> 250\,\mu\mathrm{K}$.

The measured TOF spectrum of the Oort cloud was compared to a calculated curve (solid line). For simplification it was assumed that the Oort cloud obeys a Maxwell-Boltzmann distribution. The spatial integration of the expanded density distribution over the capture region of the MOT gives the number of recaptured atoms as a function of the expansion time. Figure 8.4 shows that a temperature of 3 mK, smaller than the 12 mK trap depth, is suggested by the data. The Oort cloud is not expected to obey a Maxwell-Boltzmann distribution, as the calculated peak density of the Oort cloud in the magnetic trap is $8 \times 10^6\,\mathrm{cm}^{-3}$, and thus a thermalization time in the order of 200 s is to be expected.

8.4 Decay of the Oort cloud

The recapture of the magnetic trap contents into the MOT can be done at any time during magnetic trapping. This allows a time-resolved measurement of the Oort cloud population. In this section the decay of the Oort cloud in absence of the cold cloud is described. For the measurements, loading of the magnetic trap was done as described in Chapter 6. The evaporative cooling ramp was extended to a truncation energy less then the magnetic potential in the trap center in order to first produce a cold cloud and finally remove this cloud from the trap. Magnetic trapping of the Oort-cloud was followed by the transfer of the atoms into the MOT with energies larger than $250\,\mu\mathrm{K}$.

Two experimental situations are compared: First, the decay of the Oort cloud during magnetic trapping in absence of the cold cloud was measured. Second, this was compared to the decay of the Oort cloud, also without cold cloud, but in presence of an evaporative cooling shield at low truncation energy of $\epsilon_{\mathrm{t}} = 12.5\,\mu\mathrm{K}$ during the magnetic storage. The rf-shielding experiment was done for two different rf-amplitudes, $B_{\mathrm{rf}} = 40\,\mathrm{mG}$ and

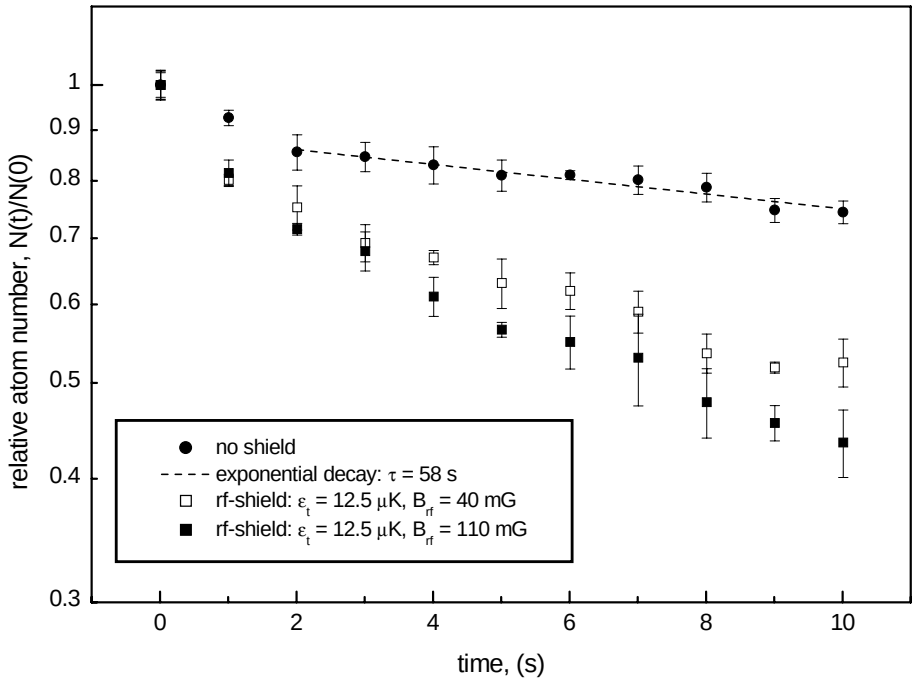

FIGURE 8.5: *Decay of the Oort cloud atom number in the absence of a magnetically trapped cloud at low temperature: After* 3 *s the Oort cloud decays exponentially with a life time of* 58 *s (circles). In presence of an rf-shield at* $\epsilon_t = 12.5\,\mu K$ *(squares) the initial relative decay rate was increased from* 0.07 */s to* 0.125 */s and not significantly depending on the rf-amplitude. The error-bars result from averaging over 3 repeats.*

$B_{\rm rf} = 110\,$mG. The measured decay curves of the Oort cloud atom number are shown in Figure 8.5. From the logarithmic scale of the graph it can be seen that the decay is not following an exponential law. The initial decay rate per atom is increased to 0.125 /s in the presence of the rf-shield, with respect to a decay rate per atom of 0.07 /s without the shield. Without the rf-shield the decay time after 3 seconds was 58 s. The observed decay was not significantly changed by increasing the rf-amplitude. Assuming an energy of 3 mK for an atom results in a Landau-Zener transition probability to untrapped states of 0.7 and 0.05 respectively (compare Figure 2.4), for the rf-amplitudes in use. From this follows, that the atom has to undergo several trap oscillations, before it is removed from the trap. However, the observed decay rate in presence of the shield is much longer than several times the $2\pi/\omega_z = 49\,$ms axial oscillation time of the magnetic trap. The long decay time is then an indication that it takes a long time before the Oort cloud atoms reach the rf-shield.

8.5 Controlling the Oort cloud population

In order to control the Oort cloud population the mechanism how the Oort cloud becomes populated must be identified. In [Cornell et al., 1999] several possible origins have been discussed: For example, the Oort cloud population can arise after three body recombination or grazing incident collisions with background particles.

In this experiment another reason for the population of the Oort cloud was identified. As presented in Section 8.4 a substantial Oort cloud population was found to be present immediately after completing the evaporative cooling ramp. The major fraction of the Oort cloud population is attributed to residual atoms resulting from incomplete evaporative cooling occurring at high truncation energies [Desruelle et al., 1999]. From Equation 2.3 it follows that at a magnetic field amplitude of

$$B = \sqrt{\frac{\hbar\omega_{\mathrm{rf}} B_{\mathrm{rf}}}{8\mu_{\mathrm{B}} g_F}} \tag{8.4}$$

the difference in the energy of the transitions $m_F = 2 \rightarrow m_F = 1$ and $m_F = 1 \rightarrow m_F = 0$ due to the quadratic Zeeman effect becomes equal to the Rabi frequency ω_{R} by which the transitions are driven. For a typical rf-magnetic field amplitude of 50 mG this condition is fulfilled at a magnetic field of 20 G corresponding to a truncation energy of 1.3 mK. As a consequence, not all atoms at high truncation energies energies are removed from the magnetic trap [Desruelle et al., 1999]. As evaporative cooling starts with 4×10^9 atoms and at a truncation energy of 1.3 mK about 1.1×10^9 atoms remain, a fraction of about 10^{-3} of the atoms on average has to remain in the trap in order to explain the observed Oort cloud.

It is often overlooked that not only in magnetic traps with large offset field [Desruelle et al., 1998] incomplete evaporation due to the quadratic Zeeman effect occurs, but also in magnetic trapping geometries as described by [Mewes et al., 1996a, Myatt et al., 1997, Esslinger et al., 1998] magnetic field strengths of relevant order are achieved.

In order to suppress the population of the Oort cloud in the present experiment a modified scheme was used, in which adiabatic compression and evaporative cooling were combined and the production of atoms at high energies was avoided. Loading of the magnetic trap was performed in the standard way followed by adiabatic compression until the third compression step was finished, as described in Section 6.2 and summarized in Table 6.1. The third step of the adiabatic compression was immediately followed by the compensation of the offset magnetic field (called fifth step in the table). At this point the quadrupole magnetic field gradient α, and thus the depth of the magnetic field has still to be increased to its maximum value. In order to allow this, but avoiding the production of atoms at high energies as the temperature of the compressed cloud rises, an evaporative cooling shield at a frequency of 14 MHz corresponding to a truncation energy of 1.3 mK with a rf-magnetic field amplitude of 100 mG is switched on. In the presence of this shield the magnetic field gradient α is ramped up to its maximum value over a period of 8 s (formerly the fourth step of the compression). Subsequently, a fast frequency ramp starting from 50 MHz to 14 MHz was applied for 1 s in order to remove atoms at high energies. From 14 MHz on the evaporative cooling ramp was applied as described in Section 7.1. As a result of applying this modified compression and evaporative cooling

scheme, the number of atoms in the Oort cloud was found to be strongly reduced. The best reduction of the Oort cloud was obtained by starting the final evaporation ramp-down not at 14 MHz but from 50 MHz. Apparently, the rf-shield is not fully effective. With this procedure a reduction of the Oort cloud population by a factor of 6 was achieved. The above experiment convincingly demonstrates that incomplete evaporation is responsible for the major fraction of the observed Oort cloud population. However, the removal of the Oort cloud turned out to be incomplete. Therefore, other sources cannot be excluded, such as trapped atoms produced by three-body recombination at high density in the cold cloud during the final stage of evaporation.

8.6 Heating due to the Oort cloud

The reduction of the Oort cloud population makes it possible to investigate the influence of the Oort cloud atom number on the heating of the cold cloud due to collisions. Figure 8.6 shows the time evolution during magnetic trapping of a) temperature, and b) atom number of the cold cloud, as well as c) the Oort cloud atom number. In these experiments a '*Type I*-like' cloud was used with initially 10^7 atoms at 1.7 μK temperature and a density of $4.2 \times 10^{14}\,\mathrm{cm}^{-3}$. Temperature and atom number of the cold cloud were measured without applying rf-shielding, using the procedure described in Section 8.2. This measurement was then followed by the measurement of the Oort cloud atom number for the same conditions of the cold cloud, using the method described in Section 8.3. These measurements were repeated in order to compare two situations: They were first done with a large initial number of atoms in the Oort cloud of 2.2×10^6 (solid data points). The measurements were then repeated for a reduced Oort cloud atom number of 3.7×10^5 (open data points) achieved by the method described in Section 8.5. At short times heating rates of 30.5 μK/s for a large Oort cloud and 16.5 μK/s for a reduced Oort cloud were measured. After five seconds of trapping the the heating rates were reduced to 2.3 μK/s and 1.2 μK/s. Thus, the heating rate was reduced by almost a factor 2, whereas the number of atoms in the Oort cloud was initially reduced by a factor of 6. In the measurement presented only atoms at energies higher than 250 μK are considered to belong to the Oort cloud. Clearly, the heating rate does not scale linearly with the Oort cloud population. However, this is not to be expected either, as the Oort cloud reduction procedure is expected to result in a different energy distribution of the Oort cloud atoms. Unfortunately, the small atom number in the reduced Oort cloud does not allow a measurement of the energy distribution. Moreover, atoms in the energy range up to 250 μK are not detected. Therefore, the strong residual heating after the reduction of the Oort cloud could be explained by heating due to trapped atoms with energies below 250 μK.

Another important experimental observation is described in the following. As already mentioned in Section 8.2, in the measurement presented in Figure 8.6,b) an increase of about 1.5×10^6 atoms in the atom number of the cold sample was observed during the first 500 ms of magnetic trapping in presence of a non-reduced Oort cloud (solid circles). At the same time the Oort cloud atom number is reduced by 6×10^5 atoms, as can be seen from Figure 8.6,c) (solid squares). For a reduced Oort cloud atom number this initial increase of the cold sample and the loss of Oort cloud atoms are not observed.

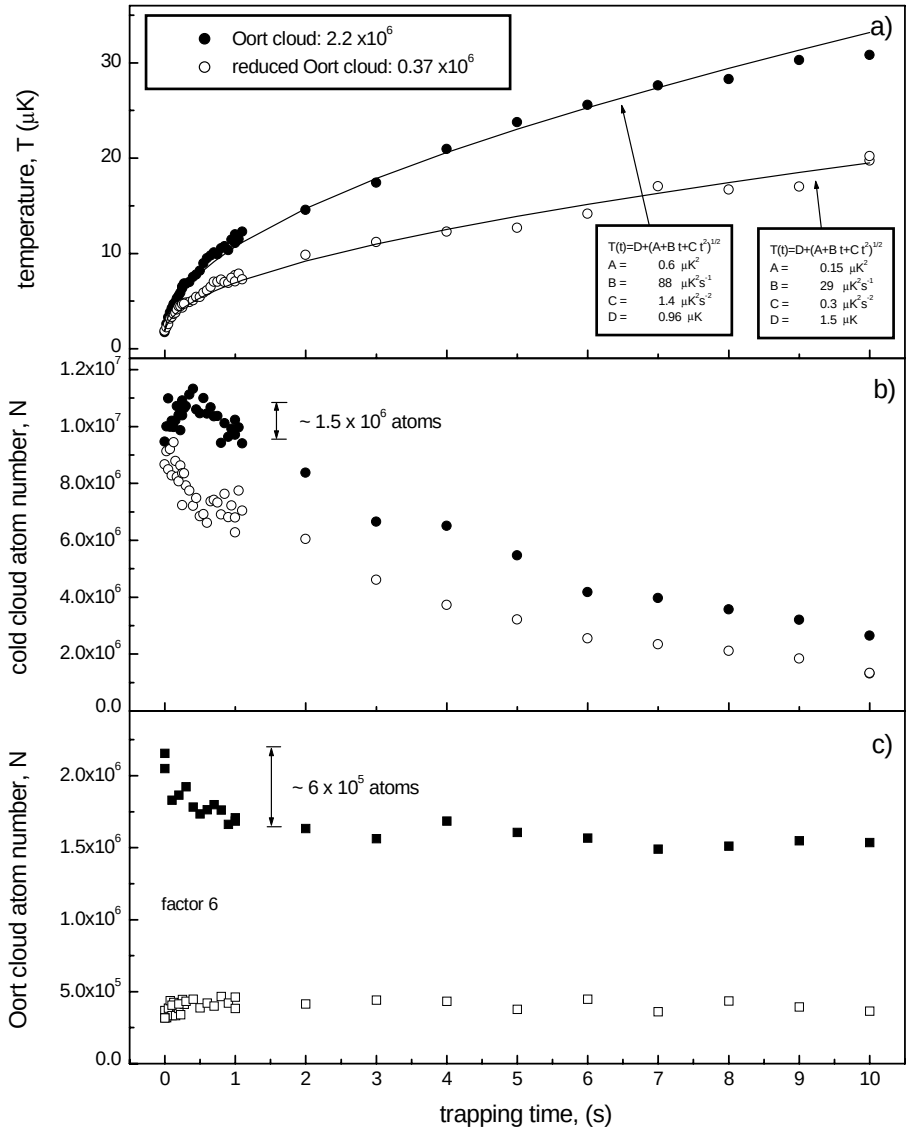

FIGURE 8.6: *Heating a), and atom loss b) of the cold cloud (Type I), obtained by absorption imaging, in comparison for a large Oort cloud (filled data points) and a reduced Oort cloud (open data points). The Oort cloud atom number c), obtained by the recapture method, was initially reduced by a factor* 6. *The heating is reduced at short times as well as at long times by a factor of 2. In presence of a large Oort cloud an increase of the atom number of the cold cloud within the first* 500 *ms is accompanied by a reduction of the Oort cloud atom number. This is interpreted as capture of atoms from the Oort cloud into the cold cloud by collisions. For a reduced Oort cloud this behaviour is absent.*

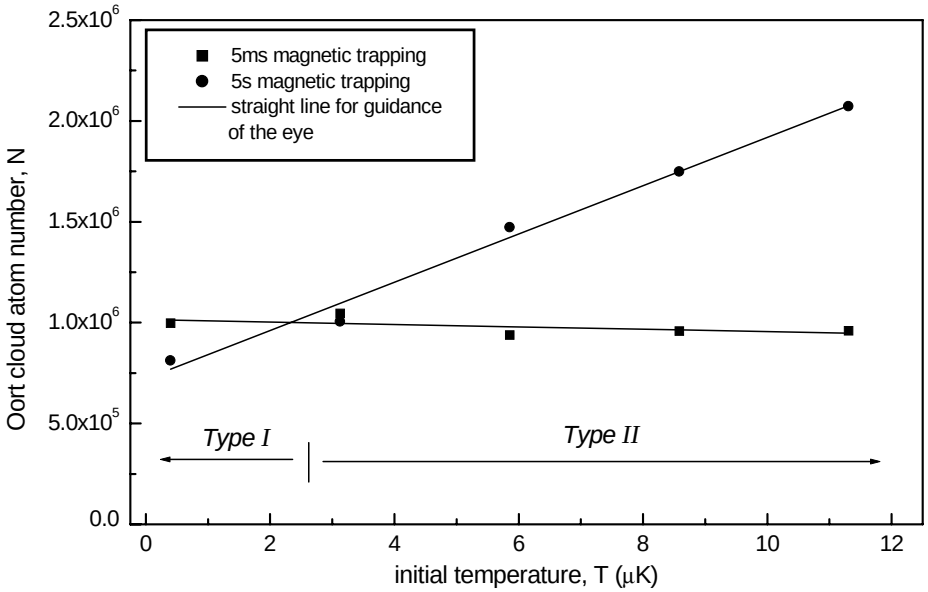

FIGURE 8.7: *Atom number of the Oort cloud after* 5 *s of interaction with a cold cloud for different initial temperature. For low initial temperature a l0ss in the Oort cloud atom number is observed (Type I). For high initial temperature the Oort cloud atom number increases (Type II).*

The question arises, how more atoms can be captured by the cold cloud than lost from the Oort cloud? As capture from the background gas can be excluded (no particle increase for reduced Oort clouds) this discrepancy is attributed to low energy Oort cloud atoms ($< 250\,\mu$K) which are not recaptured in the MOT when measuring the Oort cloud atom number. Comparing the loss of atoms from the Oort cloud with the increase of atoms in the cold cloud is concluded that approximately 40% of the Oort cloud atoms are detected by recapture into the MOT. It is unknown which fraction of the reduced Oort cloud is detected. This uncertainty can at least partially explain the non-linear relation between the heating rate and the Oort cloud population. Calculating the heat load due to capture of atoms from the cold on the basis of the measured increase of the cold cloud atom number one finds that an average energy of $E/k_{\mathrm{B}} \approx 130\,\mu$K per captured atom is dumped into the cold cloud. This result is consistent with the picture in which the heating of the cold cloud is predominantly generated by the Oort cloud. For *Type II* clouds, as presented in Figure 8.1, (squares), a different behaviour was found: For a high as well as low initial atom number in the Oort cloud no initial increase in the atom number of the cold sample was found, and always a increase in the Oort cloud atom number during the first seconds of magnetic trapping. This behaviour is demonstrated by the measurements presented in Figure 8.7. In these measurements the initial Oort cloud population (squares) is compared with the Oort cloud atom number after 5 s of magnetic trapping (circles). This measurement was done under variation of the initial

parameters of the cold sample by extending the evaporative cooling ramp to different initial temperatures of the cold sample. In this way the initial conditions of the cold cloud were varied between *Type I* -like and *Type II* -like. While the initial number of the Oort cloud does not significantly depend on the type of the cloud, the Oort cloud population after five seconds of magnetic trapping linearly increases with increasing initial temperature. At high initial temperature of 11 μK (*Type II* cold cloud) the Oort cloud number doubles from 1×10^6 atoms to 2×10^6 atoms. At low initial temperature (*Type I* cold cloud) a decay of the Oort cloud atom number was found to accompanied by an increase of the atom number in the cold sample as shown in Figure 8.6.

The loss from the Oort cloud population accompanied by the increase in the cold sample is interpreted as capture of atoms from the Oort cloud by the cold sample. As for *Type I* clouds the mean free path is smaller than the size of the sample, Oort cloud atoms are indeed expected to be captured by the cold cloud in a cascade of collisions. Less than 10 collisional stages of the cascade are expected to be required for full thermalization. The presence of a d-wave resonance [Burke et al., 1998, Verhaar, 2000] in the elastic collisional cross-section is favorable for containment of the colliding atoms in the cloud.

For the *Type II* cloud the ratio of mean free path to the size of the sample (Knudsen number) is increased. For the *Type I* cloud described in Figure 8.6 the Knudsen number is $K_n = 0.6$, whereas for the *Type II* cloud of Figure 8.1 $K_n = 1.2$ is calculated. The measurements show that no initial increase of atom number is observed but only loss. Apparently, collisions are not leading to an appreciable capture of Oort cloud atoms in this case. In fact, the decay of cold cloud atom number is present right from the start and is accompanied by an increase of the Oort cloud number. Also the heat load per atom is strongly reduced. Comparing the *Type I* and *Type II* clouds from Figure 8.1 a reduction of the heat load per atom by a factor of 8 was measured, while the ratio of mean free path to the sample size increases by only 50%. Apparently, for *Type II* clouds the rate at which atoms are kicked out of the sample exceeds the recapture rate. No detailed model to describe the thermalization of the cold cloud with the Oort cloud was attempted.

8.7 Summary and conclusions

In the following the results obtained in this chapter are summarized:

- Recapture of the magnetic trap contents into a MOT after removal of the cold cloud allowed for a observation of a magnetically trapped Oort cloud. This proofed to be a useful method to gain information, at any desirable time, about the atom number and energy distribution of the Oort cloud. In the experiments presented in this chapter, an Oort cloud of a few million atoms was populating the magnetic trap at energies up to several mK.

- The primary origin of the observed Oort cloud, described in this chapter, was identified to be incomplete rf-evaporation of the atoms in high magnetic fields due to the quadratic Zeeman effect. Typically the quadratic Zeeman effect becomes important at a field strength of 20 G, a value which also occurs in magnetic traps used by other groups. The Oort cloud atom number was strongly reduced to 3×10^5 by avoiding

the production of atoms at high trapping energies applying an experimental scheme which combines adiabatic compression and evaporative cooling.

- Aside from the initial creation of an Oort cloud also secondary development of the Oort cloud atom number was observed. Depending on the Knudsen number of the cold cloud either increase or decrease of the Oort cloud atom number was observed. For the lowest Knudsen numbers loss of atoms from the Oort cloud was accompanied by an increase of the atom number of the clod cloud by even 1.5×10^6 atoms. For obvious reasons three body decay never can explain the initial increase of the atom number observed for the cold cloud. The increase is attributed to capture of atoms from the Oort cloud in a collisional cascade. In contrast, using large Knudsen numbers an increase of the Oort cloud atom number was observed at the expense of atoms from the cold cloud.

- Atoms from the Oort cloud lead to substantial heating of the cold sample. The observed heating rate was strongly reduced by applying rf-shielding. A rough estimate of the heat load is consistent with this picture. The observed loss rate over the period $5 - 10\,\mathrm{s}$ was was not influenced by the rf-shield. The initial decay time (over the first 5 s) was seen to decrease for low truncation energies. This is consistent with three-body decay in the absence of additional heating. In case of a cold cloud of low density, removal of the Oort cloud by a short truncation ramp led to a permanent reduction of the heating rate. It is important to point out that to investigate the influence of the Oort cloud on the cold cloud it is advantageous to measure in the absence of rf-shielding, as done in the experiments for this thesis. In the presence of shielding strong heating will show as massive particle loss due to evaporation. In the latter case, it will be difficult to distinguish between intrinsic heating and loss mechanisms.

The existence of collisional cascades is of great importance for attempts to investigate Bose-Einstein condensates in the hydrodynamic regime, where even lower ratios of the mean free path to the sample size have to be achieved. Even in the presence of rf-shielding it seems important to remove an Oort cloud. A a certain fraction of the Oort cloud atoms will always travel through the cold sample leading to a collisional cascade, even if these atoms were flipped to untrapped states after entering the shielded region. In order to avoid this, rf-shielding at two different truncation energies can be helpful. Also confining the atoms in optical traps or micro-fabricated magnetic surface traps avoids the undesired effects of an Oort cloud, as the depth of these trapping potentials is small. Also, three-body decay is expected to give rise to collisional cascades at high densities. This has been investigated by [Schuster et al., 2000]. For a condensate the three-body recombination rate constant is suppressed by the quantum statistical factor ≈ 6 with respect to the rate constant for the uncondensed cloud described in this chapter [Kagan et al., 1985, Burt et al., 1997]. However, as demonstrated in Chapter 7 the densities achieved in a Bose-Einstein condensate are typically a factor $2 - 3$ higher than the density of the thermal cloud, compensating the quantum statistical factor. Therefore, it is a slight improvement to Bose-condense ^{87}Rb in the $|F = 1, m_F = -1\rangle$ state, for which the three-body recombination rate constant is smaller by a factor of 3 [Burt et al., 1997] compared

to the $|F = 2, m_F = 2\rangle$ state. Moreover, using the $|F = 1, m_F = -1\rangle$ state incomplete evaporation due to the quadratic Zeeman effect is also avoided [Desruelle et al., 1999].

Working at a limited density, one possibility to enter deeply into the hydrodynamic regime could be to tune the elastic scattering length in the vicinity of a magnetically [Tiesinga et al., 1992] or optically [Fedichev et al., 1996a] induced Feshbach resonance [Inouye et al., 1998, Roberts et al., 2000], resulting in a reduced mean free path. However, it is theoretically predicted for the case that the scattering length exceeds the range of the interaction potential that the three-body recombination rate constant is increased proportionally to a^4 [Fedichev et al., 1996b, Bedaque et al., 2000]. Here, experimental investigation for the case of ^{87}Rb is required. For Na and ^{85}Rb large interactions in the vicinity of a Feshbach resonance have been realized and short life times of the condensate close to the resonance has been experimentally observed [Stenger et al., 1999a, Cornish et al., 2000]. For these experiments, the role of collisional cascades induced by three-body recombination products or by a potential Oort cloud is at the present not clarified.

Bibliography

G. Abbas, S. Yang, V. W. S. Chan, and J. G. Fujimoto. Injection behavior and modelling of 100 mW broad area diaode lasers. *IEEE Journal of Quantum Electronics*, 24(4):609, 1998.

C. S. Adams and E. Riis. Laser cooling and trapping of neutral atoms. *Rrogress in Quantum Electronics*, 21:1–79, 1997.

M. H. Anderson, J. R. Ensher, M. R. Matthews, C. E. Wieman, and E. A. Cornell. Observation of Bose-Einstein condensation in a dilute atomic vapor. *Science*, 269(0): 198, July 1995.

M. H. Anderson, W. Petrich, J. R. Enscher, and E. A. Cornell. Reduction of light-assisted collisional loss rate from a low-pressure vapor cell trap. *Physical Review A*, 50:R3597, 1994.

M. R. Andrews, D. M. Kurn, H.-J. Miesner, D. S. Durfee, C. G. Townsend, S. Inouye, and W. Ketterle. Propagation of sound in a Bose-Einstein condensate. *Phys. Rev. Lett.*, 79(4):553, July 1997a. *ibid.* **80**, 2967 (1998).

M. R. Andrews, M. O. Mewes, N. J. van Druiten, D. S. Durfee, D. M. Kurn, and W. Ketterle. Direct, non-destructive observation of a Bose condensate. *Science*, 84:273, July 1996.

M. R. Andrews, C. G. Townsend, H.-J. Miesner, D. S. Durfee, D. M. Kurn, and W. Ketterle. Observation of interference between two Bose-Einstein condensates. *Science*, 275 (0):637, Jan. 1997b.

E. Arimondo, M. Inguscio, and P. Violino. Experimental determinations of the hyperfine structure in the alkai atoms. *Reviews of Modern Physics*, 49:31–75, 1977.

A. Aspect. Thanks for private communication, 2000.

V. Bagnato, D. E. Pritchard, and D. Kleppner. Bose-Einstein condensation in an external potential. *Physical Review A*, 35:4354, 1987.

S. Bali, K. M. O'Hara, M. E. Gehm, S. R. Granade, and J. E. Thomas. Quantum-diffractive background gas collisions in atom-trap heating and loss. *Phys. Rev. A*, 60 (1):R29, July 1999.

P. F. Bedaque, E. Braaten, and H.-W. Hammer. Three-body rcombination in bose-gases with large scattering length. *Physical Review Letters*, 85:908, 2000.

T. Bergeman, G. Erez, and H. J. Metcalf. Magnetostatic trapping fields for neutral atoms. *Physical Review A*, 35(4):35, 1987.

P. Berthoud, A. Joyet, G. Dudle, N. Sagna, and P. Thomann. A continuous beam of slow, cold cesium atoms magnetically extracted from a 2d magneto-opical trap. *Eurphysics Letters*, 41:141, 1998.

G. C. Bjorklund, M. D. Levenson, W. Lenth, and C. Oritz. Frequency modulation (FM) spectroscopy. *Applied Physics B*, 32:145–152, 1983.

I. Bloch, T. W. Hänsch, and T. Esslinger. Measurement of the spatial coherence of trapped Bose gas at the phase transition. *Nature*, 403:166, 2000.

H. M. J. M. Boesten, C. Tsai, J. R. Gardner, D. J. Heinzen, and B. J. Verhaar. Observation of a shape resonance in the collision of two cold ^{87}Rb atoms. *Physical Review A*, 55:636, 1997.

N. Bogoliubov. On the theory of superfluidity. *Journal of Physics*, 11(1):23, 1947.

S. N. Bose. Plancks Gesetz und Lichtquantenhypothese. *Zeitschrift für Physik*, 26:178, 1924.

J. P. Bouyer. Spectral stabilization of an InGaAsP laser by injection-locking. *Annales de Physique*, 18(2):89–240, April 1993.

C. C. Bradley, C. A. Sackett, and R. G. Hulet. Bose-Einstein condensation of lithium: Observation of limited condensate number. *Phys. Rev. Lett.*, 78(6):985, Feb. 1997.

C. C. Bradley, C. A. Sackett, J. J. Tollett, and R. G. Hulet. Evidence of Bose-Einstein condensation in an atomic gas with attractive interactions. *Phys. Rev. Lett.*, 75(9): 1687, Aug. 1995. *ibid.* ***79***, 1170 (1997).

G. Breit and I. I. Rabi. Measurement of nuclear spin. *Physical Review*, 38:2082, 1931.

S. Burger, K. Bongs, S. Dettmer, W. Ertmer, and K. Sengstock. Dark solitons in Bose-Einstein condensates. *Phys. Rev. Lett.*, 83(25):5198, Dec. 1999.

J. P. Burke, Jr., J. L. Bohn, B. D. Esry, and C. H. Greene. Prospects for mixed-isotope Bose-Einstein condensates in rubidium. *Phys. Rev. Lett.*, 80(10):2097, Mar. 1998.

E. A. Burt, R. W. Christ, C. J. Myatt, M. J. Holland, E. A. Cornell, and C. E. Wieman. Coherence, correlations, and collisions: What one learns about Bose-Einstein condensates from their decay. *Physical Review Letters*, 79:337, 1997.

Y. Castin and R. Dum. Bose-Einstein condensation in time dependent traps. *Physical Review Letters*, 77(27):5315, 1996.

S. Chu. The manipulation of neutral particles. *Review of Modern Physics*, 70:685, 1998.

R. A. Cline, D. A. Smith, T. J. Greytak, and D. Kleppner. Magnetic confinement of spin-polarized atomic hydrogen. *Phys. Rev. Lett.*, 45(26):2117, Dec. 1980.

C. N. Cohen-Tannoudji. Manipulating atoms with photons. *Review of Modern Physics*, 70:707, 1998.

C. J. Cooper, G. Hillenbrand, J. Rink, and C. G. Townsend. The temperature of atoms in a magneto-optical trap. *Europhysics Letters*, 28:397, 1994.

E. A. Cornell, J. R. Ensher, and C. E. Wieman. Experiments in dilute atomic Bose-Einstein condensates. In M. Inguscio, S. Stringari, and C. E. Wieman, editors, *Bose-Einstein Condensation in Atomic Gases*, Proceedings of the International School of Physics 'Enrico Fermi', Course CXL. IOS Press Ohmsha, 1999.

S. L. Cornish, N. R. Claussen, J. L. Roberts, E. A. Cornell, and C. E. Wieman. Stable ^{85}Rb Bose-Einstein condensates with widely tunable interactions. *Phys. Rev. Lett.*, 85 (9):1795, Aug. 2000.

F. Dalfovo, S. Giorgini, L. P. Pitaevskii, and S. Stringari. Theory of Bose-Einstein condensation in trapped gases. *Rev. Mod. Phys.*, 71(3):463, Apr. 1999.

J. Dalibard and C. C. Cohen-Tannoudji. Laser cooling below the Doppler limit by polarization gradients: Simple theoretical models. *Journal of the Optical Society of America B*, 6:2023, 1998.

K. B. Davis, M.-O. Mewes, M. R. Andrews, N. J. van Druten, D. S. Durfee, D. M. Kurn, and W. Ketterle. Bose-Einstein condensation in a gas of sodium atoms. *Physical Review Letters*, 75:3969, 1995.

A. C. F. den Boer, H. C. W. Beijerinck, and K. A. H. van Leeuwen. High-power broad-area diode lasers for laser cooling. *Applied Physics B*, 64:415, 1997.

B. Desruelle, V. Boyer, P. Boyer, G. Birkl, M. Lecrivian, F. Alves, C. I. Westbrook, and A. Aspect. Trapping cold neutral atoms with iron-core electromagnet. *European Physical Journal D*, 1:255, 1998.

B. Desruelle, V. Boyer, S. G. Murdoch, G. Delannoy, P. Bouyer, and A. Aspect. Interrupted evaporative cooling of ^{87}Rb atoms trapped in a high magnetic field. *Physical Review A*, 60(3):R1759, 1999.

K. Dieckmann, R. J. C. Spreeuw, M. Weidemüller, and J. T. M. Walraven. Two-dimensional magneto-optical trap as a source of slow atoms. *Physical Review A*, 58 (5):3891, November 1998.

R. W. P. Drever, J. L. Hall, F. V. Kowalski, J. Hough, G. M. Ford, A. J. Munley, and H. Ward. Laser phase and frequency stabilization using an optical resonator. *Applied Physics B*, 31:97–105, 1983.

M. Edwards. The BEC homepage at Georgia Southern University. http://amo.phy.-gasou.edu.bec.html/.

A. Einstein. Quantentheorie des einatomigen idealen Gases: Zweite Abhandlung. *Sitzungber. Preuss. Akad. Wiss.*, 1925(0):3, Jan. 1925.

J. R. Ensher, D. S. Jin, M. R. Matthews, C. E. Wieman, and E. A. Cornell. Bose-Einstein condensation in a dilute gas: Measurement of energy and ground-state occupation. *Phys. Rev. Lett.*, 77(25):4984, Dec. 1996.

T. Esslinger, I. Bloch, and T. W. Hänsch. Bose-Einstein condensation in a quadrupole-Ioffe-configuration trap. *Phys. Rev. A*, 58(4):R2664, Oct. 1998.

R. D. Etters, J. V. Dugan, Jr., and R. Palmer. The ground state properties of spin-alinged atomic hydrogen, deuterium, and tritium. *Review of Modern Physics*, 62(2): 313, Jan 1975.

P. O. Fedichev, Y. Kagan, G. V. Shlyapnikov, and J. T. M. Walraven. Influence of nearly resonant light on the scattering length in low-temperature atomic gases. *Phys. Rev. Lett.*, 77(14):2913, Sept. 1996a.

P. O. Fedichev, M. W. Reynolds, and G. V. Shlyapnikov. Three-body recombination of ultracold atoms to a weakly bound s level. *Phys. Rev. Lett.*, 77(14):2921, Sept. 1996b.

P. O. Fedichev, G. V. Shlyapnikov, and J. T. M. Walraven. Damping of low-energy excitations of a trapped Bose-Einstein condensate at finite temperatures. *Phys. Rev. Lett.*, 80(11):2269, Mar. 1998.

C. W. Gardiner, M. D. Lee, R. J. Ballagh, M. J. Davis, and P. Zoller. Quantum kinetic theory of condensate growth: Comparison of experiment and theory. *Phys. Rev. Lett.*, 81(24):5266, Dec. 1998.

C. Garrec. Stabilization of diode lasers used for a two-dimensional magneto-optical trap. Master's thesis, Van der Waals-Zeeman Institute, University of Amsterdam, 1996.

E. Gehring, B. Beyer, K. J. Boller, and R. Wallenstein. Experimental characterization and numerical modelling of an AlGaAs oscillator broad area double pass amplifier system. *Applied Physics B*, 66:287, 1998.

K. E. Gibble, S. Kasapi, and S. Chu. Improved magneto-optical trapping in a vapor. *Optics Letters*, 17:526, 1992.

S. Giorgini, L. P. Pitaevskii, and S. Stringari. Condensate fraction and critical temperature of a trapped interacting Bose gas. *Phys. Rev. A*, 54(6):R4633, Dec. 1996.

L. Goldberg, D. Mehuys, M. R. Surette, and D. C. Hall. High-power, near-diffraction-limited large-area traveling-wave semiconductor amplifiers. *IEEE Journal of Quantum Electronics*, 29(6):2028, 1993.

V. V. Goldman and I. F. Silvera. Atomic hydrogen in an inhomogeneous magnetic field: Density profile and bose-einstein condensation. *Physical Review B*, 24(5):2870, 1981.

H. Hess, G. P. Kochansky, J. M. Doyle, N. Masuhara, D. Kleppner, and T. J. Greytak. Magnetic trapping of spin-polarized atomic hydrogen. *Physical Review Letters*, 59(6): 672, 1987.

H. F. Hess. Evaporative cooling of magnetically trapped and compressed spin-polarized hydrogen. *Phys. Rev. B*, 34(5):3476, Sept. 1986.

K. Huang. *Statistical Mechanics*. Jhon Whiley & Sons, 1963.

D. A. Huse and E. D. Siggia. The density distribution of a weakly interacting Bose gas in an external potential. *Journal of Low Temperature Physics*, 46:137, 1982.

S. Inouye, M. R. Andrews, J. Stenger, H.-J. Miesner, D. M. Stamper-Kurn, and W. Ketterle. Observation of Feshbach resonances in a Bose-Einstein condensate. *Nature*, 392 (0):151, Mar. 1998.

S. Inouye, A. P. Chikkatur, D. M. Stamper-Kurn, J. Stenger, D. E. Pritchard, and W. Ketterle. Superradiant Rayleigh scattering from a Bose-Einstein condensate. *Science*, 285:571, July 1999a.

S. Inouye, T. Pfau, S. Gupta, A. P. Chikkatur, A. Görlitz, D. E. Pritchard, and W. Ketterle. Phase-coherent amplification of atomic matter waves. *Nature*, 402:641, Dec. 1999b.

D. S. Jin, J. R. Ensher, M. R. Matthews, C. E. Wieman, and E. A. Cornell. Collective excitations of a Bose-Einstein condensate in a dilute gas. *Phys. Rev. Lett.*, 77(3):420, July 1996.

D. S. Jin, M. R. Matthews, J. R. Ensher, C. E. Wieman, and E. A. Cornell. Temperature-dependent damping and frequency shifts in collective excitations of a dilute Bose-Einstein condensate. *Phys. Rev. Lett.*, 78(5):764, Feb. 1997.

P. Julienne and J. Vigué. Cold collisions of ground- and excited-state alkali-metal atoms. *Physical Review A*, 44:4464, 1991.

P. S. Julienne, F. H. Mies, E. Tiesinga, and C. J. Williams. Collisional stability of double Bose condensates. *Phys. Rev. Lett.*, 78(10):1880, Mar. 1997.

Y. Kagan, E. L. Surkov, and G. V. Shlyapnikov. Evolution of a Bose-condensed gas under variations of the confining potential. *Phys. Rev. A*, 54(3):R1753, Sept. 1996.

Y. Kagan, B. V. Svistunov, and G. V. Shlyapnikov. Effect of Bose condensation on inelastic processes in gases. *Sov. Phys. JETP Lett.*, 42(4):209, Aug. 1985.

W. Ketterle, D. S. Durfee, and D. M. Stamper-Kurn. Making probing and understanding Bose-Einstein condensates. In M. Inguscio, S. Stringari, and C. E. Wieman, editors, *Bose-Einstein Condensation in Atomic Gases*, Proceedings of the International School of Physics 'Enrico Fermi', Course CXL. IOS Press Ohmsha, 1999.

W. Ketterle and N. J. van Druten. Evaporative cooling of trapped atoms. *Advances in Atomic, Molecular, and Optical Physics*, 37:181, 1996.

K. Lindquist, M. Stephens, and C. Wieman. Experimental and theoretical study of the vapor-cell zeeman optical trap. *Physical Review A*, 46:4082, 1992.

Z. T. Lu, K. L. Corwin, M. J. Renn, M. H. Anderson, E. A. Cornell, and C. E. Wieman. Low-velocity intense source of atoms from a magneto-optical trap. *Physical Review Letters*, 77:3331, 1996.

O. J. Luiten. *Lyman-α Spectroscopy of Magnetically Trapped Atomic Hydrogen.* PhD thesis, University of Amsterdam, 1993.

O. J. Luiten, M. W. Reynolds, and J. T. M. Walraven. Kinetic theory of the evaporative cooling of a trapped gas. *Physical Review A*, 53(1):381, 1996.

K. W. Madison, F. Chevy, W. Wohlleben, and J. Dalibard. Vortex formation in a stirred Bose-Einstein condensate. *Phys. Rev. Lett.*, 84(5):806, Jan. 2000.

M. R. Matthews, B. P. Anderson, P. C. Haljan, D. S. Hall, C. E. Wieman, and E. A. Cornell. Vortices in a Bose-Einstein condensate. *Phys. Rev. Lett.*, 83(13):2498, Sept. 1999.

M. O. Mewes, M. R. Andrews, N. J. van Druiten, D. M. Kurn, D. S. Durfee, and W. Ketterle. Bose-Einstein condensation in a tightly confining dc magnetic trap. *Physical Review Letters*, 77(3):416, 1996a.

M.-O. Mewes, M. R. Andrews, N. J. van Druten, D. M. Kurn, D. S. Durfee, C. G. Townsend, and W. Ketterle. Collective excitations of a Bose-Einstein condensate in a magnetic trap. *Phys. Rev. Lett.*, 77(6):988, Aug. 1996b.

H.-J. Miesner, D. M. Stamper-Kurn, M. R. Andrews, D. S. Durfee, S. Inouye, and W. Ketterle. Bosonic stimulation in the formation of a Bose-Einstein condensate. *Science*, 279(0):1005, Feb. 1998.

A. L. Migdall, J. V. Prodan, W. D. Phillips, T. H. Bergeman, and H. J. Metcalf. First observation of magnetically trapped neutral atoms. *Physical Review Letters*, 54:2596, 1985.

C. Myatt. *Bose-Einstein Condensation Experiments in a Dilute Vapor of Rubidium.* PhD thesis, University of Colorado, Boulder, Colorado, 1997.

C. J. Myatt, E. A. Burt, R. W. Ghrist, E. A. Cornell, and C. E. Wieman. Production of two overlapping Bose-Einstein condensates by sympathetic cooling. *Phys. Rev. Lett.*, 78(4):586, Jan. 1997.

J. Nellessen, J. Werner, and W. Ertmer. Magneto-optical compression of a monoenergetic sodium atomic beam. *Opics Communications*, 78:300, 1990.

J. H. Oort. The structure of the cloud of comets surrounding the solar system, and a hypothesis concerning its origin. *Bulletin of the Atronimical Institutes of The Netherlands*, XI(408):91, 1950.

W. Petrich, M. H. Anderson, J. R. Ensher, and E. A. Cornell. Stable, tightly confining magnetic trap for evaporative cooling of neutral atoms. *Physical Review Letters*, 74: 3352, 1995.

W. D. Phillips. Laser cooling and trapping of neutral atoms. *Rev. Mod. Phys.*, 70(3): 721, July 1998.

W. D. Phillips and H. Metcalf. Laser deceleration of an atomic beam. *Physical Review Letters*, 48:596, 1982.

P. Pinkse, A. Mosk, M. Weidemüller, M. W. Reynolds, T. W. Hijmans, and J. T. M. Walraven. Adiabatically changing the phase-space density of a trapped Bose gas. *Physical Review Letters*, 78(6):990, 1997.

P. W. H. Pinkse, A. Mosk, M. Weidemüller, M. W. Reynolds, T. W. Hijmans, and J. T. M. Walraven. One-dimensional evaporative cooling of magnetically trapped atomic hydrogen. *Physical Review A*, 57(6):4747, 1998.

M. Praeger, V. Vuletic, T. Fischer, T. W. Hänsch, and C. Zimmermann. A broad emitter diode laser system for lithium spectroscopy. *Applied Physics B*, 67:163, 1998.

D. E. Pritchard. Cooling atoms in a magnetic trap for precision spectroscopy. *Physical Review Letters*, 51:1336, 1983.

A. Radzig and B. M. Smirnov. *Reference Data of Atoms, Molecules, and Ions.* Springer Verlag, Berlin, 1985.

C. Raman, M. Köhl, R. Onofrio, D. S. Durfee, C. E. Kucklewicz, Z. Hadzibabic, and W. Ketterle. Evidence for a critical velocity in a Bose-Einstein condensed gas. *Physical Review Letters*, 83:2502, 1999.

N. F. Ramsey. *Molecular Beams.* Oxford University Press, 1956.

J. Reichel, W. Hänsel, and T. W. Hänsch. Atomic micromanipulation with magnetic surface traps. *Physical Review Letters*, 83:3398, 1999.

L. Ricci, M. Weidemüller, T. Esslinger, A. Hemmerich, C. Zimmermann, V. Vuletic, W. König, and T. W. Hänsch. A compact grating-stabilized diode laser system for atomic physics. *Optics Communications*, 117:541, 1995.

E. Riis, D. S. Weiss, K. A. Moler, and S. Chu. Atom funnel for the production of a slow, high-density atomic beam. *Physical Review Letters*, 64:1658, 1990.

J. L. Roberts, N. R. Claussen, J. P. Burke, Jr., C. H. Greene, E. A. Cornell, and C. E. Wieman. Resonant magnetic field control of elastic scattering of cold ^{85}Rb. *Phys. Rev. Lett.*, 81(23):5109, Dec. 1998.

J. L. Roberts, N. R. Claussen, S. L. Cornish, and C. E. Wieman. Magnetic field dependence of ultracold inelastic collisions near a Feshbach resonance. *Phys. Rev. Lett.*, 85 (4):728, July 2000.

A. Roth. *Vacuum Technology*, chapter 4., page 158. Elsevier Science Publishers, 1990.

J. R. Rubbmark, M. M. Kash, M. G. Littman, and D. Kleppner. Dynamical effects at avoided level crossing: A study of the Landau-Zener effect using rydberg atoms. *Physical Review A*, 23(6):3107, 1981.

A. Scholz, M. Christ, D. Doll, J. Ludwig, and W. Ertmer. Magneto-optical preparation of a slow, cold and bright Ne* atomic beam. *Optics Communications*, 111:155, 1994.

J. Schuster, A. Marte, S. Amtage, B. Sang, and G. Rempe. Critical collisional opacity in a bose-einstein condensate. *preprint*, 2000.

I. Shvarchuck, K. Dieckmann, M. Zielonkowski, and J. T. M. Walraven. Broad-area diode laser system for a rubidium Bose-Einstein condensation experiment. *Applied Physics B*, 71(4):475–480, 2000.

I. F. Silvera and J. T. M. Walraven. Stabilization of atomic hydrogen at low temperature. *Phys. Rev. Lett.*, 44(3):164, Jan. 1980.

J. Söding, D. Guéry-Odelin, P. Desibiolles, H. Inamori, and J. Dalibard. Three-body decay of a rubidium Bose-Einstein condensate. *Applied physics B*, 69:257, 1999.

D. M. Stamper-Kurn, M. R. Andrews, A. P. Chikkatur, S. Inouye, H.-J. Miesner, J. Stenger, and W. Ketterle. Optical confinement of a Bose-Einstein condensate. *Physical Review Letters*, 80:2027, 1998a.

D. M. Stamper-Kurn, H.-J. Miesner, S. Inouye, M. R. Andrews, and W. Ketterle. Collisionless and hydrodynamic excitations of a Bose-Einstein condensate. *Phys. Rev. Lett.*, 81(3):500, July 1998b.

A. M. Steane, M. Chowdhury, and C. J. Foot. Radiation force in the magneto-optical trap. *Journal of the Optical Society of America B*, 9:2142, 1992.

J. Stenger, S. Inouye, M. R. Andrews, H.-J. Miesner, D. M. Stamper-Kurn, and W. Ketterle. Strongly enhanced inelastic collisions in a Bose-Einstein condensate near Feshbach resonances. *Phys. Rev. Lett.*, 82(12):2422, Mar. 1999a.

J. Stenger, S. Inouye, A. P. Chikkatur, D. M. Stamper-Kurn, D. E. Pritchard, and W. Ketterle. Bragg spectroscopy of a Bose-Einstein condensate. *Phys. Rev. Lett.*, 82 (23):4569, June 1999b.

D. Suter. *The Physics of Laser-Atom Interactions*, chapter 6.4., pages 230–237. Cambrige University Press, 1997.

E. Tiesinga, A. Moerdijk, B. J. Verhaar, and H. T. C. Stoof. Conditions for Bose-Einstein condensation in magnetically trapped atomic cesium. *Phys. Rev. A*, 46(3):R1167, Aug. 1992.

P. Valkering. Optimization of evaporative cooling of rubidium atoms in a magnetic trap. Master's thesis, University of Utrecht, February 1999.

R. van Roijen, J. J. Berkhout, S. Jaakkola, and J. Walraven. Experiments with atomic hydrogen in a magnetic trapping field. *Physical Review Letters*, 61:931, 1988.

J. Vanier and C. Audoin. *The Quantum Physics of Atomic Frequency Standards*, volume 1. Adam Hilger, Bristol and Philadelphia, 1988.

B. J. Verhaar. Thanks for private communication, 2000.

N. V. Vitanov and K. A. Suominen. Time-dependent control of ultra-cold atoms in magnetic traps. *Physical Review A*, 56(6):R4377, 1997.

E. J. D. Vredenbregt, K. A. H. van Leeuwen, and H. C. W. Beijerinck. Booster for ultra-fast loading of atom traps. *Optics Communications*, 147:375, 1998.

J. T. M. Walraven. Atomic hydrogen in magnetostatic traps. In G. L. Oppo, S. M. Barnett, E. Riis, and M. Wilkinson, editors, *Quantum Dynamics of Simple Systems*, volume 44 of *SUSSP Proceedings*. IOP, Bristol, 1996.

S. Weyers, E. Aucouturier, C. Valentin, and N. Dimarcq. A continuous beam of cold cesium atoms extracted from a two-dimensional magneto-optical trap. *Optics Communications*, 143:30, 1997.

C. E. Wieman and L. Hollberg. Using diode lasers for atomic physics. *Review of Scientific Instruments*, 62(1):1–20, January 1991.

W. H. Wing. Some problems and possibilities for quasistatic neutral particle trapping. In W. D. Phillips, editor, *Proceedings of the Workshop on Spectroscopic Applications of Slow Atomic Beams*, volume 653. NBS, Gaithersburg, April 1983.

C. Zener. Non-adiabatic crossing of energy levels. *Proceedings of the Royal Society of London Series A*, 137:696, 1932.

Summary

This thesis deals with the quantum gas phase of atomic rubidium. The work involves the development of the experimental apparatus to reach the quantum degenerate regime and a first series of experiments with the rubidium quantum gas, including the attainment of Bose-Einstein condensation. Bose-Einstein condensation was predicted in 1925 [Bose, 1924, Einstein, 1925], at the time when quantum mechanics was being developed. Seven decades later in 1995 Bose-Einstein condensation (BEC) in dilute atomic gases was first observed. Within a few months BEC was observed with the alkali atoms rubidium [Anderson et al., 1995] and sodium [Davis et al., 1995]. Lithium [Bradley et al., 1995, 1997] followed rapidly. This development became possible after magneto-optical trapping and laser cooling of alkali atoms to ultra-low temperatures were realized. For the discovery and explanation of sub-Doppler laser cooling the Nobel prize was given in 1997 [Chu, 1998, Cohen-Tannoudji, 1998, Phillips, 1998]. In the above mentioned experiments Bose-Einstein condensation was achieved after transfer of the optically precooled gas sample into a magnetic trap and application of evaporative cooling. This exciting achievement attracted a lot of attention in the scientific community and the mass media alike, in which Bose-Einstein condensation was referred to as a 'new state of matter'. The first achievements of BEC led to an enormous boost of activity and were followed to the present date by at least 24 successful BEC experiments world wide. The experimental progress is accompanied by extended theoretical work, which is leading to a deep understanding of the behaviour of Bose-condensed matter.

Dilute gases of neutral atoms can be studied at ultra-low temperature by confining them in a magnetic trap. Bose-Einstein condensation occurs when at high density and low temperature the thermal wavelength of the atoms becomes of the order of the interparticle separation between the atoms, and the atomic waves overlap. As the condensate forms, a macroscopic amount of atoms populate the ground state of the trap and share coherently the same wavefunction. The BEC transition temperature of dilute gases is typically slightly below $1\,\mu$K.

In this work emphasis is put on experiments with a large number of atoms. The availability of large numbers of cold atoms enables experiments with high density samples. From a practical point of view this allows fast thermalization and thus fast experimental procedures. From a theoretical point of view it allows the investigation of the cross-over

from the collisionless to the hydrodynamic behaviour in the rubidium quantum gas.

This thesis is divided into the following chapters: Following an introduction, Chapter 2 summarizes some theoretical principles and results are briefly to an extend as is needed for the description of the experiments. The atomic properties of rubidium, which are relevant for laser cooling and magnetic trapping are discussed. The principle of magnetic trapping is introduced, and the magnetic trapping configuration used in this thesis, which is of the Ioffe-Pritchard type [Pritchard, 1983], is explained. Bose-Einstein condensation of the trapped ideal gas is described followed by the main theoretical results for the case of repulsive interactions between the particles and large atom numbers. As of great importance for the achievement of Bose-Einstein condensation the principle of evaporative cooling is briefly introduced.

Chapter 3 describes the main components of the experimental apparatus. First, it gives an overview over the laser system consisting of 5 diode lasers and the purpose of the produced laser beams for the experiment. In order to load a large atom number into a magneto-optical trap an amount of laser power is required which exceeds the power of commonly used and commercially available diode lasers. In order to provide sufficient laser power a broad-area diode laser system, delivering 130 mW of usable laser power, was build and characterized for this experiment by [Shvarchuck et al., 2000]. For the work in this thesis the broad-area laser was integrated in the laser system and was for the first time applied in an experiment on laser cooling and trapping. Second, the vacuum system is described including a rubidium vapor cell for the realization of the atomic beam source and a UHV chamber where trapping and cooling of the gas cloud takes place. Next, a detailed portrait of the magnetic trap is given. In this work the design of the trap assembly was optimized to obtain high stability, flexibility in adjusting the trapping parameters, and a strong confinement of the gas. With a magnetic field gradient of 353 G/cm and a curvature of 286 G/cm^2 the steepest magnetic trap of this type was realized. This enables fast and efficient evaporative cooling yielding high atom numbers and densities at the BEC phase transition. Furthermore, the components for the rf-signal source used for evaporative cooling are specified. The chapter is ending with a description of the imaging system by which the properties of the cold gas clouds are measured.

Chapter 4 is based on the publication [Dieckmann et al., 1998] dealing with the intense atomic beam source developed in this experiment. The high atomic flux of the source, almost 10^{10} atoms/s at an average velocity of 10 m/s, is the basis of obtaining high atom numbers in a short time. The operation principle is based on the two-dimensional vapor cell magneto-optical (2D-MOT) trap. It is investigated how the atomic flux of a vapor cell based source can be optimized and an experimental comparison between different variations of the 2D-MOT geometry used as atomic beam sources has been performed. The highest achieved flux exceeds the atomic flux of existing vapor cell based atomic beam sources by almost two-orders of magnitude, for the same low laser power (50 mW) in use.

As described in Chapter 5 the atomic beam source is applied to load a magneto-optical trap with large atom number of 10^{10}. This is done with the goal to take benefit of the high beam flux and to achieve a high atom number after a short loading time. The measured atomic beam flux is compared to the measurements of the trap loading resulting

in a transfer efficiency of 70 %. For the first time it was demonstrated that the effective loading flux can be improved by avoiding loss from the atomic beam due a repulsive light force originating from fluorescence light from the magneto-optically trapped cloud. This is realized by optically pumping the atoms into a dark hyperfine state. After loading polarization gradient cooling is used to cool the cloud to a temperature of 40 μK. This temperature lies below the Doppler limit, which is 144 μK for rubidium. The chapter ends with a description of how the temperature of the atomic cloud after sub-doppler cooling was minimized for the case of a large atom number.

Chapter 6 explains how the atoms are loaded from the magneto-optical trap into the magnetic trap. Further, the steps for adiabatic compression of the sample in the trap are individually characterized in detail. After the compression the cloud is populated with 4×10^9 atoms at a temperature of 760 μK and a density of 7×10^{11} atoms/cm^3. The characterization of magnetic trapping is completed by the measurement of the life time of the atomic sample and the measurement of the harmonic frequencies of the trap. Measurement of the life time of the sample in the compressed magnetic trap gives information on whether efficient evaporative cooling is possible and BEC can be achieved. Measurement of the harmonic trap frequencies is essential for subsequent quantitative analysis of the trapped Bose-gas.

In the first part of Chapter 7 evaporative cooling in the runaway regime is described. The efficiency of the evaporation process with respect to the particle loss is evaluated. Evaporative cooling is usually completed within 10 s, but can also lead to Bose-Einstein condensation within 2 s with a 60 % reduction of the atom number. Second, the observation of Bose-Einstein condensation is presented including a description of the analysis methods used to obtain the cloud parameters from the absorption images. The phase transition is reached with 1.5×10^7 atomen at a temperature of 1.5 μK and a density of 7×10^{14} atoms/cm^3. As highest atom numbers are achieved, gas samples can be produced which are in the transition region between the collisionless and the hydrodynamic regimes. As the last part of this chapter a demonstration of the so called 'atom laser' is added, by which the phase coherence of the Bose-condensed atoms is shown.

Chapter 8 deals with the so called 'Oort cloud'. This is a cloud of rubidium atoms which populates the magnetic trap to energies of several mK. This is possible due to the large depth (12 mK) of the magnetic trap. It is demonstrated how for the first time clear evidence of an Oort cloud was obtained. A method for measuring the Oort cloud atom number is presented, and information on the energy distribution of the Oort cloud population is obtained. This method is based on the release of the atoms from the magnetic trap and recapture into a magneto-optical trap. In this experiment an Oort cloud population above an energy of 250 μK of up to 2.4×10^6 atoms with an averaged energy of 3 mK was found. It is investigated how atoms from the Oort cloud can lead to heating and losses from the cold cloud. To investigate these Oort cloud related phenomena cold clouds under conditions just above the BEC phase transition were used. Such clouds allow to study the essential phenomena and to trace the origin of the Oort cloud without the added complexity of the presence of a condensate. Further, it is investigated, how the effects of the Oort cloud on the cold cloud can be suppressed by means of rf-shielding. As the origin of the Oort cloud incomplete evaporation during evaporative cooling at high energies is identified. Therefore, it is possible to reduce

the Oort cloud population by a factor of 6 by applying a modified scheme of adiabatic compression and evaporative cooling. This enables to compare the effect of the Oort cloud on the cold cloud for large and reduced Oort cloud. A remarkable result is the observation of an increase of the cold cloud atom number accompanied by a decrease of the Oort cloud atom number which occurs only for the highest densities of the cold cloud. This is interpreted as capture of atoms from the Oort cloud into the cold cloud by a collisional cascade. Finally, the consequences of the observations on the non condensed samples for the possibilities of entering the hydrodynamic regime with a Bose-Einstein condensate are discussed.

Samenvatting

Dit proefschrift behandelt de quantumgasfase van atomair rubidium. Het werk omvat de ontwikkeling van de experimentele apparatuur voor het bereiken van het ontaarde quantumgebied en een eerste meetserie met rubidium quantumgas waar ondermeer Bose-Einstein-condensatie (BEC) werd bereikt. Bose-Einstein-condensatie werd in 1925 door S. N. Bose en A. Einstein voorspelt [Bose, 1924, Einstein, 1925], tijdens het ontstaan van de quantummechanica. Dit verschijnsel werd pas zeven decennia later in 1995 in verdunde atomaire gassen voor het eerst geobserveerd. Binnen en paar maanden slaagden experimenten met rubidium [Anderson et al., 1995] en natrium [Davis et al., 1995]. BEC in lithium [Bradley et al., 1995, 1997] volgde kort daarop. Deze ontwikkeling werd mogelijk door het realiseren van het magneto-optisch vangen en laser koelen van alkali atomen tot ultra-koude temperatuur. Voor het ontdekken en verklaren van sub-Doppler laser koelen werd in 1997 de Nobelprijs toegekend [Chu, 1998, Cohen-Tannoudji, 1998, Phillips, 1998]. In de bovengenoemde experimenten werd Bose-Einstein-condensatie bereikt door de met laserkoelen voorgekoelde gaswolk naar een magnetische val te transfereren en verdampingskoelen toe te passen. Deze opmerkelijke gebeurtenissen stimuleerden een grote aktiviteit in de experimentele en theoretische natuurkunde. Er ontstond een nieuw vakgebied, gericht op de verrassende eigenschappen van Bose-gecondenseerde materie, te rijk om deze hier uitputtend te noemen.

Verdunde atomaire gassen kunnen bij ultra lage temperaturen in een magnetisch val worden bestudeerd. Bose-Einstein-condensatie van het gas treedt op als bij hoge dichtheid en tegelijk lage temperatuur, de thermische golflengte van de atomen dezelfde orde van grote bereikt als de gemiddelde afstand tussen de atomen en dus de atomaire golven overlappen. Het Bose-condensaat formeert zich doordat een macroscopische fractie van de atomen de grondtoestand van de val bevolkt. Deze atomen delen daarbij op een coherente manier dezelfde golffunctie. De kritische temperatuur van de Bose-Einstein-faseovergang wordt met verdunde gassen typisch bij 1 μK bereikt.

In het werk voor dit proefschrift worden experimenten met een groot aantal atomen benadrukt. De beschikbaarheid van grote aantallen atomen maakt experimenten met een hoge dichtheid van de gaswolk mogelijk. Uit praktisch oogpunt laat dit snelle thermalisatie en snelle experimentele procedures toe. Uit theoretisch oogpunt verleent het toegang tot het overgangsgebied tussen botsingvrij en hydrodynamisch gedrag van het

gas.

Het proefschrift heeft de volgende indeling: Hoofdstuk 2 is een samenvatting van de theoretische concepten nodig voor de beschrijving van de experimenten. De atomaire eigenschappen van rubidium die relevant zijn voor laser-koeling en de werking van de magnetische val worden besproken. Het principe van de magnetische val wordt geïntroduceerd en de Ioffe-Pritchard [Pritchard, 1983] configuratie van de magnetische val, zoals in dit werk gebruikt, wordt gekarakteriseerd. Bose-Einstein-condensatie van het ideale gas wordt geïntroduceerd gevolgd door de meest belangrijke theoretische resultaten voor het geval van onderling afstotende wisselwerking tussen de atomen en voor een groot aantal atomen. Het voor het bereiken van Bose-Einstein-condensatie zo belangrijke proces, verdampingskoeling, wordt kort bescheven.

Hoofdstuk 3 beschrijft de componenten van de experimentele apparatuur. Eerst wordt een overzicht gegeven van het lasersysteem, dat uit vijf diodelasers bestaat, en de toepassingen van de produceerde laserbundels. Om een groot aantal atomen in een magneto-optische val te vangen is een hoeveelheid laservermogen nodig, die boven de door commerciële, algemeen gebruikte, diodelasers geproduceerde hoeveelheid ligt. Om aan de eisen te voldoen werd voor dit experiment een 'broad area' diodelasersysteem opgebouwd en gekarakteriseerd [Shvarchuck et al., 2000], dat effectief 130 mW laservermogen ter beschikking stelt. Voor het werk van dit proefschrift werd de 'broad-area' laser in het gehele lasersysteem geïntegreerd en voor het eerst werd deze laser in een experiment toegepast om met laserlicht atomen te vangen en te koelen. In het vervolg wordt het vacuümsysteem beschreven, met onder meer een rubidium dampcel voor de realisatie van de atomaire bundel en een ultra-hoogvacuümcel waar het vangen en koelen van de gaswolk plaatsvindt. Daarop volgt een gedetailleerde beschrijving van de magnetische val. Voor dit werk wordt het ontwerp van de magnetische val en de houder geoptimaliseerd om hoge stabiliteit, flexibiliteit om de valparameters te kunnen instellen en om een sterke opsluiting te bereiken. Met een gradient van 353 G/cm en een kromming van 286 G/cm^2 werd de steilste magnetische val van een dergelijk type gerealiseerd. Dit maakt snel en efficiënt verdampingskoelen mogelijk, waardoor Bose-Einstein-condensatie met een groot aantal atomen bij hoge dichtheid wordt bereikt. Verder worden de componenten gespecificeerd, die voor het verdampingskoelen worden toegepast. Aan het eind van dit hoofdstuk wordt het afbeeldingsysteem beschreven, dat voor het meten van de eigenschappen van de koude wolk wordt toegepast.

Hoodstuk 4 is op de publicatie [Dieckmann et al., 1998] gebaseerd, die over de voor dit experiment ontwikkelde intense atomaire bundel gaat. De hoge atomaire stroom, bijna 10^{10} atomen/s met een gemiddelde snelheid van rond 10 m/s, van deze bron is de grondslag voor het bereiken van een hoog aantal atomen. Het principe van de bron is gebaseerd op de twee-dimensionale magneto-optische val in een dampcel (2D-MOT). Dit onderzoek bestudeert hoe de hoeveelheid stroming kan worden geoptimaliseerd. Verder werden er vergelijkende metingen voor verschillende variaties van de 2D-MOT gepresenteerd. De hoogste gerealiseerde atomaire stroming overschrijdt de stroming van op dampcellen gebaseerde bundels met twee orders van grote, die eerder werden gerealiseerd en dezelfde lage hoeveelheid laservermogen (50 mW) benutten.

Zoals in hoofdstuk 5 staat beschreven wordt de atomaire bron toegepast om een magneto-optische val met een hoog aantal van order 10^{10} atomen te laden. De gemeten

atomaire stroming wordt vergeleken met het laden van de val waaruit een efficiëntie van circa 70 % resulteert. Het werd voor het eerst aangetoond, dat de instroming in de val kan worden verbeterd door verlies uit het bundel, ten gevolg van uit de magneto-optische val afkomstig strooilicht, te voorkomen. Dit kan worden gedaan door optisch pompen van de atomen van het bundel naar een donkere hyperfijntoestand. Na de laadprocedure wordt met behulp van 'polarization gradient' koelen de temperatuur van het gas tot $40\,\mu$K verlaagd. Deze temperatuur ligt onder de Doppler-temperatuur, $144\,\mu$K in het geval van rubidium. Verder wordt in dit hoofdstuk beschreven hoe de temperatuur werd geminimaliseerd voor het geval van sub-Doppler koelen van een hoog aantal atomen.

In Hoofdstuk 6 wordt uitgelegd hoe de atomen van de magneto-optische val naar de magnetische val worden overgebracht. Daarna volgt een karakterisering van de adiabatische compressie van de atomen in de magnetische val met een gedetailleerd overzicht van de individuele stappen. Na de compressie bevinden zich 4×10^9 atomen in de wolk bij een temperatuur van $760\,\mu$K en bij een dichtheid van 7×10^{11} atomen/cm^3. De karakterisering van het magnetisch invangen wordt afgerond door metingen van de levensduur van de atomaire wolk en metingen van de valfrequenties. De meting van de levensduur in de gecomprimeerde magnetische val geeft informatie over de mogelijkheid om efficiënt verdampingskoelen toe te passen. De meting van de valfrequenties is noodzakelijk voor de kwantitatieve analyse van het opgesloten Bose-gas.

In het eerste deel van hoofdstuk 7 wordt het verdampingskoelen onder 'runaway' condities beschreven. De efficiëntie van het koelproces ten opzichte van het deeltjesverlies word gemeten en geanalyseerd. De verdampingskoeling wordt meestal binnen 10 s beëindigt, maar kan ook al na 2 s tot Bose-Einstein-condensatie leiden met een om 60 % gereduceerde aantal atomen. Daarna wordt de observatie van Bose-Einstein-condensatie gepresenteerd, wat een beschrijving van de analysemethodes van de absorptiebeelden van de wolk inhoudt. De faseovergang werd met 1.5×10^7 atomen bij een temperatuur van $1.5\,\mu$K en een dichtheid van 7×10^{14} atomen/cm^3 overschreden. Met het bereiken van de hoogste aantal deeltjes wordt het overgangsgebied tussen botsingvrij en hydrodynamisch gedrag van het gas bereikt. In het eind van dit hoofdstuk is er een demonstratie van de zogenoemde 'atoomlaser' toegevoegd waardoor de coherentie van de atomen in het Bose-condensaat wordt aangetoond.

Hoofdstuk 8 behandelt de zogenoemde 'Oort-wolk'. Dit is een wolk van rubidium atomen, die de magnetische val bij hoge energieën van enkele mK bevolkt. Dit wordt door de grote diepte (12 mK) van de magnetische val mogelijk gemaakt. Hier wordt gedemonstreerd hoe voor het eerst een duidelijk bewijs voor het bestaan van een dergelijke Oort-wolk wordt verkregen. Verder wordt er een methode gepresenteerd om het aantal atomen van de Oort-wolk te meten en informatie over de energieverdeling te krijgen. Deze methode is gebaseerd op het vrijlaten van de atomen uit de magnetische val en het opnieuw invangen in een magneto-optische val. In dit experiment werden tot 2.4×10^6 atomen boven een energie van $250\,\mu$K bij een gemiddelde energie van rond 3 mK gevonden. Er wordt bestudeerd hoe de deeltjes uit de Oort-wolk tot verwarming van, en verlies van deeltjes uit de koude wolk leiden. Daarvoor worden gaswolken vlak boven de condensatiepunt gebruikt, om voor het condensaat typische verwarmings- en verliesprocessen te omzeilen. Verder wordt bestudeerd hoe een scherm van radiofrequente straling, effecten van de Oort-wolk op de koude wolk kan voorkomen. Als de oorsprong van de grootste

fractie van de Oort-wolk wordt onvoltooide verdamping geïdentificeerd. Daarna is het mogelijk het aantal atomen in de Oort-wolk door een veranderd koelschema met een factor 6 te reduceren. Daardoor kan het effect van de Oort-wolk op de koude wolk voor lage en hoge bevolking van de Oort-wolk worden bestudeerd. Een opmerkelijk resultaat is de observatie van een toename van het aantal atomen in de koude wolk bij aanwezigheid van een afnemende aantal atomen in de Oort-wolk, die alleen bij de hoogste dichtheid optreed. Dit wordt geïnterpreteerd als invang van deeltjes door een cascade van botsingen. Tenslotte worden de consequenties van deze gemaakte observaties voor het bereiken van het hydrodynamisch gebied met een Bose-condensaat bediscussieerd.

Zusammenfassung

Diese Arbeit handelt von der Quanten-gasphase atomaren Rubidiums. Sie beinhaltet die Entwicklung und den Aufbau einer experimentellen Apparatur um das Quantenregime zu erreichen, sowie eine erste Serie von Experimenten mit Rubidium Quanten-gas, das Erreichen von Bose-Einstein Kondensation eingeschlossen. Bose-Einstein Kondensation wurde im Jahre 1925 [Bose, 1924, Einstein, 1925] vorhergesagt, zu einer Zeit, als die Quantenmechanik entstand. Siebzig Jahre später, im Jahr 1995, wurde Bose-Einstein Kondensation (BEC) in verdünnten atomaren Gasen zum ersten mal beobachtet. Dies geschah binnen weniger Monate mit den Alkalitomen Rubidium [Anderson et al., 1995] und Natrium [Davis et al., 1995], kurz darauf gefolgt durch Lithium [Bradley et al., 1995, 1997]. Diese Entwicklung wurde möglich nachdem magneto-optisches Speichern und Laserkühlen von Alkaliatomen mit Laserlicht realisiert worden war. Für die Entdeckung und Erlärung des sub-Doppler Laserkühlens wurde in 1997 der Nobelpreis vergeben [Chu, 1998, Cohen-Tannoudji, 1998, Phillips, 1998]. In den obengenannten Experimenten wurde Bose-Einstein Kondensation durch den Transfer des mit Lasern vorgekühlten Gases in eine Magnetfalle und die Anwendung von Verdampfungskühlen erreicht. Dieser bemerkenswerten, rasanten Entwicklung wurde große Aufmerksamkeit in der Wissenschaft und auch in den Medien zuteil, wo Bose-Einstein Kondensation als ein neuer "Zustand der Materie" bezeichnet wurde. Es entstand ein neues, schnell wachsendes Fachgebiet, das auf die Eigenschaften von Bose-Einstein kondensierter Materie gerichtet ist. Die bisherigen Resultate sind zu vielfältig um sie hier zu nennen.

Studien an verdünnten atomaren Gasen bei ultra-tiefen Temperaturen können durch Einschluß des Gases in eine Magnetische Falle durchgeführt werden. Bose-Einstein Kondensation tritt dann auf, wenn beim Übergang zu hohen Dichten und tiefen Temperaturen die thermische Wellenlänge genauso groß wird wie der gemittelte Abstand zwischen den Atomen, und die atomaren Wellenfunktionen zu überlappen beginnen. Mit der Bildung des Kondensates bevölkert ein makroskopischer Anteil der Atome den Grundzustand der Falle und teilt dieselbe Grundzustandswellenfunktion in kohärenter Weise. Für verdünnte Gase wird die Überganstemperatur für Bose-Einstein Kondensation typischerweise etwas unterhalb von $1\,\mu$K erreicht.

In dieser Arbeit wird ein Schwerpunkt auf Experimente mit hohen Teilchenzahlen gelegt. Die Verfügbarkeit von hohen Teilchenzahlen ermöglicht Experimente bei ho-

hen Dichten. Von einem praktischen Standpunkt aus betrachtet ermöglicht das ein schnelles Thermalisieren wärend des Kühlvorganges und deshalb schnelle experimentelle Prozesse. Von einem theoretischem Standpunkt aus betrachtet werden Studien des Rubidium Quantengases im Übergangsbereich vom stoßfreien zum hydrodynamischen Limit erreichbar.

Diese Doktorarbeit ist in die folgenden Kapitel eingeteilt: Nach der Einleitung werden in Kapitel 2 einige theoretische Grundlagen und Resultate soweit eingeführt und zusammengefaßt, wie das zur Beschreibung der Experimente notwendig ist. Es werden die für die Laser-Kühlung und magnetisches Speichern relevanten atomaren Eigenschaften diskutiert. Das Prinzip des magnetischen Speicherns wird eingeführt und die Ioffe-Pritchard Magnetfallenkonfiguration [Pritchard, 1983], die hier zur Anwendung kommt, wird erklärt. Eine kurze Einführung der Bose-Einstein Kondensation des idealen Gases wird gefolgt durch die wichtigsten theoretischen Resultate für den Fall abstoßender Wechselwirkung zwischen den Atomen und hoher Teilchenzahl. Schließlich wird das für das Erreichen der Bose-Einstein Kondensation so wichtige Prinzip des Vedampfugnskühlens beschrieben.

Kapitel 3 beschreibt die Hauptkomponenten der experimentellen Apparatur. Zunächst wird ein Überblick über das aus fünf Lasern bestehende Diodenlasersystem mit einer Auflistung der erzeugten Laserstrahlen und deren Anwendungen innerhalb des Experimentes gegeben. Um eine hohe Zahl von Atomen in eine magneto-optische Falle zu laden muß eine Laserleistung zur Verfügung stehen, die die Leistung von im gewöhnlichen benutzten, kommerziell erhältlichen Laserdioden übersteigt. Um eine größere Leistung zu erreichen, wurde für dieses Experiment ein injektions-stabilisierter Breitstreifen-Diodenlaser aufgebaut und charakterisiert [Shvarchuck et al., 2000]. Im Rahmen dieser Arbeit wurde dieser Laser in das Lasersystem integriert und zum ersten mal in einem Experiment zur Laserkühlung angewendet. Im Weiteren wird das Vakuumsystem beschrieben. Es besteht aus einer Rubidium-Dampfzelle, die eine Atomstrahlquelle beherbergt, und einer Ultra-Hochvakuumkammer, in der das Fangen und Kühlen der atomaren Wolke stattfindet. Darauf folgt ein detailliertes Porträt der magnetischen Falle. Der Aufbau der Falle wurde mit dem Ziel optimiert hohe Stabilität der Magnetfelder, große Flexibilität beim Einstellen der Fallenparameter und einen steilen Einschluß zu erreichen. Mit einem Magnetfeldgradienten von 353 G/cm und einer Krümmung von 286 G/cm^2 wurde die bisher steilste Magnetfalle dieses Typs realisiert. Letzteres ermöglicht schnelles Verdampfungskühlen, was in einer hohen Teilchenzahl am BEC Übergang resultiert. Im Weiteren werden die zum Verdampfungskühlen benutzten Komponenten der rf Signalquelle spezifiziert. Das Kapitel endet mit einer Beschreibung des Abbildungssystemes, mit dem die kalte Wolke detektiert und ihre Eigenschaften gemessen werden.

Kapitel 4 basiert auf der Veröffentlichung [Dieckmann et al., 1998] über die intensive Atomstrahlquelle, die im Rahmen dieser Arbeit entwickelt wurde. Der hohe atomare Fluß dieser Quelle, beinahe 10^{10} Atome/s mit einer mittleren Geschwindigkeit von 10 m/s, ist die Grundlage für das Erzielen von hohen Teilchenzahlen innerhalb kurzer Experimentierzeiten. Das Arbeitsprinzip der Atomstrahlquelle beruht auf dem der zweidimensionalen megneto-optischen Dampfzellenfalle (2D-MOT). Es wird untersucht, wie der Fluß durch Variationen der 2D-MOT Konfiguration optimiert werden kann. Dafür werden Vergleichsmessungen mit verschiedenen Geometrieen durchgeführt. Der höchste gemessene

Fluß übersteigt den Fluß bisheriger Atomstrahlquellen, die auf Extraktion von Atomen aus einer Dampfzelle mit Hilfe von Lichtkräften beruhen, um zwei Größenordnungen, wobei dieselbe geringe Laserleistung (50 mW) zur Anwendung kommt.

In Kapitel 5 wird die Atomstrahlquelle angewendet um eine magneto-optische Falle mit einer hohen Teilchenzahl von 10^{10} Atomen zu laden. Der gemessene atomare Fluß wird mit der Laderate verglichen, woraus sich eine Transfereffizienz von 70 % ergibt. Im Folgenden wird zum ersten mal demonstriert, wie die Transfereffizienz verbessert werden kann, dadurch daß eine repulsive Lichtktraft aufgrund des von der gespeicherten Wolke herrührenden Fluoreszenzlichts vermieden wird. Dies wird durch optisches Pumpen der Atome im Atomstrahl in einen dunklen Hyperfeinzustand realisiert. Nach dem Laden wird die gespeicherte Wolke durch Polarisationsgradientenkühlen auf eine Temperatur von 40 μK abgekühlt. Diese Temperatur liegt weit unter dem Dopplerlimit, welches für Rubidium 144 μK beträgt. Das Kapitel endet mit einer Beschreibung der Art und Weise, in der die Temperatur nach dem sub-Doppler Kühlen für den Fall hoher Teilchenzahlen minimiert wird.

Kapitel 6 erklärt den Umladevorgang von der magneto-optischen Falle in die Magnetfalle. Darauf folgt eine Charakterisierung der für eine adiabatische Kompression der gespeicherten Wolke in der Magnetfalle notwendigen Einzelschritte. Nach der adiabatischen Kompression ist die Wolke mit 4×10^9 Atomen bevölkert, bei einer Temperatur von 760 μK und einer Dichte von 7×10^{11} Atomen/cm^3. Die Charakterisierung des magnetischen Speicherns wird durch Messungen der Lebensdauer der Atome in der Magnetfalle und der harmonischen Fallenfrequenzen vervollständigt. Die Messung der Lebensdauer in der komprimierten Magnetfalle gibt Aufschluß darüber, ob effizientes Verdampfungskühlen möglich ist, und ob Bose-Einstein Kondensation erreicht werden kann. Die Messung der harmonischen Fallenfrequenzen ist unerläßlich für die quantitative Analyse des gespeicherten Bose-Gases.

Im ersten Teil des Kapitels 7 wird Verdampfungskühlen im sogenannten 'runaway regime' beschrieben. Die Effizienz des Verdampfungskühlens wird hinsichtlich Teilchenverlusts analysiert. Standardmäßig wird der Kühlprozeß nach einer Dauer von 10 s beendet, kann aber auch schon nach 2 s zu Bose-Einstein Kondensation mit 60 % geringerer Teichenzahl führen. Im zweiten Teil wird die Beobachtung der Bose-Einstein Kondensation präsentiert. Dies beinhaltet eine Beschreibung der Analyse der Absorptionsbilder. Der Phasenübergang wird mit 1.5×10^7 Atomen bei einer Temperatur von 1.5 μK und einer Dichte von 7×10^{14} Atomen/cm^3 erreicht. Mit diesen höchsten Teichenzahlen werden Gasproben produziert, mit deren Eigenschaften das Übergangsgebiet zwischen dem stoßfreien und dem hydrodynamischen Limit untersucht werden kann. Schließlich wird das Kapitel mit einer Demonstration des sogenannten "Atomlasers" beendet, mit dem die Phasenkohärenz der Atome im Bose-Einstein Kondensat gezeigt wird.

Kapitel 8 handelt von der sogenannten "Oort'schen Wolke". Sie besteht aus Rubidiumatomen, die die magnetische Falle bis zu Energien von einigen mK bevölkert. Dies wird durch die große Tiefe der Magnetfalle (12 mK) ermöglicht. Es wird demonstriert, wie die Oort'sche Wolke zum ersten mal deutlich nachgewiesen wurde. Dazu wird eine Methode gezeigt, mit der die Teilchenzahl in der Oort'schen Wolke gemessen werden kann, und sich Information über die Energieverteilung in der Oort'schen Wolke erhalten läßt. Das Prinzip dieser Methode beruht auf dem Freilassen der Atome aus der magnetischen Falle

und dem Wiedereinfang in eine magneto-optische Falle. In diesem Experiment wurde eine Bevölkerung der Oort'schen Wolke oberhalb von 250 μK von bis zu 2.4×10^6 Atomen bei einer gemittelten Energie von 3 mK gefunden. Es wird untersucht, wie Atome der Oort'schen Wolke zu Heizen und Verlusten in der kalten Wolke führen können. Um solche Phänomene im Zusammenhang mit der Oort'schen Wolke zu studieren wurden kalte Wolken bei Temperaturen etwas oberhalb des BEC Phasenüberganges verwendet. Solche kalten Wolken erlauben es, die von der Oort'schen Wolke augehenden Phänomene ohne die zusätzliche Komplexität der Bose-Eintein Kondensate zu identifizieren. Darüber hinaus wird untersucht, wie die von der Oor'schen Wolke ausgehenden Effekte mit Hilfe eines rf Schildes unterdrückt werden können. Als Entstehungsursache für den größten Teil der Oort'schen Wolke ist in diesem Experiment unvollständiges Verdampfungskühlen verantwortlich. Mit dieser Kenntnis ist es möglich die Teilchenzahl in der Oort'schen Wolke durch Anwendung eines veränderten Kompressions- und Kühlschemas um einen Faktor 6 zu reduzieren. Dies erlaubt es die Auswirkungen der Oort'schen Wolke auf die kalte Wolke für hohe und geringe Teilchenzahlen in der Oort'schen Wolke zu vergleichen. Eine bemerkenswerte Beobachtung ist die Zunahme der Teilchenzahl in der kalten Wolke bei gleichzeitiger Abnahme in der Oort'schen Wolke, die nur bei den höchsten Dichten in der kalten Wolke auftritt. Dies wird als Einfang von Atomen aus der Oort'schen Wolke in die kalte Wolke durch eine Stoßkaskade interpretiert. Schließlich werden die Konsequenzen dieser Beobachtungen hinsichtlich der Möglichkeiten, das hydrodynamische Limit mit einem Bose-Einstein Kondensat zu erreichen, diskutiert.

Acknowledgments

During the realization of this project I was collaborating and getting help and company from many colleagues and friends. To these people I would like to say thank you:

First, I would like to thank my promoter Jook Walraven for starting up the BEC project with rubidium and providing me with all the support it took to realize it. The scientific education he gave me in many inspiring discussions about physics is invaluable for me and was the basis for having a great time in his group.

With Martin Zielonkowski the first main goal, BEC, was achieved. I have found in him an enjoyable teammate who gave his contributions with patience, creativity and a wide understanding of physics especially during the Ort cloud measurements. I would not like to miss His moral support during the last year was very important.

The other mate was Igor Shvarchuck who solved, with the realization of the broad-area diode laser and the detection system, two difficult experimental tasks which were of the greatest importance for the successful realization of the experiment. With him I also shared the moment of achieving BEC. In our meager spare time I found out that he is a perfect teacher of ice-skating. I wish him all the best for the rest of his PhD period.

I would like to thank Matthias Weidemüller for the well organized supervision in the first year. With him the foundation for a working experiment was laid. After working some time alone it was of great importance that Robert Spreeuw from the University of Amsterdam got involved in the project providing a lot of physics input and being under all circumstances an enjoyable and important discussion partner.

The work of Pieter Valkering, the only Dutch person in the group aside from Jook, on the realization and simulation of evaporative cooling was of great help for the experiment.

As the experiment was started from the scratch only the strong support of many technicians made the fast realization of the experiment possible. The experiment was initialized at the University of Amsterdam with the help of Otto Höpfner, Bert Zwart, and Jost Overtoom, with the transfer of the setup to AMOLF as a perspective. At AMOLF, we experienced the all round support of Hans Alberda, Idsart Attema, Herman Ficke, Henk Neerings, Duncan Verheiden, Ton Vijftigschild, Martijn Witlox. Each of them delivering precise and detailed, important items built with their experience and creativity. Especially, I would like to thank our group technician Hinco Schoenmaker, who almost always came up with solutions and immediate help. The result: The machine

works fine, and the first BEC below sea level has been achieved.

For an experimentalist it is a luxury to share an office (non smoking) with the theory group of Gora Shlyapnikov. With his enthusiasm he taught me a lot of physics and any question could be discussed at almost any time. The same holds for Peter Fedichev and Dimitry Petrov. Peter also helped me a lot in battling with Mathematica's syntax and I enjoyed the time spent together in Amsterdam outside the Laboratory. It is of great value for the experimental group how Dimitry is engaged with some experiment-related problems and I wish him to keep on having a fruitful collaboration.

Thanks to all colleagues of the other Amsterdam cold atom groups and all visiting scientists for creating a stimulating scientific environment. Especially with Dirk Voigt a useful exchange of knowledge and material has taken place.

I would like to thank Pepijn Pinkse, Allard Mosk, Tom Hijmans for supporting my start at the University of Amsterdam. I shared with Pepijn many diners at the mensa and coffees at the Kriterion. I wish him even more success in Munich. The same holds for Allard who, during his stay in Heidelberg, let me his flat in Amsterdam. This increased my life and light standard enormously and let me feel much more at home in Amsterdam. Tom Hijmans was very important for the start of the the project with his ideas about the atomic beam source. During my whole PhD period I was impressed and got inspired by his understanding of physics, although he never understood why only one Eifel Tower was build.

Thanks to Catherine Garrec everybody knows how rubidium spectroscopy lines look like in Amsterdam. With the hospitality of our Greek colleagues and friends Giannnis Zacharakis and Adonius we spent a wonderful vacation in Crete.

I thank Wolf van Klitzing and Lorenzo Vichi as new members of the group and my friends and colleges at AMOLF, Rüdiger Lang, Cristof Strohhöfer, Bernd Riedmüller, and all others for company and moral support and I wish a productive time in the future to everybody.

I would also like to thank all my friends accompanying me spending a nice time in Amsterdam.

Finally, I would like to thank my mother Heide and sister Annette for their interest, tolerance and moral support.